Distorted Weyl cones under perturbation
&
Monopole stabilization in interpenetrating pyrochlore lattices

Distorted Weyl cones under perturbation
&
Monopole stabilization in interpenetrating pyrochlore lattices

Vervormde Weylkegels onder verstoring
&
Stabilisering van monopolen in interpenetrerende
pyrochloorroosters

(met samenvatting in het Nederlands)

Proefschrift

ter verkrijging van de graad van doctor aan de Universiteit Utrecht op
gezag van de rector magnificus, prof. dr. H. R. B. M. Kummeling,
ingevolge het besluit van het college voor promoties in het openbaar
te verdedigen op maandag 28 oktober 2019 des morgens te 10.30 uur

door

Tycho Sven Sikkenk

geboren op 29 januari 1991
te Houten

Preface

This thesis is the result of four years of work performed at the Institute for Theoretical Physics at Utrecht University under supervision of dr. Lars Fritz, as well as on a long research visit to the Theory of Condensed Matter group at Cambridge University under supervision of dr. Claudio Castelnovo.

It correspondingly consists of two independent parts: Chapter 1 gives an introduction to, and outline of, the first part of this thesis on perturbed Weyl semimetals. The results of our research on these systems are described in Chapters 2 and 3. In Chapter 4 we introduce an extension of the spin ice model and present the results of our calculations and simulations therein. At the end of the thesis, the reader will find the bibliography, summaries in English and Dutch and a C.V. of the author.

I wish the reader much joy and inspiration from reading this thesis.

Tycho Sikkenk
August 2019, Utrecht

List of publications

This thesis is based on the following publications:

- <u>Tycho S. Sikkenk</u> and Lars Fritz, *"Disorder in tilted Weyl semimetals from a renormalization group perspective"*, Phys. Rev. B **96**, 155121 (2017).

- <u>Tycho S. Sikkenk</u> and Lars Fritz, *"Interplay of disorder and interactions in a system of subcritically tilted and anisotropic three-dimensional Weyl fermions"*, Phys. Rev. B **100**, 085121 (2019).

Other publications to which the author has contributed:

- <u>Tycho S. Sikkenk</u>, Kris Coester, Stefan Buhrandt, Lars Fritz, and Kai P. Schmidt, *"Emergence of a two-dimensional macrospin liquid in a highly frustrated three-dimensional quantum magnet"*, Phys. Rev. B **95**, 060401(R) (2017).

Contents

Contents

Part I

Distorted Weyl cones under perturbation

1 Introduction

This introductory chapter is based on unpublished work. Some sections loosely follow derivations presented elsewhere, among which most notably: Refs [1–3].

In the first decades of the 20th century, the field of physics found itself in a state of great flux. As opposed to earlier statements, fundamental science had turned out to be far from finished, and great advances were made in a wide range of areas in rapid succesion. Quantum mechanics was invented to describe the wavelike properties of matter at very small length scales. At the other end of the scale, the nascent theory of relativity explained gravitation as curvature of spacetime itself that is caused by very large massive bodies. It long remained unclear how to reconcile these distinct theories at scales where their domains of validity may be expected to overlap. A first breakthrough was achieved by by P. A. M. Dirac in 1928 [4], proposing a linear differential equation for the propagation of massive spin-1/2 fermions that combines the relativistic equal footing of space and time with a positive definite quantum mechanical wavefunction probability [5]. This Dirac equation reads

$$- \left(i \, \gamma^\mu \partial_\mu - m \right) \Psi = 0, \tag{1.1}$$

where $\partial_\mu = (\partial_t, \boldsymbol{\nabla})$ and m is the mass of the fermion, which is symbolized by four-spinor Ψ. We use natural units $\hbar = c = 1$ throughout, unless otherwise indicated. The gamma matrices are defined through their Clifford commutation algebra

$$\{\gamma^\mu, \gamma^\nu\} = -2\eta^{\mu\nu} = -2 \, \mathrm{diag} \left(-1, +1, +1, +1\right), \tag{1.2}$$

in terms of a mostly positive Minkowski metric. Remarkably, only one year later in 1929, H. Weyl realized that the gamma matrices have a convenient off-diagonal representation

$$\gamma^0 = \begin{pmatrix} 0 & \sigma_0 \\ \sigma_0 & 0 \end{pmatrix}, \qquad \boldsymbol{\gamma} = \begin{pmatrix} 0 & \boldsymbol{\sigma} \\ -\boldsymbol{\sigma} & 0 \end{pmatrix}, \tag{1.3}$$

by which the massless limit of Eq. (1.1) diagonalizes and so decomposes into two independent sectors [6],

$$-i\,\gamma^{\mu}\partial_{\mu}\Psi = -i\,\gamma^{0}\begin{pmatrix}\sigma_0\partial_0 - \boldsymbol{\sigma}\cdot\boldsymbol{\nabla} & 0 \\ 0 & \sigma_0\partial_0 + \boldsymbol{\sigma}\cdot\boldsymbol{\nabla}\end{pmatrix}\begin{pmatrix}\psi^{(-)} \\ \psi^{(+)}\end{pmatrix} = 0, \qquad (1.4)$$

where σ_{μ} are the usual Pauli matrices and $\psi^{(\chi)}$ are two-spinors that are characterized by opposite chiralities $\chi = \pm$. Although Weyl particles are theoretically permissible in the standard model, no fundamental particles have so far been observed experimentally to obey the Weyl equations in Eq. (1.4). In condensed matter however, they can be used to describe the effective behavior of the chiral low energy excitations close to the touching points in the band structure of so-called Weyl semimetals, where the dispersion is approximately linear.

In section 1.1 of this introductory chapter we take a closer look at these effective Weyl modes in condensed matter, providing a model setting and examining some of the characteristics that have recently put them under intense scrutiny. In section 1.2 we lay out the physics behind the perturbations to which we aim to submit the Weyl fermion model. In section 1.3 we set up the theory of the renormalization group by which the general behavior of the Weyl model may be determined. In section 1.4 we relate our model setting to the theory of quantum electrodynamics, with all the Ward identities that entails.

In chapter 2 we subsequently submit the Weyl fermion model with a tilted dispersion to perturbation by placing it within a disordered background. We then derive the corresponding renormalization group flow using a momentum shell cutoff scheme. In chapter 3 we expand on this setup by including the possibility of anisotropies in the tilted dispersion and by also allowing for Coulomb interactions between the Weyl excitations on top of the disorder. Regularizing by means of a double epsilon expansion leads to a set of flow equations that is fully consistent with the symmetries of quantum electrodynamics.

1.1 Free Weyl fermions in condensed matter

We start our discussion from the momentum space representation of the action of a free massless Dirac fermion,

$$S_\Psi[\Psi] = \int_{\omega,\mathbf{q}} \Psi^\dagger_{\omega,\mathbf{q}} G^{-1}_{0;\Psi}(i\omega,\mathbf{q})\Psi_{\omega,\mathbf{q}}$$
$$= \sum_{\chi=\pm} \int_{\omega,\mathbf{q}} \psi^{(\chi),\dagger}_{\omega,\mathbf{q}} G^{-1}_{0,\chi}(i\omega,\mathbf{q})\psi^{(\chi)}_{\omega,\mathbf{q}} = \sum_{\chi=\pm} S_\psi[\psi^{(\chi)}]. \qquad (1.5)$$

Variation of this action with respect to conjugate field $\Psi^\dagger$ will yield a version of the Fourier transformed form of the massless Dirac equation Eq. (1.4). The corresponding inverse Green function is given by

$$G^{-1}_{0;\Psi}(i\omega,\mathbf{q}) = \begin{pmatrix} G^{-1}_{0,-}(i\omega,\mathbf{q}) & 0 \\ 0 & G^{-1}_{0,+}(i\omega,\mathbf{q}), \end{pmatrix} \qquad (1.6)$$

where the Weyl decompostion is explicitly observed. The constituent inverse Green functions to the Weyl equations are given by

$$G^{-1}_{0,\chi}(i\omega,\mathbf{q}) = i\omega\sigma_0 - \mathcal{H}_{0,\chi} = (i\omega - vtq_\parallel)\sigma_0 - v\chi(q_\parallel\mathbf{d} + \eta\mathbf{q}_\perp)\cdot\boldsymbol{\sigma}, \qquad (1.7)$$

where $\chi = \pm$ encodes the chirality of the Weyl fermion. The energy eigenspectrum of these excitations fermion may be obtained by diagonalizing the Hamiltonian $\mathcal{H}_{0,\chi}$. As it is expressed completely in terms of Pauli matrices, such is done straightforwardly by squaring the operator while taking account of the constant shift. Alternatively, the energy levels also correspond directly to the structure of the poles of the Green function Eq. (1.7). They are given by

$$E_{0,s}(\mathbf{q}) = v\left(t\,q_\parallel + s\sqrt{q_\parallel^2 + \eta^2 q_\perp^2}\right). \qquad (1.8)$$

where $s = \pm 1$ distinguishes the conduction and valence bands. This conical dispersion is depicted in Fig. 1.1 for some indicative parameter values. It is important to realize that these Weyl fermions are effective quasiparticles describing the low-energy excitations close to touching points in the band structure of selected materials called semimetals. As such they are not constrained by the requirement to preserve Lorentz symmetry, as a putative

fundamental Weyl particle would. Although they are massless, they propagate at the Fermi velocity $v \ll c$, several orders below the speed of light. Furthermore, there can be distortions in the dispersion. The Fermi velocity need not be isotropic in all directions, as parametrized by the variable η in Eq. (1.8). The parameter t controls a permissible tilting of the Weyl cone, changing the circular shape of the Fermi surface away from the nodal point in upright position. In type-II Weyl semimetals with tilts $t \geq 1$ electron and hole pockets coexist in the Fermi surface, giving rise to some interesting and peculiar phenomena [7]. Nevertheless we here restrict to type-I Weyl fermions characterized by tilts $0 \leq t < 1$, whose Fermi surfaces are ellipsoidal cuts of the dispersion cone.

(a) $t = 0$, $\eta = 0$.   (b) $t = 0.5$, $\eta = 0$.   (c) $t = 0$, $\eta = 1.5$.   (d) $t = 0.5$, $\eta = 1.5$.
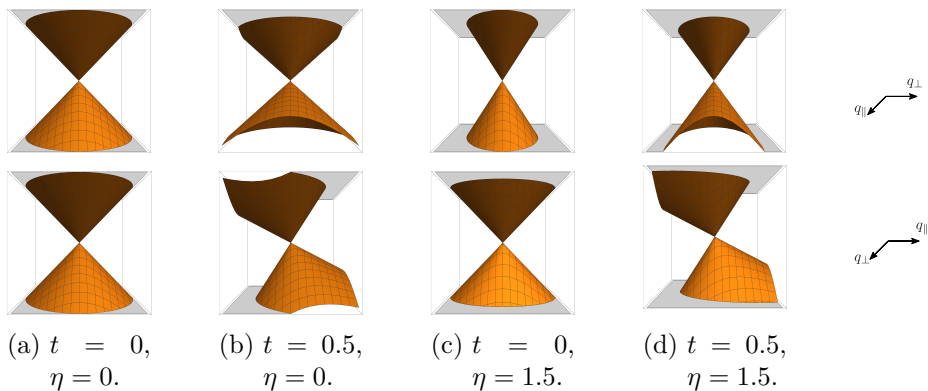
Figure 1.1: Conical dispersion in Eq. (1.8) of a single Weyl mode for indicated parameter values.

Although it is not detectable in the conical dispersion Eq. (1.8) of a condensed matter Weyl fermion, their chiral nature is reflected in their peculiar magnetic response. A vector potential $\mathbf{A}$ and the magnetic field $\mathbf{B}$ that is its curl, which without loss of generality can be chosen as

$$\mathbf{A} = -\frac{yB}{2}\hat{x} + \frac{xB}{2}\hat{y}, \qquad \mathbf{B} = \boldsymbol{\nabla} \times \mathbf{A} = B\hat{z}, \qquad (1.9)$$

may be included in the Weyl cone model by minimal substitution of the

momenta $\mathbf{q}$ in the free Hamiltonian $\mathcal{H}_{0,\chi}$ by the gauge covariant momenta

$$\mathbf{\Pi} = \mathbf{q} + g\mathbf{A}, \qquad [\Pi_y, \Pi_x] = \frac{gB}{2}\left([x, q_x] + [y, q_y]\right) = igB \qquad (1.10)$$

where g is the charge of the coupling between the Weyl fermion and the magnetic field. Its components have commutation relations proportional to the canonical comutator $[x, q] = i$ that is the cornerstone of quantum mechanics. Continuing the analogy, this setup permits ladder operators of the same form as the prototypical quantum harmonic oscillator [8],

$$a = \frac{\Pi_x + i\Pi_y}{\sqrt{2gB}}, \qquad a^\dagger = \frac{\Pi_x - i\Pi_y}{\sqrt{2gB}}, \qquad [a, a^\dagger] = 1. \qquad (1.11)$$

Restricting for simplicity to the isotropic untilted case this results in the magnetic Hamiltonian

$$\mathring{\mathcal{H}}_\chi^{\mathrm{LL}} = v\chi\,\boldsymbol{\sigma}\cdot\mathbf{\Pi} = v\chi\,\boldsymbol{\sigma}\cdot(\mathbf{q} + g\mathbf{A}) = v\chi\begin{pmatrix} q_z & \Pi_x - i\Pi_y \\ \Pi_x + i\Pi_y & -q_z \end{pmatrix}$$

$$= v\chi\begin{pmatrix} q_z & \sqrt{2gB}\,a^\dagger \\ \sqrt{2gB}\,a & -q_z \end{pmatrix}. \qquad (1.12)$$

The eigenvalue equation for this magnetic Hamiltonian can be solved by the Ansatz eigenstates $\psi_n^{(\chi)} = (|n\rangle, \alpha_n|n-1\rangle)^T$ where the $|n\rangle$ for $n = 0, 1, 2, \ldots$ are ladder operator eigenfunctions and the α_n are unknowns to be determined consistently. The corresponding energy spectrum consists of Landau levels (LL) given by

$$\mathring{E}_{n=0}^{\mathrm{LL}}(q_z, B) = v\chi\,q_z, \qquad \mathring{E}_{n\geq 1,s}^{\mathrm{LL}}(q_z, B) = s\,v\sqrt{q_z^2 + 2gBn} \qquad (1.13)$$

where $s = \pm 1$ distinguishes the conduction and valence bands for Landau levels indexed by $n \geq 1$. The magnetic dispersion is depicted in Fig. 1.2 for both $\chi = \pm$. As a consequence of the chirality of the Weyl fermion the lowest Landau level $n = 0$ is directional. An electric field $\mathbf{E}$ in the same direction as $\mathbf{B} \parallel \hat{z}$ would then have the effect of respectively removing or adding charge carriers from a negative respectively positive chirality fermion. The density of modes within an individual cone is not preserved, seemingly leading to the conclusion that the Weyl model violates the fundamental law of conservation of electric charge. Because of this paradoxical behavior, this phenomenon has become known as the chiral anomaly [9].
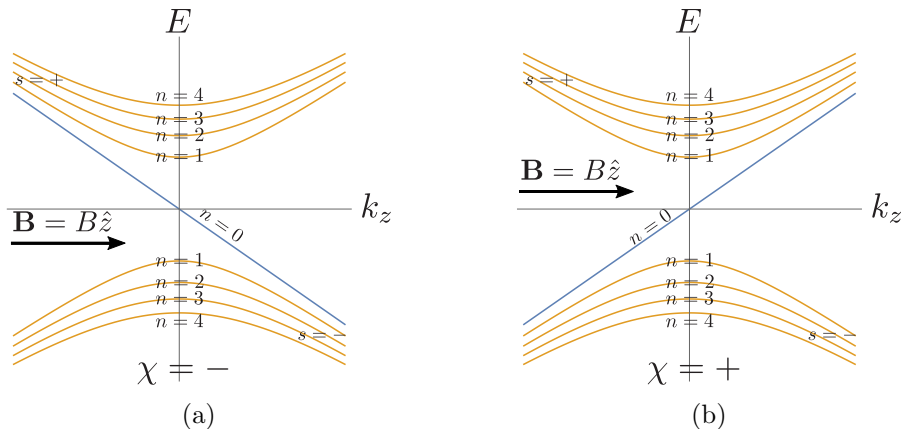
Figure 1.2: Landau level spectrum for a chiral Weyl fermion $\chi = \pm$ under influence of a magnetic field.

The anomalous response of a Weyl fermion to magnetic fields is intrinsically linked to its chirality, which ultimately stems from the singular topology of the wavefunction at the nodal Weyl point. An eigenstate moving adiabatically through the parameter space $\{\mathbf{R}\}$ can pick up a non-vanishing Berry phase if the followed path is a closed contour $\mathcal{C}$. This phase for the eigenfunction $|u_n(\mathbf{R})\rangle$ is defined as

$$\gamma_n = \oint_{\mathcal{C}} \mathrm{d}\mathbf{R} \cdot \boldsymbol{\mathcal{A}}_n(\mathbf{R}) = \int_S \mathrm{d}\mathbf{S} \cdot \boldsymbol{\Omega}_n(\mathbf{R}) = \int_S \sum_{i,j,l=1}^3 \mathrm{d}S_l \, \epsilon_{lij} \Omega_{n;ij}(\mathbf{R}), \quad (1.14)$$

where we have used Stokes theorem to rewrite the contour integral of the Berry connection $\boldsymbol{\mathcal{A}}_n$ as integral of its curl, the Berry curvature $\boldsymbol{\Omega}_n$, over the enclosed surface S. These quantities are given by

$$\boldsymbol{\mathcal{A}}_n(\mathbf{R}) = i\langle u_n(\mathbf{R})|\boldsymbol{\nabla}_{\mathbf{R}}|u_n(\mathbf{R})\rangle, \qquad \boldsymbol{\Omega}_n(\mathbf{R}) = \boldsymbol{\nabla}_{\mathbf{R}} \times \boldsymbol{\mathcal{A}}_n(\mathbf{R}). \quad (1.15)$$

The curvature is like the parameter space field arising from the vector potential that is the connection, and the Berry phase is the flux of this field through the surface. The more general Berry curvature two-form is the pure antisymmetrization of the pseudovector [10], which allows for a significant

rewriting in terms of derivatives of the model's Hamiltonian,

$$\Omega_{n;ij}(\mathbf{R}) = \frac{1}{2} \sum_{l=1}^{3} \epsilon_{ijl} \Omega_{n;l}(\mathbf{R}) = \partial_{R_i} \mathcal{A}_{n,j}(\mathbf{R}) - (i \leftrightarrow j)$$

$$= i \sum_{n' \neq n} \frac{\left\langle u_n(\mathbf{R}) \middle| \partial_{R_i} H \middle| u_{n'}(\mathbf{R}) \right\rangle \left\langle u_{n'}(\mathbf{R}) \middle| \partial_{R_j} H \middle| u_n(\mathbf{R}) \right\rangle - \text{c.c.}}{(E_n - E_{n'})^2},$$

(1.16)

where we have used that we can rewrite $\left\langle u_n(\mathbf{R}) \middle| \partial_{R_i} H \middle| u_{n'}(\mathbf{R}) \right\rangle = (E_n - E_{n'}) \left\langle \partial_{R_i} u_n(\mathbf{R}) \middle| u_{n'}(\mathbf{R}) \right\rangle$. This shows that the curvature diverges at degeneracy points in $\mathbf{R}$-parameter space where the energy bands come to overlap. Consequently lines of the curvature field originate from or terminate at such points [11].

For a class of chiral Hamiltonians $H_\chi = h_0 \sigma_0 + \chi \mathbf{h} \cdot \boldsymbol{\sigma}$ with $\chi = \pm$, which also includes the tilted anisotropic Weyl Hamiltonian $\mathcal{H}_{0,\chi}$ defined by Eq. (1.7), the Berry curvature is easily computed explicitly. They have only two energy eigenstates $|u_{\chi,s}\rangle = |u_{-\chi,-s}\rangle$ and $|u_{\chi,-s}\rangle = |u_{-\chi,s}\rangle$ labelled by $s = \pm$, with energy levels split by $|E_s - E_{-s}| = 2|\mathbf{h}| = 2h$. It is then straightforward to find matrix elements $\langle u_{\chi,s}|\partial_{h_i} H_\chi |u_{\chi,-s}\rangle = \chi \langle u_{\chi,s}|\sigma_i|u_{\chi,-s}\rangle$, so that Eq. (1.16) for the Berry curvature tensor simplifies to

$$\Omega_{\chi,s;ij}(\mathbf{h}) = \frac{i}{4h^2} \Big(\langle u_{\chi,s}|\sigma_i|u_{\chi,-s}\rangle \langle u_{\chi,-s}|\sigma_j|u_{\chi,s}\rangle - \text{c.c.} \Big)$$

$$= -\frac{s}{2h^2} \Big| \text{Im} \Big(\langle u_{+,+}|\sigma_i|u_{+,-}\rangle \langle u_{+,-}|\sigma_j|u_{+,+}\rangle \Big) \Big|.$$

(1.17)

Inserting the explicit form of the eigenstates then yields the Berry curvature pseudovector components

$$\Omega_{\chi,s;l}(\mathbf{h}) = \sum_{i,j=1}^{3} \epsilon_{lij} \Omega_{\chi,s;ij}(\mathbf{h}) = -\frac{s\chi}{2h^3} h_l.$$

(1.18)

At the Fermi level only the lower band $s = -$ contributes and the curvature takes the shape of a field emanating from a monopole with charge $\chi = \pm$ situated at the origin $\mathbf{h} = \mathbf{0}$. Depending on the chirality, this touching point in the dispersion is either a source or sink of Berry flux [11].

Since the Brillouin zone (BZ) in which the band structure of a crystal is defined is a closed parameter space, the total charge of the curvature field contained in it trivially vanishes. There is no boundary to escape to, so all the field lines must be contained within the space itself [5]. As a consquence, in a consistent model every monopole of the curvature field must be accompanied by a partner antimonopole with the converse chiral charge. The only way to remove a Weyl nodal point from the spectrum is to let it merge with its chiral partner into a Dirac point without chiral charge, after which a gap can open. Since Weyl cones in material band structures are well-separated in momentum space [12–15], such merging requires major perturbations reconfiguring the model. The relative isolation of a Weyl node in the BZ guarantees that the topological protection of a chiral Weyl node cannot be broken in a realistic scenario. For stability purposes, it is then sufficient to consider only a single Weyl node. For probing transport properties however both nodes need to be incorporated. The apparent contradiction in the chiral anomaly is an artefact of an incomplete model. When both Weyl fermions in a chiral pair are included, imposing parallel magnetic and electric fields simply pumps electric charge between the nodes [5].

While the Berry phase is dependent on the contour, or the surface enclosed therein, for which it is computed, it is famously associated to various phenomena that are independent of the followed path. The Chern number of a surface S is proportional to the Berry phase produced by the penetrating flux,

$$\nu_n = \frac{1}{2\pi}\gamma_n = \frac{1}{2\pi}\int_S \mathrm{d}\mathbf{S}\cdot\mathbf{\Omega}_n(\mathbf{q}). \tag{1.19}$$

By construction, the Chern number calculates the imbalance of chiral charges in the Fermi sea on either side of the momentum surface and is thus a quantized integer. In the double Weyl fermion model this results in the picture of Fig. 1.3 that slices the BZ by surfaces perpendicular to the momentum vector separating the chiral partner monopoles. Such slices have a non-zero Chern number $\nu_- = 1$ only when they segregate the charges of a pair [16]. As a result of the bulk-boundary correspondence this implies that in this region there must be topologically non-trivial border states dubbed Fermi arcs connecting the projections of the nodes on the periodicity edges of the BZ [12–15] that can lead to interesting non-local transport properties [17, 18].
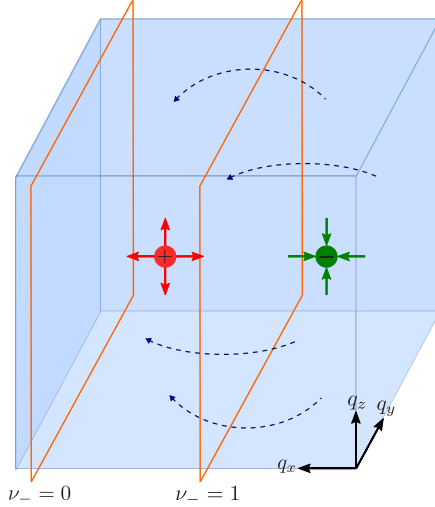
Figure 1.3: Three-dimensional Brillouin zone at the Fermi level containing two Weyl nodes of opposite chirality $\chi = +$ (red) and $\chi = -$ (green). Bulk surfaces separating the chiral partners have a non-zero Chern number $\nu_- = 1$, and correspondingly there will be non-trivial Fermi arcs (blue dashed lines) connecting the projections of the nodes on the BZ periodicity edges [16].

So far, our treatment of effective Weyl fermions in the setting of condensed matter band structures has been mostly theoretical. It is then instructive to see how the above equations relate to the world of experiment by considering how they impact the density of states (DoS), a quantity that can be probed by for example Scanning Tunneling Microscopy (STM) measurements [19]. The DoS, a measure of the number of states available at some energy ω, is obtained from the Green function of Eq. (1.7) as

$$\rho_{0,\chi}(\omega) = -\frac{1}{\pi} \int_{\mathbf{q}} \operatorname{Im} \operatorname{Tr} G_{0,\chi}(\omega^+, \mathbf{q})$$

$$= -\frac{2}{\pi} \operatorname{Im} \int_{\mathbf{q}} \frac{\omega^+ - vtq_{\parallel}}{(\omega^+ - vtq_{\parallel})^2 - v^2(q_{\parallel}^2 + \eta^2 q_{\perp}^2)},$$

where $\omega^+ = \omega + i0^+$ in the sense that the limit to zero from above should be taken on the imaginary part. Completing the square in the denominator,

shifting the parallel integration variable and keeping only even terms yields

$$\rho_{0,\chi}(\omega) = -\frac{2}{\pi}\,\omega \int_{\tilde{\mathbf{q}}} \mathrm{Im}\left[(\omega^+)^2 - v^2(1-t^2)(\eta^2\tilde{q}_\perp^2 + (1-t^2)\tilde{q}_\parallel^2)\right]^{-1}$$

$$= \frac{\omega}{\eta^2 v^3(1-t^2)^2}\int_{\mathbf{q}'}\frac{1}{\pi q'}\left\{\mathrm{Im}\left[(\omega^+ + \mathbf{q}')^{-1} - (\omega^+ - \mathbf{q}')^{-1}\right]\right\},$$

where we have rescaled the parallel and perpendicular integration variables to restore the isotropy of the integrand. Using now the usual theorem $\mathrm{Im}(x \pm i0^+)^{-1} = \mp\pi\delta(x)$, we find

$$\rho_{0,\chi}(\omega) = -\frac{\omega}{\eta^2 v^3(1-t^2)^2}\int_{\mathbf{q}'}\frac{1}{q'}\left\{\delta(\omega + \mathbf{q}') - \delta(\omega - \mathbf{q}')\right\}$$

$$= \frac{\omega}{\eta^2 v^3(1-t^2)^2}\int_{-\omega}^{+\omega}\frac{\mathrm{d}q_\parallel'}{2\pi}\int_0^\infty\frac{\mathrm{d}q_\perp'}{2\pi}\delta(q_\perp' - q_{\perp,(0)}')\left(\theta(\omega) - \theta(-\omega)\right)$$

$$= \frac{\omega^2}{2\pi^2\eta^2 v^3(1-t^2)^2}, \tag{1.20}$$

where we have rewritten the delta function as $\delta(\omega \mp \mathbf{q}) = \delta(q_\perp - q_{\perp,(0)})$ $\theta(\omega)\,q/q_\perp$ for the single real pole $q_{\perp,(0)}$. Note that in the limit $t \to 1$ the tilted DoS becomes singular, indicating the onset of a type-I to type-II transition. The form of the Density of States set out in Eq. (1.20) is essential because it stipulates experimentally observable features that define a material as a type-I Weyl semimetal. As a consequence of the presence of the characteristic Weyl nodal point the DoS will vanish at the Fermi level $\omega = 0$. Similarly, the quadratic scaling with the energy away from the band touching point is a direct consequence of the linearity of the dispersion Eq. (1.8). As we will see in section 1.2, these properties make the DoS an appropriate choice of order parameter to gauge if a phase transition out of the semimetallic regime has occured.

1.2 Perturbations to the free Weyl fermion model

1.2.1 Coulomb interactions

Coulomb's law states that the electric field emanating from a stationary point particle with charge Q located at the origin is given by

$$\mathbf{E}(\mathbf{x}) = \frac{Q}{4\pi \, x^3} \, \mathbf{x}. \tag{1.21}$$

The total field produced by a collection of point charges Q_i at positions $\mathbf{x}_i$ spread through space is a superpostion that can be rewritten as an integral over the appropriate charge density,

$$\mathbf{E}(\mathbf{x}) = \frac{1}{4\pi} \sum_i Q_i \frac{(\mathbf{x} - \mathbf{x}_i)}{|\mathbf{x} - \mathbf{x}_i|^3} = \frac{1}{4\pi} \int_{\mathbf{x}'} \varrho(\mathbf{x}') \frac{(\mathbf{x} - \mathbf{x}')}{|\mathbf{x} - \mathbf{x}'|^3}. \tag{1.22}$$

Taking the divergence of this vector equation yields the differential form of Gauss' law,

$$\boldsymbol{\nabla} \cdot \mathbf{E}(\mathbf{x}) = \frac{1}{4\pi} \int_{\mathbf{x}'} \varrho(\mathbf{x}') \, \boldsymbol{\nabla} \cdot \frac{(\mathbf{x} - \mathbf{x}')}{|\mathbf{x} - \mathbf{x}'|^3} = \int_{\mathbf{x}'} \varrho(\mathbf{x}') \, \delta(|\mathbf{x} - \mathbf{x}'|) = \varrho(\mathbf{x}). \tag{1.23}$$

Absent a time-dependent magnetic field producing a flux that integrates to a electric field contribution, the curl of the electric field will vanish by Faraday's law of induction [20]. As a result the conservative field can be written as the gradient of some scalar field $\Phi(x)$,

$$\boldsymbol{\nabla} \times \mathbf{E} = \partial_t \mathbf{B} = 0, \qquad \mathbf{E}(\mathbf{x}) = -Q_{\text{tot}} \, \boldsymbol{\nabla}\Phi(x), \tag{1.24}$$

where we have separated the total charge $Q_{\text{tot}} = \int_{\mathbf{x}} \rho(\mathbf{x})$ from the potential for normalization purposes. Combining Gauss' law Eq. (1.23) and Faraday's law Eq. (1.24) gives the Poisson equation for electrostatics,

$$\varrho(\mathbf{x}) = \boldsymbol{\nabla} \cdot \mathbf{E}(\mathbf{x}) = -Q_{\text{tot}} \nabla^2 \Phi(x). \tag{1.25}$$

It can straightforwardly be solved by means of Fourier transformation to find the normalized potential produced by the charge density distribution,

$$\Phi(x) = \frac{1}{4\pi Q_{\text{tot}}} \int_{\mathbf{x}'} \frac{\varrho(\mathbf{x}')}{|\mathbf{x} - \mathbf{x}'|}. \tag{1.26}$$

In the case of a single point particle the charge density is peaked in a delta function distribution, causing the potential to assume the form

$$\varrho_{\text{Cou}}(\mathbf{x}) = Q\,\delta(\mathbf{x}), \qquad\qquad \Phi_{\text{Cou}}(x) = \frac{1}{4\pi\,x}. \qquad (1.27)$$

Note that the force that is experienced by a test particle with charge Q' when it is placed at position $\mathbf{x}$ inside the Coulomb potential is

$$\mathbf{F}_{\text{Cou}} = Q'\,\mathbf{E} = -Q\,Q'\,\boldsymbol{\nabla}\Phi_{\text{Cou}} = \frac{Q\,Q'}{4\pi x^2}\,\hat{x}, \qquad (1.28)$$

so that like charges repel whereas opposite charges attract. The momentum space representation of the Coulomb potential is given by

$$\Phi_{\text{Cou}}(q) = \frac{1}{4\pi}\int_{\mathbf{x}}\frac{e^{-i\mathbf{q}\cdot\mathbf{x}}}{x} = \frac{1}{2}\lim_{r\to\infty}\int_0^r \mathrm{d}x\int_{-1}^{+1}\mathrm{d}u\, x e^{-iqx\,u}$$
$$= \frac{1}{q^2}\lim_{r\to\infty}\int_0^r \mathrm{d}x\,\sin x = \frac{1}{q^2}\lim_{r\to\infty}(1-\cos r) \to \frac{1}{q^2}. \qquad (1.29)$$

The improper integral of this Fourier transform formally fails to converge because it oscillates infinitely wildly between 0 and $+2/q^2$ as $r\to\infty$. There are however more advanced definitions of the limit procedure that result in a convergent value. In the Cesàro method, an infinite sum is defined as the $n\to\infty$ limit of the sequence of means of the first n partial sums of the series [21]. Up to proportionality, the integral in derivation Eq. (1.29) is a continuous version of Grandi's series

$$\sum_{n=0}^{\infty}(-1)^n = \begin{cases} = (+1-1)+(+1-1)+\dots & = 0 \\ = +1+(-1+1)+(-1+1)+\dots & = +1 \end{cases} \to \frac{1}{2}, \qquad (1.30)$$

with arithmic Cesàro mean $1/2$. This regularizes the Fourier transform, showing that the Coulomb potential in three dimensions falls off quadratically with momentum space distance. Scattering between small momentum separated states will dominate.

The situation is different in the closely related Yukawa potential, in which a mass term is included in the momentum space denominator. Fourier trans-

formation yields

$$\Phi_{\text{Yukawa}}(x) = \int_{\mathbf{q}} \Phi_{\text{Yukawa}}(q)\, e^{i\mathbf{q}\cdot\mathbf{x}} = \int_{\mathbf{q}} \frac{1}{q^2 + m_\varphi^2} e^{i\mathbf{q}\cdot\mathbf{x}}$$

$$= \frac{1}{4\pi^2} \int_0^\infty \mathrm{d}q\, \frac{q^2}{q^2 + m_\varphi^2} \int_{-1}^{+1} \mathrm{d}u\, e^{iqx\,u}$$

$$= \frac{1}{2\pi^2} \int_0^\infty \mathrm{d}q\, \frac{q^2}{q^2 + m_\varphi^2} \frac{\sin(qx)}{q\,x} = \frac{1}{4\pi^2 ix} \int_{-\infty}^\infty \mathrm{d}q\, \frac{q\, e^{iqx}}{q^2 + m_\varphi^2}$$

$$= \frac{1}{4\pi} \frac{e^{-m_\varphi x}}{x}, \tag{1.31}$$

where we employed a radial parametrization of the integration variable and we picked up the pole $q = +im_\varphi$ in contour integration [1]. The massive interactions based on the Yukawa potential approximately satisfy Coulomb's law Eq. (1.21) at small distances. However, they are exponentially surpressed in their real space range. In momentum space the mass term causes convergence of the potential as the distance approaches nill. Scattering processes between states spread out over an extended momentum span are relevant.

Note that the Coulomb potential Eq. (1.27) can be obtained from the Yukawa potential Eq. (1.31) by taking the massless limit, and so can be seen as an infinite range Yukawa potential. A direct comparison between the behavior of these two potentials can be found in Fig. 1.4.
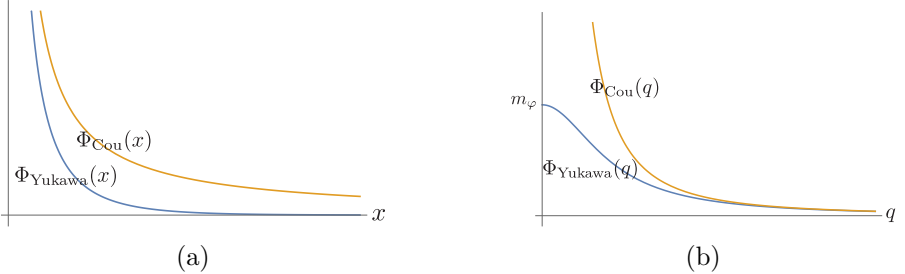

Figure 1.4: Comparison of the behavior of the massless Coulomb potential and Yukawa potential with mass m_φ in both real space and momentum space.

In quantum field theory, electromagnetic interactions between two equally

charged Dirac particles can be implemented in the action as the quartic term

$$
\frac{g^2}{2} \int_{\forall(\omega_i, \mathbf{q}_i)} \Psi^\dagger_{\omega_1, \mathbf{q}_1} \Psi_{\omega_1 - \omega_0, \mathbf{q}_1 - \mathbf{q}_0} D_0(\omega_0, \mathbf{q}_0) \Psi^\dagger_{\omega_2, \mathbf{q}_2} \Psi_{\omega_2 + \omega_0, \mathbf{q}_2 + \mathbf{q}_0}
$$

$$
= \frac{g^2}{2} \sum_{\chi, \chi' = \pm} \int_{\forall(\omega_i, \mathbf{q}_i,)} \psi^{(\chi), \dagger}_{\omega_1, \mathbf{q}_1} \psi^{(\chi)}_{\omega_1 - \omega_0, \mathbf{q}_1 - \mathbf{q}_0} D_0(\omega_0, \mathbf{q}_0) \psi^{(\chi'), \dagger}_{\omega_2, \mathbf{q}_2} \psi^{(\chi')}_{\omega_2 + \omega_0, \mathbf{q}_2 + \mathbf{q}_0}.
$$

$$(1.32)$$

Under the Weyl decomposition it splits up into interactions between excitations within the same Weyl cone for $\chi = \chi'$ plus interactions connecting different cones for $\chi \neq \chi'$. Taking account of the two-fold external leg exchange symmetry and two-fold Weyl degeneracy this action yields the zeroth order transition matrix element [1]

$$
iT(\omega, \mathbf{q}; \omega', \mathbf{q}') \approx 2ig^2 D_0(\omega - \omega', \mathbf{q} - \mathbf{q}'). \tag{1.33}
$$

We can then compare this result to the analogous quantum mechanical calculation. The Born approximation assumes that the coupling ξ of a potential Φ is weak compared to the typical free model energy level, so that the full wavefunction $|f\rangle$ is well approximated by its free cousin $|f^0\rangle$. For a translationally invariant potential, the elements of the transition matrix are then given by [22]

$$
\langle f^0_{\mathbf{q}'} | iT | f^0_{\mathbf{q}} \rangle = \langle f^0_{\mathbf{q}'} | i\,\xi\Phi | f_{\mathbf{q}} \rangle \approx i \int_{\mathbf{x}, \mathbf{x}'} \langle f^0_{\mathbf{q}'} | f^0_{\mathbf{x}'} \rangle \langle f^0_{\mathbf{x}'} | \varsigma\Phi | f^0_{\mathbf{x}} \rangle \langle f^0_{\mathbf{x}} | f^0_{\mathbf{q}} \rangle
$$

$$
= i\xi \int_{\mathbf{x}} \Phi(x) e^{i(\mathbf{q} - \mathbf{q}') \cdot \mathbf{x}} = i\,\xi\Phi(|\mathbf{q} - \mathbf{q}'|). \tag{1.34}
$$

We observe that Eq. (1.32) reproduces the quantum mechanical expression for the scattering of Weyl particles off a electromagnetic potential if we identify the coupling g with the electric charge $Q = Q'$ and the function $D_0(\omega, \mathbf{q})$ in the transition matrix with the potential Φ.

In perturbation theory, corrections enter through the Dyson equation

$$
D(\omega, \mathbf{q}) = \frac{1}{D_0^{-1}(\omega, \mathbf{q}) - \Pi(\omega, \mathbf{q})}. \tag{1.35}
$$

1 Introduction

A constant term $\Pi(0, \mathbf{0})$ in the polarization enters the dressed internal line as an effective mass term m_φ, meaning the potential it corresponds to becomes of the Yukawa type. To lowest order the polarization is given by a simple fermion loop, whose constant part is given by

$$
\begin{aligned}
\Pi(0, \mathbf{0}) &= -(ig)^2 \int_{\omega, \mathbf{q}} \text{Tr}\, G_{0,\chi}(i\omega, \mathbf{q})^2 = (ig)^2 \int_{\omega, \mathbf{q}} \text{Tr}\, \partial_{i\omega} G_{0,\chi}(i\omega, \mathbf{q}) \\
&= (ig)^2 \int_{\omega, \mathbf{q}} \int_{\tilde{\omega}} \partial_{i\omega} \frac{\rho_0(\tilde{\omega}, \mathbf{q})}{-i\omega + \tilde{\omega}} = (ig)^2 \int_{\omega, \mathbf{q}} \int_{\tilde{\omega}} \frac{\rho_0(\tilde{\omega}, \mathbf{q})}{(-i\omega + \tilde{\omega})^2} \\
&= (ig)^2 \int_{\mathbf{q}} \int_{\tilde{\omega}} \rho_0(\tilde{\omega}, \mathbf{q}) \delta(\tilde{\omega}) = -g^2 \rho_0(0), \quad\quad (1.36)
\end{aligned}
$$

where we have taken advantage of the identity

$$
\partial_{i\omega'} G_{0,\chi}(i\omega - i\omega', \mathbf{q} - \mathbf{k}) = -G_{0,\chi}(i\omega - i\omega', \mathbf{q} - \mathbf{k})^2 \quad\quad (1.37)
$$

regarding the frequency derivative of the Green function. The mass-inducing part of the polarization is related to the density of states at Fermi level. In this way, a finite DoS exponentially screens the range of the electromagnetic interactions by inducing an effective mass in the Yukawa potential Eq. (1.31). In a system of Weyl fermions the density of states vanishes at the nodal point as per Eq. (1.20), so that the Coulomb interactions remain unscreened and fall off rapidly as $\sim 1/q^2$ in momentum space. We thus work with

$$
D_0(\omega, \mathbf{q}) = \Phi_{\text{Cou}}(q) = \frac{1}{q^2}. \quad\quad (1.38)
$$

Although in real materials various Weyl cones can be present in the band structure, single cones sit relatively isolated in momentum space [23, 24]. States within the same cone can form arbitrarily close momentum pairs, and processes connecting them form a significant perturbation to the free model. On the other hand the unscreened Coulomb interaction between states in different cones is heavily surpressed by their momentum separation and will be less important.

While it is entirely possible to proceed with the interaction action term Eq. (1.32), at higher order in perturbation theory it results in a large set of diagrams to be evaluated. Instead, we perform a Hubbard-Stratonovich

transformation that brings the action into a more amenable form [2]. Since it integrates to a constant in the partition function, we are free to add the Gaussian action term

$$\frac{1}{2} \int_{\omega,\mathbf{q}} \tilde{\varphi}_{\omega,\mathbf{q}} D_0(\omega,\mathbf{q})^{-1} \tilde{\varphi}_{-\mathbf{q},-\omega}, \tag{1.39}$$

$$\tilde{\varphi}_{\omega,\mathbf{q}} = \varphi_{\omega,\mathbf{q}} + ig \int_{\omega',\mathbf{q}'} \Psi_{\omega',\mathbf{q}'}^{\dagger} \Psi_{\omega,\mathbf{q}'-\mathbf{q}} \, D_0(\omega,\mathbf{q}).$$

This has the effect of decomposing the quartic action term of Eq. (1.32) into a three-point interaction

$$S_{\text{Cou}}[\Psi,\varphi] = ig \int_{\omega,\omega',\mathbf{q},\mathbf{q}'} \varphi_{\omega-\omega',\mathbf{q}-\mathbf{q}'} \, \Psi_{\omega,\mathbf{q}}^{\dagger} \Psi_{\omega',\mathbf{q}'}$$

$$= ig \sum_{\chi=\pm} \int_{\omega,\omega',\mathbf{q},\mathbf{q}'} \varphi_{\omega-\omega',\mathbf{q}-\mathbf{q}'} \, \psi_{\omega,\mathbf{q}}^{(\chi),\dagger} \psi_{\omega',\mathbf{q}'}^{(\chi)} = \sum_{\chi=\pm} S_{\text{Cou}}[\psi^{(\chi)},\varphi] \tag{1.40}$$

plus a term describing the propagation of the intermediate force-carrying bosonic field φ, a massless scalar photon,

$$S_{\varphi}[\varphi] = \frac{1}{2} \int_{\omega,\mathbf{q}} \varphi_{\omega,\mathbf{q}} \, D_0^{-1}(\omega,\mathbf{q}) \, \varphi_{-\omega,-\mathbf{q}}, \qquad D_0(\omega,\mathbf{q}) = q^{-2}. \tag{1.41}$$

Since Eq. (1.40) is a Dirac fermion bilinear it decomposes neatly into left-handed and righthanded Weyl sectors. Breaking up the Coulomb interaction into its fundamental building blocks prunes the number of perturbative correction diagrams to be calculated, which is particularly convenient at higher order or in combination with other perturbations.

1.2.2 Disorder

A Dirac particle moving through a static disordered background has the Hamiltonian $\mathcal{H}_{0,\Psi} - \Gamma V(\mathbf{x})$. By Legendre transform this leads to addition of the element

$$\Gamma \int_{\mathbf{x},\tau} \Psi_{\mathbf{x},\tau}^{\dagger} \, V(\mathbf{x}) \, \Psi_{\mathbf{x},\tau} \tag{1.42}$$

to the free action. The normalized real space potential $V(\mathbf{x})$ can take the shape of an arbitrary and irregular disorder landscape. Saliently it need not be translationally invariant, which rhymes well with the heuristic microscopic picture in which it arises from randomly distributed impurities in a lattice model. We are, however, interested more in the overall properties of disordered models than in the coincidental pecularities of a specific realization. Thinking of V as a function whose statistics are contained in the probability measure $P[V]$, we can average over the disorder potential by performing the functional integral

$$\langle \dots \rangle_{\text{dis}} = \int \mathcal{D}V \, P[V] \, (\dots) \qquad (1.43)$$

Under the condition that various characteristic realizations of the potential are relatively benign, this smooths out the disorder and restores translational invariance. We assume here the disorder potential to be Gaussian distributed over space,

$$P[V] = \exp\left\{ -\frac{1}{2} \int_{\mathbf{x}} V_{\mathbf{x}} V_{\mathbf{x}} \right\}. \qquad (1.44)$$

The choice of the correlation function that is associated with the disorder field is often not critical to the physics of the problem [3, 25], and numerical computations based on different correlation funtions show the same phenomenology as our approach [26, 27]. We therefore consider calculationally convenient white-noise disorder whose Gaussian variance is the short-ranged delta function correlation,

$$\langle V_{\mathbf{x}} \, V_{\mathbf{x}'} \rangle_{\text{dis}} = \delta(|\mathbf{x} - \mathbf{x}'|). \qquad (1.45)$$

In principle, the purpose of any physical theory is to make predictions of the outcome of experiments. Theoretically, such observables $\mathcal{O}$ are obtained by functional differentiation of the free energy $(-\ln Z)$ with respect to an added source J that isolates correlation functions after completing the square. In the context of a disordered background this procedure is obfuscated by the desire to average over the potential realizations. It is not obvious how we could perform the averaging functional integral over a log of the partition function, while if the source differentiation is taken first an

obstructing denominator results [3]. A way out of this quandary is offered by the replica trick, which rewrites the log as the sole surviving term of the vanishing limit of the Taylor expansion of an exponential. For the expectation value of an observable over the disorder ensemble this works out to

$$
\begin{aligned}
\langle \mathcal{O} \rangle_{\text{dis}} &= -\frac{\delta}{\delta J} \langle \ln Z_{V=0} \rangle_{\text{dis}} \Big|_{J=0} = -\frac{\delta}{\delta J} \lim_{R \to 0} \frac{1}{R} \sum_{r=1}^{\infty} \left\langle \frac{(R \ln Z_{V=0})^r}{r!} \right\rangle_{\text{dis}} \Big|_{J=0} \\
&= -\frac{\delta}{\delta J} \lim_{R \to 0} \frac{1}{R} \left\langle e^{R \ln Z_{V=0}} - 1 \right\rangle_{\text{dis}} \Big|_{J=0} \\
&= -\frac{\delta}{\delta J} \lim_{R \to 0} \frac{1}{R} \left\langle Z_{V=0}^R \right\rangle_{\text{dis}} \Big|_{J=0}.
\end{aligned}
\tag{1.46}
$$

In other words, the object of interest in this setting is not the base action of the clean partition function

$$
Z_{V=0} = \int \prod_{X_i \neq V} \mathcal{D} X_i \, \exp\{-S[X, V = 0]\}
\tag{1.47}
$$

itself, but rather the combination of R of its copies and the disorder functional. Because the exponent of the Gaussian measure Eq. (1.44) enters as an free disorder action term

$$
S_V[V] = \frac{1}{2} \int_{\mathbf{q}} V_{\mathbf{q}} V_{-\mathbf{q}},
\tag{1.48}
$$

this defines a disorder-averaged partition function of the form

$$
\begin{aligned}
\bar{Z} &= \lim_{R \to 0} \frac{1}{R} \left\langle Z_{V=0}^R \right\rangle_{\text{dis}} \\
&= \lim_{R \to 0} \frac{1}{R} \int \prod_{X_i \neq V} \prod_{a=1}^{R} \mathcal{D} X_i^{(a)} \exp\left\{ -\sum_{a=1}^{R} S[X^{(a)}, V = 0] \right\} \\
&\quad \times \int \mathcal{D} V \exp\left\{ -\left(S_V[V] + \sum_{a=1}^{R} S_{\text{dis}}[\psi^{(a)}, V] \right) \right\}.
\end{aligned}
\tag{1.49}
$$

The term Eq. (1.42), formerly included in the free action, is reinterpreted as

a three-point interaction between disorder and the fermion replicas

$$
\begin{aligned}
S_{\text{dis}}[\Psi^{(a)}, V] &= \Gamma \int_{\omega, \mathbf{q}, \mathbf{q}'} V_{\mathbf{q}-\mathbf{q}'} \Psi_{\omega, \mathbf{q}}^{(a), \dagger} \, \Psi_{\omega, \mathbf{q}'}^{(a)} \\
&= \Gamma \sum_{\chi = \pm} \int_{\omega, \mathbf{q}, \mathbf{q}'} V_{\mathbf{q}-\mathbf{q}'} \psi_{\omega, \mathbf{q}}^{(\chi, a), \dagger} \, \psi_{\omega, \mathbf{q}'}^{(\chi, a)} = \sum_{\chi = \pm} S_{\text{dis}}[\psi^{(\chi, a)}, V].
\end{aligned}
\tag{1.50}
$$

Note that the field V itself does not obtain a replica index, essentially because $\langle Z_{V=0}^R \rangle_{\text{dis}} \neq \langle Z_{V=0} \rangle_{\text{dis}}^R$. Off-diagonal processes connecting different replicas are possible in this framework. This is also seen explicitly after doing the disorder averaging Gaussian integral, or implementing a field shift

$$
V_{\mathbf{q}} = \tilde{V}_{\mathbf{q}} - \Gamma \sum_{a=1}^{R} \int_{\omega, \mathbf{q}'} \Psi_{\omega, \mathbf{q}'+\mathbf{q}}^{(a), \dagger} \Psi_{\omega, \mathbf{q}'}^{(a)}
\tag{1.51}
$$

in what amounts to a reverse Hubbard-Stratonovich transformation. This impacts the disorder part of the action as

$$
\begin{aligned}
S_V[V] &+ \sum_{a=1}^{R} S_{\text{dis}}[\Psi^{(a)}, V] \\
&= S_V[\tilde{V}] - \frac{\Gamma^2}{2} \sum_{a,b=1}^{R} \int_{\omega_1, \omega_2} \int_{\mathbf{q}, \mathbf{q}_1, \mathbf{q}_2} \Psi_{\omega_1, \mathbf{q}_1+\mathbf{q}}^{(a), \dagger} \Psi_{\omega_1, \mathbf{q}_1}^{(a)} \, \Psi_{\omega_2, \mathbf{q}_2-\mathbf{q}}^{(b), \dagger} \Psi_{\omega_2, \mathbf{q}_2}^{(b)} \\
&= S_V[\tilde{V}] - \frac{\Gamma^2}{2} \sum_{\chi, \chi' = \pm} \sum_{a,b=1}^{R} \int_{\omega_1, \omega_2} \int_{\mathbf{q}, \mathbf{q}_1, \mathbf{q}_2} \psi_{\omega_1, \mathbf{q}_1+\mathbf{q}}^{(\chi, a), \dagger} \psi_{\omega_1, \mathbf{q}_1}^{(\chi, a)} \, \psi_{\omega_2, \mathbf{q}_2-\mathbf{q}}^{(\chi', b), \dagger} \psi_{\omega_2, \mathbf{q}_2}^{(\chi', b)},
\end{aligned}
\tag{1.52}
$$

where $\tilde{V}$ now only appears in the partition function as a Gaussian term and is freely integrated out. This leaves an effective quartic interaction in which the fermions can well belong to different replicas [3]. As a result all diagrams that include a fermion loop connected solely by disorder lines have a free internal replica index that is traced over, giving a factor of R that causes them to vanish in the replica limit. Although it is more standard in the literature to work with the quartic fermionic interaction Eq. (1.52), we instead choose to leave the disorder field unintegrated and proceed with the three-points interaction Eq. (1.50) plus disorder propagator term Eq. (1.48)

The effective quartic interaction term in Eq. (1.52) describes both scattering within the same Weyl cone for $\chi = \chi'$ and processes connecting chiral partner modes for $\chi \neq \chi'$. This includes backscattering effects between the nodes, a fundamental prerequisite for Anderson localization and the implied disorder-induced phase transition into an insulating state [28]. At the Fermi level, however, there are no available states to backscatter into by virtue of the conical dispersion, as testified by the vanishing DoS Eq. (1.20), so that localization cannot occur in the free model.

Nevertheless, the semimetallic state is not entirely impervious to disorder. In the non-crossing approximation, all diagrams contributing to the self-energy can be obtained by inserting the full Green function under a single disorder line. This leads to the self-consistent Born Approximation (SCBA) of the isotropic self-energy,

$$
\overset{\circ}{\Sigma}{}^{\mathrm{SCBA}} = \Gamma^2 \int_{\mathbf{q}}' \left[\overset{\circ}{G}_{0,\chi}^{-1}(0, \mathbf{q}) - \overset{\circ}{\Sigma}{}^{\mathrm{SCBA}} \right]^{-1}
$$

$$
= \Gamma^2 \int_{\mathbf{q}}' [ia\,\sigma_0 - \chi(v\,\mathbf{q} - ib\,\mathbf{d})\cdot\boldsymbol{\sigma}]^{-1} = -\Gamma^2 \int_{\mathbf{q}'}' \frac{ia\sigma_0}{a^2 + v^2 q'^2}, \quad (1.53)
$$

where we have used an ansatz form $\overset{\circ}{\Sigma}{}^{\mathrm{SCBA}} = -ia\,\sigma_0 - ib\,\chi\mathbf{d}\cdot\sigma$. Notationally, the prime on the integral indicates the resulting divergence is handled by implementing a cutoff. This consistency equation always has the trivial solution $a = b = 0$, but also admits a non-trivial solution $a > 0$, $b = 0$ in case the disorder strength Γ exceeds some critical value Γ_c. As a result, the perturbative density of states at Fermi level becomes

$$
\overset{\circ}{\rho}_\chi^{\mathrm{SCBA}}(0) = -\frac{1}{\pi} \operatorname{Im} \operatorname{Tr} \int_{\mathbf{q}}' \left[\overset{\circ}{G}_{0,\chi}^{-1}(0, \mathbf{q}) - \overset{\circ}{\Sigma}{}^{\mathrm{SCBA}} \right]^{-1} = -\frac{1}{\pi\Gamma^2} \operatorname{Im} \operatorname{Tr} \overset{\circ}{\Sigma}{}^{\mathrm{SCBA}}
$$

$$
= \frac{2}{\pi\Gamma^2}\, a \quad \begin{cases} = 0 & \text{if} \quad 0 < \Gamma < \Gamma_c \\ > 0 & \text{if} \quad \Gamma > \Gamma_c. \end{cases} \tag{1.54}
$$

Beyond the critical value Γ_c the disorder induces a phase transition from the free semimetallic (SM) phase with a vanishing DoS into a diffusive metallic (DM) phase with a finite DoS [25, 29, 30], see Fig. 1.5. It should be mentioned that this view is currently challenged by the possibility that rare regions in the potential defy the averaging procedure Eq. (1.43) and lead to an exponentially small but finite DoS even in the SM region of the

phase diagram [31]. Irrespective, at intermediate energy scales the physics should still be controlled by the critical point and associated exponents of the SM-DM phase transition. Once a finite DoS has opened at intermediate disorder the system becomes susceptible to ordinary localization effects by means of backscattering processes between different cones and will eventually transition into an Anderson insulating phase. Note that the required finite DoS and prequisite backscattering between multiple cones both preclude the metal-insulator transition to be studied in the framework of the free Weyl model of Eq. (1.7).
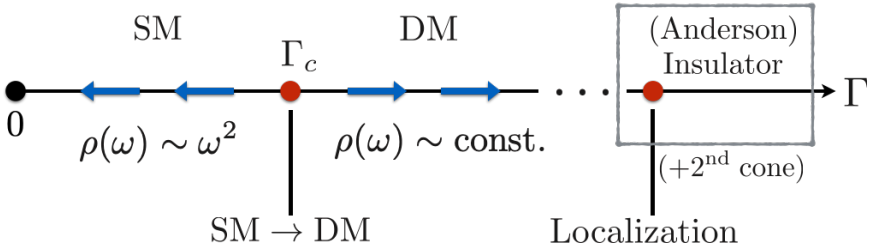
Figure 1.5: One-dimensional phase diagram of the disordered Weyl semimetal.

Naturally, the introduction of distortions in the dispersion will have significant rammifications for the isotropic picture sketched above. We confine ourselves to Type-I Weyl cones, whose subcritical tilts preserve the point-like Fermi surface. As follows from the free DoS in Eq. (1.20) tilts and anisotropies change the number of states available away from the nodal point, making the distorted system more or less susceptible to the effects of disorder level broadening. Thus the critical point of the phase transition between semimetal and diffusive metal, as characterized by the development of a finite density of states, might be expected to shift under such band structure distortions.

On a mathematical level, tilts lead to some interesting calculational complications when combined with perturbative expansion of disorder. Strictly speaking a tilt is a vectorial quantity, and besides its magnitude $0 \leq t < 1$ also implies a unit direction $\mathbf{d}$ will appear in the model that allows for new combinations with the yet existing vectors such as $\mathbf{d} \cdot \mathbf{q}\,\sigma_0$ or $\mathbf{d} \cdot \boldsymbol{\sigma}$. Now, it is a commonly accepted tennet in modern physics that the Lagrangian of a theory should contain all terms permissible by the imposed symme-

tries. Indeed, at first order in perturbation the self-energy contains a term $\sim t\, i\omega\, \mathbf{d} \cdot \boldsymbol{\sigma}$ not originally present in the original Green function in Eq. (1.7), a sign the model is incomplete. Similar issues emerge in the first order vertex correction. Terms capable of absorbing such corrections should be added to the free model to correctly take into acount all contributions. With such additions all possible combinations of vectors, Pauli matrices σ_μ and linear frequency or momentum parameters are represented, completing the model of linearly dispersing tilted Weyl fermions in three dimensions.

We take two subtly different approaches to introducing the requisite terms into the model. In chapter 2 we manually add a new parameter at every occurence of a perturbatively newly generated term. In contrast, in chapter 3 we employ a field transformation

$$\psi_{\omega,\mathbf{q}}^{(\chi)} = \hat{\lambda}^{1/2}\psi_{\omega,\mathbf{q}}^{\prime(\chi)}, \qquad \hat{\lambda} = \sigma_0 - \lambda\chi\, \mathbf{d} \cdot \boldsymbol{\sigma}. \tag{1.55}$$

to introduce a single parameter λ into the model that will prove sufficient to manage all perturbatively generated terms by itself. This is possible only on the realization that the appearance of these terms is associated to perturbative changes to the quasiparticle weight of the fermionic excitations, which will arise identically everywhere their fields are included.

Under transformation Eq. (1.55) the bare Green becomes

$$\begin{aligned} G_{0,\chi}^{\prime-1}(i\omega,\mathbf{q}) &= \hat{\lambda}^{1/2}G_{0,\chi}^{-1}(i\omega,\mathbf{q})\hat{\lambda}^{1/2} \\ &= (i\omega\hat{\lambda} - v't'q_\parallel)\sigma_0 - v'\chi(q_\parallel\mathbf{d} + \eta'\mathbf{q}_\perp) \cdot \boldsymbol{\sigma}. \end{aligned} \tag{1.56}$$

This propagator has the same flavor as the original, with parameters that are related as

$$v' = v\,(1 - t\lambda), \quad \eta' = \eta\,\frac{\sqrt{1 - \lambda^2}}{1 - t\lambda}, \quad t' = \frac{t - \lambda}{1 - t\lambda}, \tag{1.57}$$

or alternatively,

$$v = v'\,\frac{1 + t'\lambda}{1 - \lambda^2}, \quad \eta = \eta'\,\frac{\sqrt{1 - \lambda^2}}{1 + t'\lambda}, \quad t = \frac{t' + \lambda}{1 + t'\lambda}. \tag{1.58}$$

Note that the determinant of the transformed Green function is proportional to the original, $\det G_{0,\chi}' = \det G_{0,\chi}/\det\hat{\lambda}$. Importantly this means that the transformation has no bearing on the excitation energies of the Weyl fermion modes so that it remains given by Eq. (1.8).

1.3 Renormalization Group analysis

In this section we submit the disorder-averaged, Coulomb-interacting Weyl fermion action developed in secs. 1.1-1.2 to Renormalization Group analysis.

For completeness and ease of access, we restate here the action terms found in secs. 1.1-1.2. The full disorder averaged partition function is

$$\bar{Z}^{(\chi)} = \lim_{R \to 0} \frac{1}{R} \prod_{a=1}^{R} Z^{(\chi,a)},$$

$$Z^{(\chi,a)} = \int \mathcal{D}\psi'^{(\chi,a)} \, \mathcal{D}\varphi^{(a)} \, \mathcal{D}V \, \exp\left\{ -S[\psi'^{(\chi,a)}, \varphi^{(a)}, V] \right\}, \qquad (1.59)$$

for a single chiral replica action

$$S[\psi'^{(\chi,a)}, \varphi^{(a)}, V] = S_0[\psi'^{(\chi,a)}, \varphi^{(a)}, V] + S_{\text{int}}[\psi'^{(\chi,a)}, \varphi^{(a)}, V], \qquad (1.60)$$

with a free part

$$S_0[\psi'^{(\chi,a)}, \varphi^{(a)}, V] = S_\psi[\psi'^{(\chi,a)}] + S_\varphi[\varphi^{(a)}] + S_V[V], \qquad (1.61)$$

and interaction terms

$$S_{\text{int}}[\psi'^{(\chi,a)}, \varphi^{(a)}, V] = S_{\text{dis}}[\psi'^{(\chi,a)}, V] + S_{\text{Cou}}[\psi'^{(\chi,a)}, \varphi^{(a)}]. \qquad (1.62)$$

The chirality of a Weyl component is conserved, so that there cannot be terms that would cause it to flip. The action splits into two seperate sections, each describing one of the chiral partners. Although interactions between replicas are possible the replica index is similarly preserved. We can concentrate on a single replica copy as long as we remember to take the vanishing R limit at the end of caclulation.

The free propagation of a chiral Weyl fermion is described by the action

$$S_\psi[\psi'^{(\chi,a)}] = \int_{\omega, \mathbf{q}} \psi'^{(\chi,a),\dagger}_{\omega,\mathbf{q}} \, G'^{-1}_{0,\chi}(i\omega, \mathbf{q}) \, \psi'^{(\chi,a)}_{\omega,\mathbf{q}}. \qquad (1.63)$$

Note that this action includes the fermion field transformation Eq. (1.55), which introduces the matrix $\hat{\lambda} = \sigma_0 - \lambda\chi \, \mathbf{d} \cdot \boldsymbol{\sigma}$ into the inverse Green function

$$G'^{-1}_{0,\chi}(i\omega, \mathbf{q}) = (i\omega\hat{\lambda} - v't'q_\parallel)\sigma_0 - v'\chi(q_\parallel\mathbf{d} + \eta'\mathbf{q}_\perp) \cdot \boldsymbol{\sigma} \qquad (1.64)$$

Figure 1.6: Weyl fermion propagator $G'_{0,\chi}$.

to be able to manage all perturbatively generated terms. Diagramatically, the fermion Green function is represented as in Fig. 1.6.

Coulomb interactions are represented in the action by a term

$$S_{\text{Cou}}[\psi'^{(\chi,a)}, \varphi^{(a)}] = ig \int_{\omega,\omega',\mathbf{q},\mathbf{q}'} \varphi^{(a)}_{\omega-\omega',\mathbf{q}-\mathbf{q}'} \left(\psi'^{(\chi,a),\dagger}_{\omega,\mathbf{q}} \, \hat{\lambda} \, \psi'^{(\chi,a)}_{\omega',\mathbf{q}'} \right), \qquad (1.65)$$

where the propagation of the force-carrying photon is described by

$$S_{\varphi}[\varphi^{(a)}] = \frac{1}{2} \int_{\omega,\mathbf{q}} \varphi^{(a)}_{\omega,\mathbf{q}} \, D_0^{-1}(\omega, \mathbf{q}) \, \varphi^{(a)}_{-\omega,-\mathbf{q}}, \qquad D_0^{-1}(\omega, \mathbf{q}) = q^{d-1-\bar{\epsilon}}, \quad (1.66)$$

where $\bar{\epsilon} \to 0$ is a dimensional regulator that is introduced for technical reasons. Retardation effects are neglected, resulting in an instantaneous Coulomb interaction with a propagator that is constant in frequency or delta function-like under Fourier transformation to a time domain. These action terms are represented in Fig. 1.7a and Fig. 1.7b respectively.

(a)   (b)

Figure 1.7: Tree level three-points Coulomb interaction vertex of a Weyl fermion and scalar photon, and photon propagator D_0.

Averaged disorder comes in by means of the effective interaction term

$$S_{\text{dis}}[\psi'^{(\chi,a)}, V] = \Gamma \int_{\omega,\mathbf{q},\mathbf{q}'} V_{\mathbf{q}-\mathbf{q}'} \left(\psi'^{(\chi,a),\dagger}_{\omega,\mathbf{q}} \, \hat{\lambda} \, \psi'^{(\chi,a)}_{\omega,\mathbf{q}'} \right),$$

where we maintain the dynamic disorder field, whose propagation is contained in

$$S_V[V] = \frac{1}{2} \int_{\mathbf{q}} V_{\mathbf{q}} V_{-\mathbf{q}},$$

in the action instead of integrating it out. We consider quenched disorder with a potential that is constant in time, resulting in a delta function form in the frequency domain. This reflects elastic disorder scattering processes, in which energy is conserved. These action terms are represented in Fig. 1.8a and Fig. 1.8b respectively.

(a)　　　　　　　　　　　　　(b)

Figure 1.8: Tree level three-points disorder interaction vertex of a Weyl fermion and disorder field and the trivial disorder propagator.

1.3.1 Subdivision of field manifold

The most fundamental part of any renormalization group approach is the first step, in which the integration manifold of the fields X_i present in the action is divided into two sets on either side of some arbitrarily set scale,

$$X_i = X_{i,<} + X_{i,>} \qquad \forall i. \tag{1.67}$$

Generally the lesser and greater fields will be coupled in the action, so that high energy processes influence the low energy physics displayed by the system. This mechanism becomes transparent upon integrating out the greater fields $X_{i,>}$ of the action [2],

$$
\begin{aligned}
Z &= \int \mathcal{D}X e^{-S[X]} = \int \mathcal{D}X_< \mathcal{D}X_> \, e^{-S[X_<,X_>]} \\
&= \int \mathcal{D}X_< \, e^{-S_0[X_<]} \int \mathcal{D}X_> \, e^{-S_0[X_>]} \, e^{-S_{\text{int}}[X_<+X_>]} \\
&= \int \mathcal{D}X_< \, e^{-S_0[X_<]} Z_{0;>} \left\langle e^{-S_{\text{int}}[X_<+X_>]} \right\rangle_{0;>} \\
&= \int \mathcal{D}X_< \, e^{-S_{\text{eff}}[X_<]}.
\end{aligned}
\tag{1.68}
$$

Here we have denoted the normalized high energy expectation value of an operator A as

$$\langle A \rangle_{0;>} = Z_{0;>}^{-1} \int \mathcal{D}X_> \, e^{-S_0[X_>]} \, A, \qquad Z_{0;>} = \int \mathcal{D}X_> \, e^{-S_0[X_>]}. \quad (1.69)$$

Anticipating results, we defined $S_{\text{eff}}[X_<]$ as the effective action for the lesser fields at the set scale as the outcome of the greater field integration [2]. It results from the expectation value of the exponential of the interacting term S_{int} that mixes the fields of the two subsets. Expanding in the small couplings of this term, in casu the Coulomb interaction strength g and disorder parameter Γ, yields

$$\left\langle e^{-S_{\text{int}}} \right\rangle_{0;>} = \left\langle 1 + \sum_{n=1}^{\infty} \frac{(-1)^n}{n!} S_{\text{int}}^n \right\rangle_{0;>} = 1 + \sum_{n=1}^{\infty} \frac{(-1)^n}{n!} \langle S_{\text{int}}^n \rangle_{0;>}$$

$$\equiv \exp\left\{ -\sum_{n=1}^{\infty} \frac{(-1)^{n-1}}{n!} \kappa_n \right\}, \quad (1.70)$$

where the cumulants κ_n will be polynomials of the first n non-central moments $\langle S_{\text{int}}^n \rangle_{0;>}$ whose expressions will feed back into the effective action S_{eff} of the lesser fields. Taking the m-th source derivative on both sides of the last equality above shows they are related by the recursive formula [32]

$$\kappa_n = \langle S_{\text{int}}^n \rangle_{0;>} - \sum_{m=1}^{n-1} \binom{n-1}{m-1} \kappa_m \left\langle S_{\text{int}}^{n-m} \right\rangle_{0;>}. \quad (1.71)$$

It is an exercise in substitution to show that the first few cumulants κ_n of the expansion are given explicitly by

$$\kappa_1 = \langle S_{\text{int}} \rangle_{0;>},$$
$$\kappa_2 = \left\langle S_{\text{int}}^2 \right\rangle_{0;>} - \langle S_{\text{int}} \rangle_{0;>}^2,$$
$$\kappa_3 = \left\langle S_{\text{int}}^3 \right\rangle_{0;>} - 3 \langle S_{\text{int}} \rangle_{0;>} \left\langle S_{\text{int}}^2 \right\rangle_{0;>} + 2 \langle S_{\text{int}} \rangle_{0;>}^3. \quad (1.72)$$

Note that these cumulant expressions can also be obtained by re-exponentiating the upper line of Eq. (1.70) and Taylor expanding the resultant logarithm.

1.3.2 Free scaling and power counting

Suppose first that there are no correlations between fields at different energy scales, $S_{\text{int}} = S_{\text{int}}[X_<] + S_{\text{int}}[X_>]$, and the effective theory of the lesser fields is unaffected by greater field integration. By Eq. (1.69) higher field expectation values reduce to just the lesser field operator and so the effective action is nothing more than the regular action,

$$\left\langle e^{-S_{\text{int}}[X_<]} e^{-S_{\text{int}}[X_>]} \right\rangle_{0;>} \sim e^{-S_{\text{int}}[X_<]}, \qquad S_{\text{eff}}[X_<] = S[X_<]. \qquad (1.73)$$

Notably, this trivially holds true for the non-interacting case where $S_{\text{int}} = 0$, at zeroth order in the expansion Eq. (1.70) . The only dependence of the model's fields X_i and parameters y_i on the mass scale μ is contained in their respective scaling dimensions $[X_i]$ and $[y_i]$. These may be determined by insisting that the model action remains invariant under an anisotropic spacetime rescaling

$$\omega \to \mu^{+z}\, \omega, \qquad\qquad \mathbf{q} \to \mu^{+1}\, \mathbf{q} \qquad\qquad (1.74)$$

that brings out explicitly the dimensionality of the integration variables. Here, the dynamical exponent z determines the effective dispersion relation between frequency and momentum that may come to deviate from unity under renormalization [3]. Under these transformations, the components of the free action change as

$$S_\psi[\psi'] \to \int_{\omega,\mathbf{q}} \mu^{+(d+z)}\mu^{+2[\psi_{\omega,\mathbf{q}}]} \psi^\dagger_{\omega,\mathbf{q}} \left[\mu^{+z} i\omega(\sigma_0 - \mu^{+[\lambda]}\lambda\chi \mathbf{d}\cdot\boldsymbol{\sigma}) \right.$$
$$\left. - \mu^{+1}\mu^{+[v]}v\left(\mu^{+[t]} t\, q_\parallel\sigma_0 + \chi(q_\parallel\mathbf{d} + \mu^{+[\eta]}\eta\,\mathbf{q}_\perp)\cdot\boldsymbol{\sigma}\right) \right] \psi_{\omega,\mathbf{q}},$$

$$S_\varphi[\varphi] \to \frac{1}{2}\int_{\omega,\mathbf{q}} \mu^{+(d+z)}\mu^{+(d-1-\bar{\epsilon})}\mu^{+2[\varphi_{\omega,\mathbf{q}}]} \varphi_{\omega,\mathbf{q}}\, q^{d-1-\bar{\epsilon}}\, \varphi_{-\omega,-\mathbf{q}},$$

$$S_V[V] \to \frac{1}{2}\int_{\mathbf{q}} \mu^{+d}\mu^{+2[V_{\mathbf{q}}]} V_{\mathbf{q}} V_{-\mathbf{q}}.$$

This yields a system of equations that can be solved in sequence. The dimensionalities of the fields can be obtained from the parameterless leading operator term. This shows that

$$[\psi_{\omega,\mathbf{q}}] = -\frac{1}{2}(d+2z), \qquad [\varphi_{\omega,\mathbf{q}}] = -\frac{1}{2}(2d+z-1-\bar{\epsilon}), \qquad [V_{\mathbf{q}}] = -\frac{d}{2}.$$
$$(1.75)$$

Knowing the field dimensions it is straightforward to find that the free sector parameters should have scaling dimensions

$$
\begin{aligned}
[v] &= -(d + 1 + z + 2[\psi_{\omega,\mathbf{q}}]) = z - 1, \\
[t] &= [\eta] = [\lambda] = -(d + 1 + z + 2[\psi_{\omega,\mathbf{q}}] + [v]) = 0.
\end{aligned}
\tag{1.76}
$$

Progressing to first order in perturbation in Eq. (1.70) gives

$$
\langle S_{\text{int}}[X_< + X_>]\rangle_{0;>} = S_{\text{int}}[X_<] + \dots.
\tag{1.77}
$$

The resulting term $S_{\text{int}}[X_<]$ is just the interacting part Eq. (1.62) of the lesser field action, graphically represented as tree level vertices without internal lines. This is a restatement of the obvious fact that at tree level the only connected diagrams that contribute are the unadorned interaction vertices themselves. Two tadpole diagrams, fermion loops with a single external Coulomb or disorder line, deliver a contribution to the vacuum expectation value of the lesser fields. Picking the fields appropriately gaurantees that these terms will vanish, and accordingly we here neglect them.

Thus at first order the only scale dependence of the couplings is contained in their mass dimension. Making it explicit to counteract the anisotropic rescaling procedure Eq. (1.74) yields

$$
\begin{aligned}
S_{\text{Cou}}[\psi', \varphi] &\to i g \, \mu^{+[g]} \int_{\omega,\omega'\mathbf{q},\mathbf{q}'} \mu^{+(2d+2z)} \mu^{+[\varphi_{\omega,\mathbf{q}}]} \mu^{+2[\psi_{\omega,\mathbf{q}}]} \varphi_{\omega-\omega',\mathbf{q}-\mathbf{q}'} \\
&\quad \left(\psi_{\omega,\mathbf{q}}'^{\dagger} (\sigma_0 - \mu^{+[\lambda]} \lambda \chi \mathbf{d} \cdot \boldsymbol{\sigma}) \psi_{\omega',\mathbf{q}'}' \right), \\
S_{\text{dis}}[\psi', V] &\to \Gamma \, \mu^{+[\Gamma]} \int_{\omega,\omega'\mathbf{q},\mathbf{q}'} \mu^{+(2d+z)} \mu^{+[V_{\mathbf{q}}]} \mu^{+2[\psi_{\omega,\mathbf{q}}]} V_{\mathbf{q}-\mathbf{q}'} \\
&\quad \left(\psi_{\omega,\mathbf{q}}'^{\dagger} (\sigma_0 - \mu^{+[\lambda]} \lambda \chi \mathbf{d} \cdot \boldsymbol{\sigma}) \psi_{\omega,\mathbf{q}'}' \right).
\end{aligned}
$$

Including the field zeroth order scaling Eq. (1.75), invariance of the interacting action is achieved by coupling scaling dimensions

$$
\begin{aligned}
[g] &= -(2d + 2z + [\varphi_{\omega,\mathbf{q}}] + 2[\psi_{\omega,\mathbf{q}}]) = \frac{1}{2}(z - 1 - \bar{\epsilon}), \\
[\Gamma] &= -(2d + z + [V_{\mathbf{q}}] + 2[\psi_{\omega,\mathbf{q}}]) = z - \frac{d}{2}.
\end{aligned}
\tag{1.78}
$$

Nominally we are interested in Weyl fermions in a $(d + 1)$-dimensional spacetime where $d = 3$. The free model is characterized by the ordinary values $\bar{\epsilon} = 0$ and $z = 1$, to which the Coulomb interactions presents a marginal perturbation whose scaling is determined fully by interaction effects. Differently disorder is irrelevant in the renormalization group sense, implying scaling towards the clean model until perturbative interaction contributions start to dominate.

1.3.3 Interaction scaling

Higher orders in the perturbative expansion Eq. (1.70) of the interaction couplings can change the effective dimensionality of the parameters and thus efffect their scaling behavior under flow of the renormalization scale μ. The terms that so arise have a more convenient pictorial interpretation in terms of Feynman diagrams, with higher orders characterized by progessively more intersecting vertices. External lines in these diagrams correspond to lesser fields. Internal lines, whose frequencies and momenta are integrated over, represent two-points expectation values of the greater fields that translate into the corresponding Green functions by a source differentation mechanism.

In the recursive relation of Eq. (1.71) the first term on the right-hand side produces all the diagrams conceivable at some order through Wick's theorem. The second term then substracts from these certain classes of graphs that can be constructed from previous orders. By this mechanism all disconnected diagrams, those graphs that factorize into several disjoint subgraphs, are cancelled from the expansion. Contributions can come only from the connected diagrams, in which all Green functions and vertices form a single linked cluster [3].

At higher order we can distinguish two classes of diagrams that contribute to the renormalized two-points function. One-particle irreducible (1PI) diagrams are graphs with an internal structure of lines, by which they do not decompose into two valid subgraphs when a single internal line is cut. Other diagrams are simple repeats of 1PI units, connected by internal lines. The full contribution to the two-points function can then be written as a geometric series of an increasing 1PI insertions on the respective propagator

line,

$$= \sum_{n=0}^{\infty}\big) \left(\Sigma' G'_{0,\chi}\right)^n \Sigma' = \left(1 - \Sigma'\, G'_{0,\chi}\right)^{-1}\Sigma',$$

$$= \sum_{n=0}^{\infty}\big) \left(\Pi D_0\right)^n \Pi = \left(1 - \Pi\, D_0\right)^{-1}\Pi. \tag{1.79}$$

Loops similarly arise in two different ways in the vertex corrections at higher order. Amputated diagrams have loops only internally in an 1PI core, to which only unadorned external lines connect. On the other hand there will arise diagrams that are manifestly not 1PI due to loops on individual external legs. Sequences of such loops are similarly resummed as the two points function,

$$= \sum_{n=0}^{\infty} \left(\Sigma'\, G'_{0,\chi}\right)^n = \left(1 - \Sigma'\, G'_{0,\chi}\right)^{-1},$$

$$= \sum_{n=0}^{\infty} \left(\Pi\, D_0\right)^n = \left(1 - \Pi\, D_0\right)^{-1}. \tag{1.80}$$

By this token these geometric factors appear everywhere where a lesser field is included, and so they amount to an overall factor that can be freely incorporated by a global rescaling of the fields. Dividing the fields by the respective higher-point external line factor results in the conclusion that significant deviations from the bare propagator form arising due to perturbations are given by the Dyson equations

$$G'^{-1}_\chi = G'^{-1}_{0,\chi} - \Sigma', \qquad D^{-1} = D_0^{-1} - \Pi. \tag{1.81}$$

We thus conclude that we efficiently incorporate all perturbative contributions by considering all possible Feynman diagrams that are simply con-

nected and one-particle irreducible. As a general rule this includes higher-point vertex function diagrams not originally present in the action. Fortunately these will be progessively more RG irrelevant the more external legs are attached, and are therefore safely neglected [3]. Similarly disregarded is a zoo of further tadpole-style diagrams, which will only produce inconsequential shifts in the vacuum expectation value of the fields.

Even orders in the expansion will consist of terms contributing to the renormalization of the free propagation action terms Eq. (1.61) of the lesser fields. The first such significant corrections to the free model are the 1PI connected diagrams listed in Fig. 1.9 arising at one loop order, corresponding to second order in the expansion Eq. (1.70). Further graphs include a disorder polarization contribution with a free replica index on its fermion loop, which vanishes in the replica limit $R \to 0$. Another fermion loop, interpolating between a Coulomb external line and a disorder external line, will prove to be irrelevant.
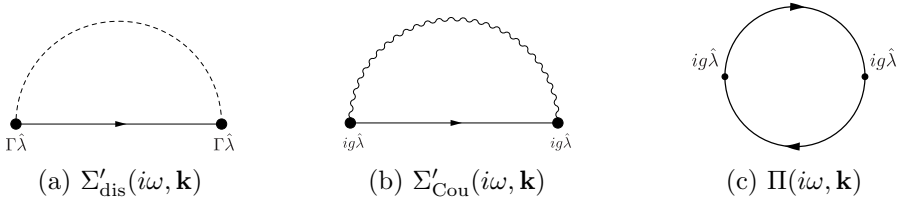
Figure 1.9: 1PI self-energy corrections to the fermion Green function G'_0 and polarization contributing to renormalization of photon propagator D_0.

Corrections to the three-points Coulomb and disorder vertices come in at odd orders in the expansion Eq. (1.70). Contributions to the vertex couplings come purely from those diagrams whose legs have been amputated, and have loops only internally in an 1PI core [1]. The first such significant corrections to the interaction part of the action are the amputated vertex diagrams listed in Figs. 1.10-1.11, arising at one loop order or third order in the perturbative expansion. Similar to the two-point case there is also a further mixed fermion loop graph, interpolating between an internal disorder line and an external Coulomb line, which is irrelevant to the RG.
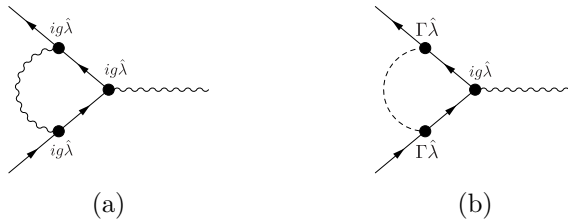
Figure 1.10: Vertex corrections to the Coulomb coupling g.
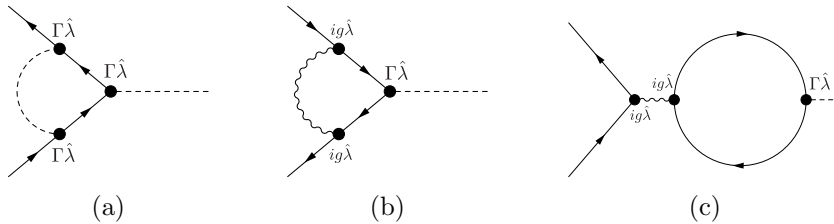
Figure 1.11: Vertex corrections to disorder coupling Γ.

1.3.4 Renormalization group schemes

In this Subsection we discuss two renormalization group schemes that are common to the literature. In essence, these schemes are prescriptions that instruct how to manage the nominally divergent integrals, pictorially represented as Feyman diagrams, that arise from the expansion of interaction terms perturbing a free model.

Wilsonian Momentum Shell RG

The Wilsonian approach to renormalization relies on a procedure that changes the initial action in such a way that it may be compensated for by a redefinition of the model parameters [33, 34]. First, greater fields $X_>$ are integrated out of the action $S[X]$ with a hard cutoff Λ to regulate the emerging divergencies. This also changes the domain of integration in the action, which is counteracted by a rescaling of the integration variables. Containing the same operator terms as the original the resultant action is self-similar, albeit with parameter coefficients transfigured by their dimensionality as well as by the diagrammatic contributions stemming from the greater field integration [2].

1 Introduction

First of all, the subdivision of the field manifold set out in Eq. (1.67) is formalized as

$$X_{i,<} = X_{i,<}(\omega, \mathbf{q} \mid 0 < q < b\Lambda),$$
$$X_{i,>} = X_{i,>}(\omega, \mathbf{q} \mid b\Lambda < q < \Lambda), \qquad (1.82)$$

where $b < 1$ is a dimensionless parameter. Functional integration of the higher fields out of the partition function results in the set of Feyman diagrams set out in Subsec. 1.3.3, that now encode regularized integrations within a cylindrical momentum shell between $b\Lambda$ and original cutoff Λ. Formally this parametrization [35], which we indicate by a prime on the integral, is taken to be

$$
\begin{aligned}
\int_{\mathbf{q}}' \ldots &= \int_{-\pi}^{\pi} \frac{\mathrm{d}\phi}{2\pi} \int_{-\infty}^{\infty} \frac{\mathrm{d}q_{\parallel}}{2\pi} \int_{\mu=b\Lambda}^{\Lambda} \frac{\mathrm{d}q_{\perp}}{2\pi} \, q_{\perp} \ldots \\
&\approx \frac{\Lambda}{(2\pi)^2} \int_{-\pi}^{\pi} \frac{\mathrm{d}\phi}{2\pi} \int_{-\infty}^{\infty} \mathrm{d}q_{\parallel} \ldots \Big|_{q_{\perp}=\Lambda} \int_{\mu=b\Lambda}^{\Lambda} \mathrm{d}q_{\perp} \\
&= \frac{\Lambda^2(1-b)}{(2\pi)^2} \int_{-\pi}^{\pi} \frac{\mathrm{d}\phi}{2\pi} \int_{-\infty}^{\infty} \mathrm{d}q_{\parallel} \ldots \Big|_{q_{\perp}=\Lambda} \\
&\approx \frac{\Lambda^2 l}{(2\pi)^2} \int_{-\pi}^{\pi} \frac{\mathrm{d}\phi}{2\pi} \int_{-\infty}^{\infty} \mathrm{d}q_{\parallel} \ldots \Big|_{q_{\perp}=\Lambda}. \qquad (1.83)
\end{aligned}
$$

Assuming here that the momentum interval is a thin shell of infinitesimal width $l = \ln b^{-1} \ll 1$, the integrand may be well approximated by the constant radius Λ. The 1PI self-energy diagrams contribute to the free action via the Dyson equation (1.81), while the amputated vertex diagrams offer corrections to the interacting part of the action. In general the expressions proceeding from the evaluation of the diagrams will contain terms with higher powers of frequency or momentum, which will be irrelevant in the RG sense and may be neglected.

After integrating out the greater fields the action that remains is defined in terms of the lesser fields $X_{i,<}$ with momenta limited to lowered cutoff $b\Lambda = e^{-l}\Lambda$. Scaling of the integration variables

$$\omega \to b^{+z}\omega = e^{-zl}\omega, \qquad\qquad \mathbf{q} \to b^{+1}\mathbf{q} = e^{-l}\mathbf{q} \qquad (1.84)$$

brings the cutoff back to its original value. We should then also rescale the fields to put them back up to the original scale,

$$X_{i,<} \to b^{+[X_i]} Z_{X_i}^{-1} X_{i,<} = e^{-[X_i]l} Z_{X_i}^{-1} X_{i,<}. \tag{1.85}$$

Here, the field renormalization factors $Z_{X_i}^{-1}$ are chosen in such a way that they eliminate the self-energy contributions to the leading operator terms in the free action. Finally, we define new scale-dependent parameters

$$y_i(l) = b^{-[y_i]} Z_{y_i} y_i = e^{+[y_i]l} Z_{y_i} y_i \tag{1.86}$$

by identifying them with the remaining terms. The parameter renormalization factors then Z_{y_i} absorb the selected pictorial contributions of the appropriate operator terms, discounted by the appropriate field factors. The action has now regained its original form, albeit with different parameters that have come to depend on the result of the integration. Combining the greater field integration with rescaling of parameters and fields amounts to performing a transformation of the action. Repeating this operation is akin to following a trajectory of flow in the associated parameter space [1]. This results in a set of differential equations, the (ultraviolet) β functions,

$$\beta_{y_i} = -b\frac{\mathrm{d}y_i(l)}{\mathrm{d}b} = \frac{\mathrm{d}y_i(l)}{\mathrm{d}l} = \frac{\mathrm{d}}{\mathrm{d}l}\left(e^{+[y_i]l} Z_{y_i} y_i\right) = y_i(l)\left([y_i] + Z_{y_i}^{-1}\frac{\mathrm{d}Z_{y_i}}{\mathrm{d}l}\right)$$
$$\approx y_i(l)\left([y_i] + \frac{\mathrm{d}(Z_{y_i} - 1)}{\mathrm{d}l}\right) \tag{1.87}$$

that describe how the parameters of the model flow as the momentum cutoff is decreased. Note that such corresponds to increasing the shell thickness l, and that their differential equations carry the opposite sign.

Although the Wilsonian renormalization group provides an intuitive picture to understand the scaling of parameters with the change of energy scale, it has several drawbacks. Most saliently among these is its tendency to artificially break the gauge symmetries of the model under consideration. The hard cutoff Λ imposed on the integrals in the cylindrical momentum shell scheme Eq. (1.83) disallows the rescaling of the integration variable that is instrumental to the development of the requisite Ward identities [1]. The current set-up was consequently found sufficient for the disorder-only Weyl fermion problem treated in chapter 2, but proved ill-suited when electromagnetic interactions are added as in chapter 3.

Counterterm RG and Dimensional Regularization

Rather than looking at the theory as a general concept with a self-similar structure, the counterterm approach to the renormalization group postulatest that a renormalizable effective model exists at a certain renormalization scale and studies how the Green functions, ultimately related to observables, change with its variation. By the way of Eq. (1.68), any such renormalized model requires divergences coming from degrees of freedom at higher scales to be neutralized and incorporated. This is done by the introduction of counterterms into the model, which are treated as further perturbations in their own right. The counterterms may then be chosen such that they exactly cancel the divergent contributions at the renormalization scale, keeping the renormalized parameters finite. Small variations of the renormalization scale lead to changes in the fields and parameters that should be counteracted by adjustments to the counterterms, as summarized in the Callan-Symanzik equation for the Green functions of the theory. We can finally use this relation to find the β functions of the parameters in an order by order approximation.

Anticipating the emergence of divergent terms in a pertubative expansion of the action we employ multiplicative renormalization constants as

$$y_{i,B} = Z_{y_i}\, y_i, \qquad\qquad Z_{y_i} = 1 + \delta_{y_i},$$
$$X_{i,B} = Z_{X_i}\, X_i, \qquad\qquad Z_{X_i} = 1 + \delta_{X_i}, \qquad (1.88)$$

to change from bare to renormalized fields and parameters. Here, the δ_{y_i} and δ_{X_i} are counterterms that should be interpreted as further perturbations to the model that will result in additional diagrams beyond those in Figs. 1.9-1.11. We treat the divergent integrals that arise in the calculation of these diagrams by analytical continuation of the number of dimensions to non-integer values [36]. Expanding around the disorder marginal dimension as $d = 2 + \epsilon$ captures corresponding infinities as poles $\sim \Omega^\epsilon/\epsilon$ with Ω symbolizing the external energy scale at which the diagram is computed. At the end of all calculations, the limit $\epsilon \to 1$ should be taken in order for results to apply to three dimensional Weyl fermions. Note that the Coulomb interaction is defined as Fourier transform of the potential $1/x$ and so constitutes a marginal perturbation indendent of number of spatial dimensions. Divergences arising from perturbation in its coupling cannot be accounted

for by the same dimensional expansion as disorder. We therefore implement a dimensional regulator $\bar{\epsilon}$ on its propagator as $q^{d-1-\bar{\epsilon}}$ as set out in Eq. (1.66), which similarly captures the corresponding infinities. At the end of all calculations, taking the the limit $\bar{\epsilon} \to 0$ is sufficient to return us to the three-dimensional case. It is noteworthy to remark here that this dimensional regularization scheme is known to respect the gauge invariance characteristic of electrodynamic theories [1].

If a physical theory is to describe reality, it should be possible to express it in terms of a finite limit set of renormalized parameters at some renormalization scale μ. This imposes renormalization conditions on all n-point functions, which specify how the counterterms should be chosen so that their diagrams exactly cancel the regular diagrams. In essence, setting the counterterms to balance out divergent contributions defines a theory at a given scale.

For the counterterm framework set out by Eq. (1.88) the chosen renormalization scale is essentially aribitrary from a technical point of view. It is important only in making experimentally verifiable quantitative predicitions, but has little bearing on general qualitative aspects with which we are concerned here. We might equally well have picked another renormalization scale without impacting the calculations, although the counterterms would also need to be numerically different in compensation. For small shifts of the renormalization scale and corresponding changes of the fields and parameters

$$\mu \to \mu + \Delta\mu, \qquad y_i \to y_i + \Delta y_i, \qquad X_i \to (1 + \Delta X_i)X_i, \qquad (1.89)$$

the adjustment of a fully connected and amputated $\{n_{X_j}\}$-points Green function is determined by the field rescaling,

$$\mathcal{G}^{(\{n_{X_j}\})} \to \prod_j (1 + \Delta X_j)^{n_{X_j}} \mathcal{G}^{(\{n_{X_j}\})} \approx \left(1 + \sum_j n_{X_j} \Delta X_j\right) \mathcal{G}^{(\{n_{X_j}\})}.$$

$$(1.90)$$

For a generic renormalized Green function $\mathcal{G}^{(\{n_{X_j}\})} = \mathcal{G}^{(\{n_{X_j}\})}(\mu; \{y_i\})$, defined at scale μ and depending on the parameters in the set $\{y_i\}$, this trans-

formation yields the equation

$$\mathrm{d}\mathcal{G}^{(\{n_{X_j}\})} = \frac{\mathrm{d}\mathcal{G}^{(\{n_{X_j}\})}}{\mathrm{d}\mu}\Delta\mu + \sum_i \frac{\mathrm{d}\mathcal{G}^{(\{n_{X_j}\})}}{\mathrm{d}y_i}\Delta y_i = \sum_j n_{X_j}\,\Delta X_j\,\mathcal{G}^{(\{n_{X_j}\})}.$$

(1.91)

Multiplying through by $\mu/\Delta\mu$ leads to the Callan-Symanzik (CS) equation [37, 38]

$$\left[\mu\frac{\mathrm{d}}{\mathrm{d}\mu} - \sum_i \beta_{y_i}\frac{\mathrm{d}}{\mathrm{d}y_i} + \sum_j n_{X_j}\,\gamma_{X_j}\right]\mathcal{G}^{(\{n_{X_j}\})}\left(\mu; \{y_i\}\right) = 0.$$

(1.92)

Note that in the case of a Weyl fermion model this is a matrix equation in 2×2 Pauli space, and so contains several scalar relations. The CS equation describe how a shifts of the renormalization scale μ is compensated for by changes in the parameters encapsulated in the (ultraviolet) flow equation

$$\beta_{y_i} \equiv -\frac{\mu}{\Delta\mu}\Delta y_i = -\frac{\mu}{\Delta\mu}\left(\frac{(\mu+\Delta\mu)^{-[y_i]}Z_{y_i}^{-1}(\mu+\Delta\mu)}{\mu^{-[y_i]}Z_{y_i}^{-1}(\mu)} - 1\right)y_i(\mu)$$

$$= y_i\left([y_i] + \frac{\mu}{Z_{y_i}}\frac{\mathrm{d}}{\mathrm{d}\mu}Z_{y_i}\right),$$

(1.93)

plus modifications to the field strength captured by

$$\gamma_{X_i} \equiv -\frac{\mu}{\Delta\mu}\delta X_i = -\frac{\mu}{\Delta\mu}\left(\frac{Z_{X_i}^{-1}(\mu+\Delta\mu)}{Z_{X_i}^{-1}(\mu)} - 1\right) = \frac{\mu}{Z_{X_i}}\frac{\mathrm{d}}{\mathrm{d}\mu}Z_{X_i}.$$

(1.94)

In our set-up, we then find to one loop order that the universal functions reduce to

$$\beta_{y_i} = y_i\left([y_i] + \mu\frac{\mathrm{d}}{\mathrm{d}\mu}\delta_{y_i}\right), \qquad \gamma_{X_i} = \mu\frac{\mathrm{d}}{\mathrm{d}\mu}\delta_{X_i}.$$

(1.95)

Note that this agrees with the exact relation Eq. (1.93) above to leading order. The functions β_{y_i} and γ_{X_i} do not depend on any renormalization scale but are expressed completely in terms of the renormalized parameters and their scaling dimensions. They contain important information on the

stability of the model at various renormalization scales. If the function β_{y_i} is negative, the parameter y_i will exponentionally decrease upon lowering the renormalization scale. At lower scales then, such parameters might as well be excluded from an efficient description of the system. In contrast, positive values of $\beta_{y_i} > 0$ indicate that the flow is towards larger parameter values that will come to dominate the theory when going to lower renormalization scales. Only if the function vanishes, $\beta_{y_i} = 0$, the parameter value is independent of the scale at which the system is investigated. If this holds for all parameters the model is at a fixed point, where it is completely scale-invariant. This means that all model dependent physics can be scaled away, and only universal behavior remains. These traits are determined by a set of model-independent exponents that sort all fixed points into a limited number of universality classes. Importantly, included in the exponents is information on the orientation of the flow around the point. Tuning the parameters of a system at a fixed scale to take it across a repulsive fixed point abruptly changes the flow directionality, associating it with a different attractive fixed point at which it displays wildly different behavior. This is the hallmark of a phase transition.

1.4 Quantum Electrodynamics in the non-relativistic limit

In this section we investigate more closely how the model we study in the following chapters is derived from quantum electrodynamics (QED), and is thus subject to all the symmetries and identities particular to that theory. We start from the familiar massless Dirac Lagrangian

$$\mathcal{L}_\Psi = -ic\,\bar{\Psi}\left[\gamma^\mu \partial_\mu\right]\Psi = -i\,\Psi^\dagger\left[\partial_t + c\,\gamma^0\boldsymbol{\gamma}\cdot\boldsymbol{\nabla}\right]\Psi$$
$$= c\,\Psi^\dagger\left[q_0 + \gamma^0\boldsymbol{\gamma}\cdot\mathbf{q}\right]\Psi, \tag{1.96}$$

where we have reinstated the speed of light c and have defined the momentum operator as $q_\mu = -i\partial_\mu = -i(\partial_t/c, \boldsymbol{\nabla})$. Variation with respect to the conjugate field $\bar{\Psi}$ leads to the massless Dirac equation, introduced in Eq. (1.1), as equation of motion. The Lagrangian appropriate to quantum electrodynamics, the relativistic field theory describing the way fermionic matter interacts with light, is given by

$$\mathcal{L}_{\mathrm{QED}} = \mathcal{L}_\Psi|_{\delta_\mu \to D_\mu} + \mathcal{L}_A, \tag{1.97}$$

and is traditionally obtained by submitting the Dirac Lagrangian Eq. (1.96) to the minimal substitution procedure

$$\partial_\mu \to D_\mu = \partial_\mu + \frac{iQ}{c}(A_\mu + B_\mu). \tag{1.98}$$

This results in a term

$$\mathcal{L}_\Psi|_{\delta_\mu \to D_\mu} = -ic\,\bar{\Psi}\left[\gamma^\mu D_\mu\right]\Psi$$
$$= \Psi^\dagger\left[-i\partial_t + Q(A_0 + B_0) + \gamma^0\boldsymbol{\gamma}\cdot(-ic\boldsymbol{\nabla} + Q(\mathbf{A} + \mathbf{B}))\right]\Psi$$
$$= \Psi^\dagger\left[i\omega + Q(A_0 + B_0) + \gamma^0\boldsymbol{\gamma}\cdot(c\,\mathbf{q} + Q(\mathbf{A} + \mathbf{B}))\right]\Psi. \tag{1.99}$$

Here A_μ is the four-potential of the electromagnetic field, whose free propagation is contained in the Lagrangian

$$\mathcal{L}_A = -\frac{1}{4}F_{\mu\nu}F^{\mu\nu}, \qquad\qquad F_{\mu\nu} = \partial_\mu A_\nu - \partial_\nu A_\mu. \tag{1.100}$$

The coupling of the four-potential and the fermion is determined by the charge Q of the model under the $U(1)$ local gauge transformation

$$\Psi \to e^{i\theta}\Psi, \qquad A_\mu \to A_\mu - \frac{c}{Q}\partial_\mu\theta, \qquad \theta = \theta(x_\mu). \qquad (1.101)$$

A field B_μ introduced by an external source couples identically to the fermion field, while its kinetics are outside the model. QED is well-known to contain certain rules that protect the form of the minimal coupling between derivative and gauge field in Eq. (1.98) even in perturbation theory [1]. Its Ward identities, resulting from the gauge invariance of the model, establish relations between different classes of diagrams that then conspire to ensure non-renormalization of group charge Q.

Unlike the fundamental particles described by the Dirac equation in QED, Linearly-dispersing Dirac and Weyl fermions encountered in material band structures in condensed matter settings are non-relativistic and propagate at Fermi velocity v much lower than c. The bosons mediating the electromagnetic interaction however are no different, and by defintion move at the speed of light. This leaves the minimal substitution mechanism of Eq. (1.98) unchanged, resulting in the non-relativistic Lagrangian

$$\mathcal{L}^{\mathrm{NR}}_{\mathrm{QED}} = \mathcal{L}^{\mathrm{NR}}_{\Psi}\big|_{\delta_\mu \to D_\mu} + \mathcal{L}^{\mathrm{NR}}_{A}, \qquad (1.102)$$

The fermionic term becomes

$$\begin{aligned}
\mathcal{L}^{\mathrm{NR}}_{\Psi}\big|_{\delta_\mu \to D_\mu} &= -i\,\Psi^\dagger \left[c\,D_0 + v\gamma \cdot \mathbf{D}\right]\Psi \\
&= \Psi^\dagger \left[-i\partial_t + Q(A_0 + B_0) + \gamma^0\boldsymbol{\gamma} \cdot \left(-iv\boldsymbol{\nabla} + \frac{v}{c}Q(\mathbf{A} + \mathbf{B})\right)\right]\Psi \\
&\approx \Psi^\dagger \left[-i\partial_t + Q(A_0 + B_0) - iv\,\gamma^0\boldsymbol{\gamma} \cdot \boldsymbol{\nabla}\right]\Psi \\
&= \Psi^\dagger \left[i\omega + Q(A_0 + B_0) + v\,\gamma^0\boldsymbol{\gamma} \cdot \mathbf{q}\right]\Psi \qquad (1.103)
\end{aligned}$$

where we have kept only terms at zeroth order in an expansion of $v/c \ll 1$. Taking the same non-relativistic approximation on the four-potential term

in the Lagrangian yields

$$
\begin{aligned}
\mathcal{L}_A^{\mathrm{NR}} &= -\frac{1}{4} F_{\mu\nu} F^{\mu\nu} = -\frac{1}{4} \left(2 F_{0i} F^{0i} + F_{ij} F^{ij} \right) \\
&= -\frac{v^2}{2c^2} \left(\frac{\partial_t}{v} \mathbf{A} \right)^2 + \frac{1}{2} \left(\boldsymbol{\nabla} A_0 \right)^2 - \frac{v}{c} \left(\boldsymbol{\nabla} A_0 \right) \cdot \left(\frac{\partial_t}{v} \mathbf{A} \right) - \frac{1}{4} F_{ij} F^{ij} \\
&\approx \frac{1}{2} \left(\boldsymbol{\nabla} A_0 \right)^2 = -\frac{1}{2} q^2 A_0,
\end{aligned}
\tag{1.104}
$$

where we have left out also the decoupled purely spatial term. Identifying the charge as $Q = g$, the temporal electromagnetic field as $A_0 = i\varphi$ and the temporal external field with the disorder field, which we are free to rescale so that $B_0 = \Gamma V/Q$, these terms exactly lead to the untilted and isotropic limit of the overall action of Eq. (1.60) before applying the replica trick to treat the disorder average. We may thus expect our theory to be subject to a custom set of Ward identities that ensure that the remaining gauge symmetry is preserved, and anticipate the non-renormalization of the couplings.

Indeed, explicit calculation of the fermion loop integral in the dimensional regularization scheme set out in Subsubsec. 1.3.4 shows that it is entirely regular, or subleading in the dimensional regulator. Thus none of the diagrams including it, whether they be vertex corrections or part of the self-energy, contribute to the renormalization group flow. Constructing the remaining diagrams then amounts to an exercise in finding all one-particle irreducible ways of connecting the appropriate number of vertices on a single continuous fermion line at a given order in the perturbation expansion. This is true for both self-energy type diagrams and vertex corrections. As such, it follows that any vertex diagram can be obtained straightforwardly by inserting the corresponding external vertex into an internal fermion line of the appropriate self-energy diagram. By the Green function relation

$$
\partial_{i\omega'} G_{0,\chi}'(i\omega - i\omega', \mathbf{q} - \mathbf{k}) = -G_{0,\chi}'(i\omega - i\omega', \mathbf{q} - \mathbf{k}) \, \hat{\lambda} \, G_{0,\chi}'(i\omega - i\omega', \mathbf{q} - \mathbf{k})
\tag{1.105}
$$

we see that such an operation corresponds to taking the derivative with respect to the external frequency in mathematical terms. This argument continues to hold good also when the inclusion of a tilt in the dispersion

necessitates the introduction of an additional parameter in the fermion Green function by means of the field transformation Eq. (1.55) as it implies the relation changes into Eq. (1.105), mirroring the emergence of the matrix factor $\hat{\lambda}$ in both the fermion-bilinear vertex functions. We thus have Ward identities relating self-energy and vertex class contributions,

$$\text{(1.106)}$$

where the shaded areas represent the sum of all 1PI subdiagrams that can be used to connect the external legs and the derivative is understood to be taken with respect to the external frequency and applying the product rule. Due to the relations Eq. (3.43) vertex corrections will be exactly cancelled by the counterterms for the fermion field and the field transformation parameter from the self-energy corrections. As predicted, this leads to non-renormalization of the couplings Γ and g.

2 Disordered tilted Weyl cones

Up to minor notational and cosmetic alterations, this chapter is an integral reproduction of: Tycho S. Sikkenk and Lars Fritz, *"Disorder in tilted Weyl semimetals from a renormalization group perspective"*, Phys. Rev. B **96**, 155121 (2017) [39]. For this work TSS performed all calculations, discussed the results and prepared the manuscript for publication.

2.1 Introduction

In condensed matter theory, the Dirac equation describes the behavior of low energy quasiparticles near the touching points of two degenerate bands in the three dimensional dispersion of a class of materials known as Dirac semimetals (DSMs). These Dirac nodes are topologically protected by time reversal and inversion symmetry and cannot be removed without opening a gap in the spectrum. In Weyl semimetals (WSMs), at least one of these symmetries is broken and the Dirac nodal points disassociate into two Weyl nodes that are separated in momentum space. There is a non-zero flux of Berry curvature between the nodes that enriches them with an opposite monopole charge, or chirality, by Gauss' law. Band structure calculations predicted WSMs in several material families [23, 40] and Weyl fermion states have been discovered experimentally in materials such as TaAs, NbAs, TaP and NbP [12–15, 24, 41, 42]. Because of the unique features of their nodes, WSMs can exhibit a range of fascinating properties not observed in graphene, DSMs or other topological semimetallic systems. On their surface they harbor open Fermi surfaces connecting the node projections, implying novel contributions to various transport properties [18, 43]. Such surface arcs have also been observed in angle-resolved photoemission spectroscopy (ARPES) experiments on these systems.

The topological properties of these systems also lead to a remarkable robustness against weak perturbations, including disorder from dilute impurities [44, 45], since the Weyl nodes can only be annihilated by joining pairs of

opposite chirality [16]. This has important consequences for the properties under disorder, most notably of which is Anderson localization [28, 46]. For three dimensional metals it is well established that generically a mobility edge separating localized states from extended states develops as a function of disorder. The associated phase transition connects the diffusive metal (DM) with states above the mobility edge to the Anderson insulator on the other side. In Weyl systems the situation can be different in two ways: (i) A single Weyl node, very similarly to the surface Dirac fermion of a three dimensional strong topological insulator, cannot be localized by disorder because no backscattering can occur [47]. In reality, however, every Weyl node in a Weyl semimetal must be accompanied by its chiral partner, which then allows for backscattering through processes connecting the two cones. If the disorder is sufficiently long-range backscattering can be suppressed by the distance between the nodes in reciprocal space [25]. Indeed, intercone scattering has typically been found to have a much smaller amplitude than intracone scattering in realistic samples [48]. In the following we concentrate on a single Weyl node, assuming intercone processes are negligible compared to scattering within the cone. (ii) For a single Weyl node it was pointed out that there can be an additional phase at weak disorder that is semimetallic (SM) [26, 29, 30, 45, 49–51]. This point of view is currently challenged by numerical simulations which indicate the presence of rare regions [31]. However, for intermediate energy scales the critical point between the semimetal and diffusive metal should still control the physics, which is the point of view taken in this paper.

More recently, it was appreciated that Weyl cones in condensed matter systems, in contrast to fundamental Weyl fermions, do not have to be perfectly isotropic. The Femi velocity may take unequal values in different directions. Such anisotropy is common in Weyl semimetals and has significant consequences for various observable quantities [52, 53]. Alternatively, the Weyl spectrum may continuously be tilted away from its upright position. Recently, it was first predicted [7, 54] and later experimentally confirmed [14, 55–58] that the conical dispersion can even be tilted over. These systems, commonly referred to as type-II Weyl semimetals, develop a Fermi surface in which electron and hole pockets coexist with the Weyl touching points. This leaves clear signatures in their thermodynamic and transport properties, e.g. magnetic breakdown at nodal energy, unusual magneto-respsonse and the emergence of an intrinsic anomalous Hall effect [58–60]. Since nodal

quasiparticles can scatter resonantly to electron or hole surfaces, inclusion of disorder leads to considerably more complicated situations.

In contrast, subcritical tilts qualitatively preserve the structure of the pointlike Fermi surface. Nevertheless, they can have a definite influence on the transport properties of type-I Weyl cones. For instance, the conductance and Fano factor show strongly anisotropic responses upon increasing tilt [53]. Tilted Weyl cones support an increased amount of states at energies away from the nodal point and so enhance the effects of level broadening under disorder.

In this paper we investigate the interplay of finite subcritical tilts and potential disorder within the framework of the renormalization group. Our findings confirm earlier conclusions based on numerical methods and self-consistent Born approximation (SCBA) analysis [27], and additionally provide new analytic insights to describe disordered tilted Weyl cones.

The remainder of this chapter is organized as follows: Sec. 3.2 introduces the model. In Sec. 2.3 we study this model using an RG approach and discuss the resulting flow. Our main results consist of a set of analytical equations describing the scaling of the density of states when taking disorder effects into account. We show also that finite tilts lower the disorder strength of the SM-DM phase transition. Disorder generically renders the system anisotropic and furthermore increases the observable tilt, thereby enhancing the density of states. We finish with a conclusion in Sec. 3.6.

2.2 Model Setting

The starting point of our investigations is given by a single tilted Weyl cone described by the Bloch Hamiltonian

$$\mathcal{H}_{0,\chi}(\mathbf{q}) = v\,(t\,\sigma_0\,\mathbf{d} + \chi\,\boldsymbol{\sigma})\cdot\mathbf{q} \qquad (2.1)$$

where σ_0 is the identity matrix and $\{\sigma_x, \sigma_y, \sigma_z\}$ are the standard Pauli matrices. The Fermi velocity is given by v, while t denotes the strength of a tilt along the direction of unit vector $\mathbf{d}$, ($|\mathbf{d}| = 1$). The chirality of the cone is set by $\chi = \pm 1$. The eigenspectrum of Eq. (3.1) reads

$$E_{0,s}(\mathbf{q};t) = v\,(t\,\mathbf{d}\cdot\mathbf{q} + s\,k) = v\left(tq_\parallel + s\sqrt{q_\parallel^2 + q_\perp^2}\right)\,, \qquad (2.2)$$

where $s = \pm 1$ distinguishes electron and hole bands. We furthermore introduce a momentum parametrization where $q_\parallel$ is oriented in the direction of $\mathbf{d}$ while $q_\perp$ is a radial coordinate in the perpendicular plane. Upon increasing t the band structure progressively tilts over until the cone acquires one dispersionless direction at $t = 1$ thereby effectively becoming metallic (in principle higher order in momentum terms have to be included to stabilize the theory). Concentrating on values $0 < t < 1$ the density of states (DoS) behaves according to

$$\rho_{0,\chi}(\omega; t) = \frac{\omega^2}{2\pi^2 v^3 (1 - t^2)^2} \tag{2.3}$$

which becomes singular for $t \to 1$, consistent with the system going into the metallic phase.

We consider quenched scalar chemical potential disorder obeying a Gaussian white-noise distribution with zero mean [25, 35, 61],

$$\langle V(\mathbf{x}) \rangle = 0 , \qquad \langle V(\mathbf{x}) V(\mathbf{x}') \rangle = \Gamma^2 \, \delta^3(\mathbf{x} - \mathbf{x}') . \tag{2.4}$$

We are interested in average properties of the disordered system. Therefore, we promote the disorder potential to a field that is integrated over corresponding to an averaged partition function

$$Z^{(\chi)} = \int \mathcal{D}\psi^{(\chi)} \, \mathcal{D}V \, \exp\left\{ -S[\psi^{(\chi)}, V] \right\} , \tag{2.5}$$

$$S = S_0 + S_V + S_{\mathrm{dis},\Gamma} + S_{\mathrm{dis},\bar{\Gamma}} . \tag{2.6}$$

We have also rescaled V by Γ in both the disorder coupling term and the Gaussian weight introduced during the averaging procedure to obtain the expressions

$$S_V = \frac{1}{2} \int_{\mathbf{x}} V^2(\mathbf{x}) , \tag{2.7}$$

$$S_{\mathrm{dis},\Gamma} = \Gamma \int_{\mathbf{x}} \mathrm{d}\tau \, V(\mathbf{x}) \left(\psi^{(\chi),\dagger} \sigma_0 \psi^{(\chi)} \right) . \tag{2.8}$$

Philosophically, our procedure is equivalent to replicating the system and integrating out disorder, which leads to a retarded interaction in replica space. In contrast, we integrate out disorder only at every order in perturbation theory instead of exactly which provides us with technical advantages.

The combination of tilt and disorder (Eq. (2.6), Eq. (2.7), and Eq. (2.8)) is not closed under one-loop RG transformation. The self-energy generates a marginal term $\sim i\omega\,\chi\,\mathbf{d}\cdot\boldsymbol{\sigma}$ that is not present in the original action and should therefore be added by hand. We stress that this term is manifestly unphysical and cannot appear in a Hamiltonian due to its association with frequency $i\omega$. Rather, it is connected to the quasiparticle weight attributed to the exitations of the system. After Fourier transformation we obtain the adapted tree level Weyl fermion action

$$S_0 = \int_{\mathbf{x},\tau} \psi^{(\chi),\dagger}\left[(\sigma_0 - \chi\lambda\,\mathbf{d}\cdot\boldsymbol{\sigma})\,\partial_\tau + iv(t\,\sigma_0\,\mathbf{d} + \chi\boldsymbol{\sigma})\cdot\boldsymbol{\nabla}\right]\psi^{(\chi)}. \qquad (2.9)$$

Further analysis shows that there is also an additional vertex that is generated under the renormalization group transformation. As a result we add a second type of disorder vertex:

$$S_{\mathrm{dis},\bar{\Gamma}} = \bar{\Gamma}\int_{\mathbf{x},\tau} V(\mathbf{x})\left(\psi^{(\chi),\dagger}(-\chi\mathbf{d}\cdot\boldsymbol{\sigma})\psi^{(\chi)}\right) , \qquad (2.10)$$

which obeys the same distribution function as the original vertex. The altered free fermion Green function $G_{0,\chi}(i\omega,\mathbf{q})^{-1} = (i\omega - vt\,\mathbf{d}\cdot\mathbf{q})\sigma_0 - \chi(v\,\mathbf{q} + i\omega\lambda\,\mathbf{d})\cdot\boldsymbol{\sigma}$ that results from Eq. (2.9) has excitations at modified energy-momentum pairs. The poles of the inverse propagator, determined from $\det[G_{0,\chi}] = 0$, yield the dispersion

$$E_{0,s}(\mathbf{q};t,\lambda) = \frac{v}{1-\lambda^2}\left[(t+\lambda)q_\parallel + s\sqrt{q_\parallel^2(1+t\lambda)^2 + q_\perp^2(1-\lambda^2)}\right]. \quad (2.11)$$

We plot the excitation spectrum of Eq. (2.11) in Fig. 2.1 for some characteristic parameter values. Comparison with Eq. (3.2) teaches that the effect of λ on the dispersion is twofold:

(1). It introduces anisotropy into the system, inducing respective effective Fermi velocities

$$v_\parallel^{\mathrm{eff}} = v\,\frac{1+t\lambda}{1-\lambda^2} \qquad\qquad v_\perp^{\mathrm{eff}} = v\,\frac{1}{\sqrt{1-\lambda^2}} , \qquad (2.12)$$

parallel and perpendicular to the orientation of the tilt.

(2). It introduces an effective tilt,

$$t^{\text{eff}} = \frac{t + \lambda}{1 + t\lambda}. \tag{2.13}$$

The presence of finite anomalous tilt λ is also felt by other physical quantities such as the density of states,

$$\begin{aligned}
\rho_{0,\chi}(\omega; t, \lambda) &= -\frac{1}{\pi} \int_{\mathbf{q}} \text{Im Tr } G_{0,\chi}(\omega + i0^+, \mathbf{q}) \\
&= \frac{\omega^2 (1 + t\lambda)^2}{2\pi^2 v^3 (1 - t^2)^2} \sim \frac{\omega^2}{2\pi^2 v_{\parallel}^{\text{eff}} (v_{\perp}^{\text{eff}})^2 (1 - (t^{\text{eff}})^2)^2}.
\end{aligned} \tag{2.14}$$

Although increasing the anomalous tilt above unity implies tipping over the conical dispersion per Eq. (2.13), a vanishing quasiparticle weight ensures that Eq. (2.14) remains completely regular for all values of λ.

(a) $v = 1$, $t = \lambda = 0$.

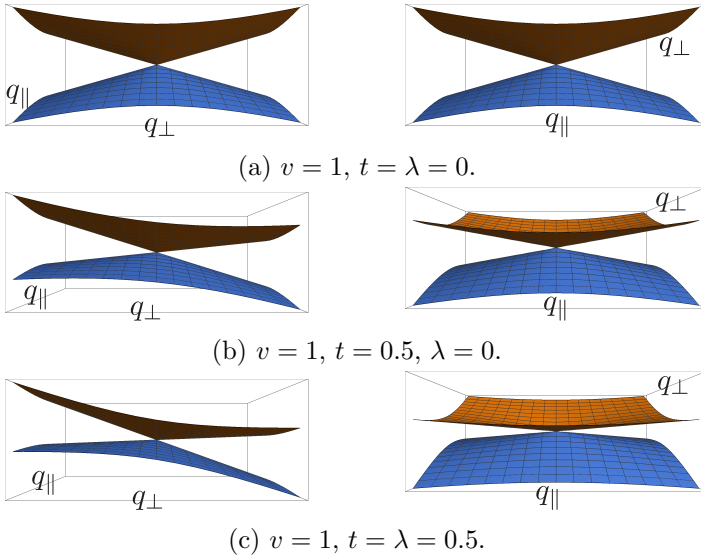(b) $v = 1$, $t = 0.5$, $\lambda = 0$.

(c) $v = 1$, $t = \lambda = 0.5$.

Figure 2.1: Modified Weyl cone dispersion $E_{0,s}(\mathbf{q}, t, \lambda)$ for (a) the untitled case, (b) ordinary tilt and (c) modified tilting.

2.3 Renormalization Group Analysis

The action Eq. (2.6) remains invariant under anisotropic space-time rescaling $\tau \to e^{zl}\tau$, $\mathbf{x} \to e^l\mathbf{x}$ for dimensionalities $[\psi] = [V] = d/2$ for the fermion and boson field, $[v] = z - 1$ for the Fermi velocity and $[\Gamma] = [\bar{\Gamma}] = z - d/2$ for the disorder couplings. The remaining parameters are scale-invariant irrespective of the number of spatial dimensions, $[t] = [\lambda] = 0$. The dimension number d and dynamical exponent z are model-dependent quantities. For three-dimensional Weyl semimetals ($d = 3$, $z = 1$) both disorder vertices are irrelevant at tree level. This opens up the possibility of the existence of a nontrivial quantum critical point separating a semimetallic weak disorder phase from the diffusive metal phase, as was extensively discussed in the untilted case [29, 30, 49, 50].

We now analyze the flow of the parameters by means of a one-loop expansion in both disorder couplings (note that within our scheme we treat λ non-perturbatively). Contributing diagrams are listed in Figs. 3.7)-2.3, where dotted vertices denote factors $\sim \Gamma$ deriving from Eq. (2.8) and squared vertices indicate factors $\sim \bar{\Gamma}$ coming from Eq. (2.10). We calculate these by integrating out the Fourier modes within the shell $e^{-l}\Lambda < k_\perp < \Lambda$ and $-\infty < q_\parallel < \infty$ [35]. This cylindrical momentum-shell scheme is indicated by a prime $'$ on the relevant integrals. Here we restrict ourselves to leading order expressions.
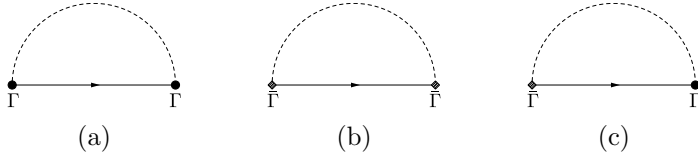
Figure 2.2: Diagrams contributing to the self-energy correction Σ to the modified naked Green function $G_{0,\chi}$.

The one-loop contributions to the self-energy are shown in Fig. 3.7. These diagrams are related by straightforward manipulation of external vertices. Introducing dimensionless couplings

$$\gamma^2 = \frac{\Gamma^2\Lambda}{4\pi v^2(1 - t^2)^{1/2}}, \qquad \bar{\gamma}^2 = \frac{\bar{\Gamma}^2\Lambda}{4\pi v^2(1 - t^2)^{1/2}}, \qquad (2.15)$$

the diagram of Fig. 2.2a yields

$$\text{Fig. 2.2a} = \Gamma^2 \int_{\mathbf{q}}^{'} G_{0,\chi}(i\omega, \mathbf{q})$$

$$\simeq -i\omega\,\gamma^2 \left(\frac{1+t\lambda}{1-t^2}\right)(\sigma_0 - t\,\chi\,\mathbf{d}\cdot\boldsymbol{\sigma})\,l. \tag{2.16}$$

Since $(-\chi\mathbf{d}\cdot\boldsymbol{\sigma})^2 = \sigma_0$ the diagram in Fig. 2.2b differs only by a change in coupling constant,

$$\text{Fig. 2.2b} = \left(\frac{\bar{\Gamma}}{\Gamma}\right)^2 (-\chi\mathbf{d}\cdot\boldsymbol{\sigma})\,[\text{Fig. 2.2a }]\,(-\chi\mathbf{d}\cdot\boldsymbol{\sigma})$$

$$\simeq -i\omega\,\bar{\gamma}^2 \left(\frac{1+t\lambda}{1-t^2}\right)(\sigma_0 - t\,\chi\,\mathbf{d}\cdot\boldsymbol{\sigma})\,l. \tag{2.17}$$

The diagram in Fig. 2.2c has a modified matrix structure,

$$\text{Fig. 2.2c} = 2\left(\frac{\bar{\Gamma}}{\Gamma}\right)(-\chi\mathbf{d}\cdot\boldsymbol{\sigma})\,[\text{Fig. 2.2a }]$$

$$\simeq -2i\omega\,\gamma\,\bar{\gamma}\left(\frac{1+t\lambda}{1-t^2}\right)(t\sigma_0 - \chi\,\mathbf{d}\cdot\boldsymbol{\sigma})\,l, \tag{2.18}$$

where we have also taken into account a symmetry factor of two that stems from the freedom to interchange the order of the vertex types. The dressed fermion propagator is then determined from the Dyson equation,

$$G_\chi(i\omega, \mathbf{q})^{-1} = G_{0,\chi}(i\omega, \mathbf{q})^{-1} - \Sigma(i\omega, \mathbf{q})$$

$$= \left[i\omega\left(1 + \frac{1+t\lambda}{1-t^2}\left((\gamma^2 + \bar{\gamma}^2) + 2t\gamma\bar{\gamma}\right)l\right) + vt\,\mathbf{d}\cdot\mathbf{q}\right]\sigma_0$$

$$+ \chi\boldsymbol{\sigma}\cdot\left[v\mathbf{q} - i\omega\mathbf{d}\left(\lambda + \frac{1+t\lambda}{1-t^2}\left(t(\gamma^2 + \bar{\gamma}^2) + 2\gamma\bar{\gamma}\right)l\right)\right]. \tag{2.19}$$

We similarly calculate the renormalization of the disorder couplings. At one loop order there are two contributing groups of diagrams, each of which has three representatives that are related by manipulation of external ver-
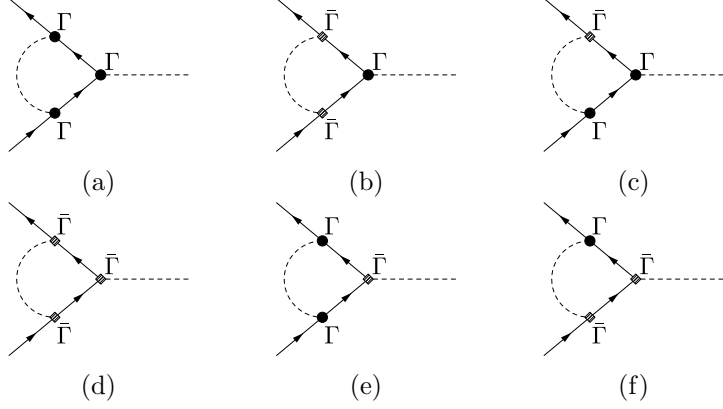
Figure 2.3: Vertex corrections to disorder couplings $\Gamma, \bar{\Gamma}$.

tices. For the first group, Figs. 2.3a-2.3c, we have

$$
\begin{aligned}
\text{Fig. 2.3a} &= \Gamma^3 \int_{\mathbf{q}}' G_{0,\chi}(0, \mathbf{q})^2 \\
&\simeq \Gamma \gamma^2 \left(\frac{1}{1 - t^2} \right) (\sigma_0 - t \chi \, \mathbf{d} \cdot \boldsymbol{\sigma}) \, l,
\end{aligned}
\tag{2.20}
$$

and

$$
\begin{aligned}
\text{Fig. 2.3b} &= \left(\frac{\bar{\Gamma}}{\Gamma} \right)^2 (-\chi \mathbf{d} \cdot \boldsymbol{\sigma}) \, [\text{Fig. 2.3a}] \, (-\chi \mathbf{d} \cdot \boldsymbol{\sigma}) \\
&\simeq \Gamma \bar{\gamma}^2 \left(\frac{1}{1 - t^2} \right) (\sigma_0 - t \chi \, \mathbf{d} \cdot \boldsymbol{\sigma}) \, l,
\end{aligned}
\tag{2.21}
$$

and

$$
\begin{aligned}
\text{Fig. 2.3c} &= 2 \left(\frac{\bar{\Gamma}}{\Gamma} \right) (-\chi \mathbf{d} \cdot \boldsymbol{\sigma}) \, [\text{Fig. 2.3a}] \\
&\simeq 2\Gamma \gamma \bar{\gamma} \left(\frac{1}{1 - t^2} \right) (t \, \sigma_0 - \chi \mathbf{d} \cdot \boldsymbol{\sigma}) \, l,
\end{aligned}
\tag{2.22}
$$

where we have again accounted for a symmetry factor of two for the last

diagram. The diagrams of the second group, 2.3d-2.3f, are given by

$$\text{Fig. 2.3d} = \bar{\Gamma}^3 \int_{\mathbf{q}}' (-\chi \mathbf{d} \cdot \boldsymbol{\sigma}) \left(G_{0,\chi}(0, \mathbf{q})(-\chi \mathbf{d} \cdot \boldsymbol{\sigma}) \right)^2$$

$$\simeq \bar{\Gamma} \bar{\gamma}^2 \left(\frac{t}{1 - t^2} \right) (\sigma_0 - t \chi \, \mathbf{d} \cdot \boldsymbol{\sigma}) \, l, \qquad (2.23)$$

and

$$\text{Fig. 2.3e} = \left(\frac{\Gamma}{\bar{\Gamma}} \right)^2 (-\chi \mathbf{d} \cdot \boldsymbol{\sigma}) \, [\text{Fig.(2.3d)}] \, (-\chi \mathbf{d} \cdot \boldsymbol{\sigma})$$

$$\simeq \bar{\Gamma} \gamma^2 \left(\frac{t}{1 - t^2} \right) (\sigma_0 - t \chi \, \mathbf{d} \cdot \boldsymbol{\sigma}) \, l, \qquad (2.24)$$

and

$$\text{Fig. 2.3f} = 2 \left(\frac{\Gamma}{\bar{\Gamma}} \right) (-\chi \mathbf{d} \cdot \boldsymbol{\sigma}) \, [\text{Fig. 2.3d}]$$

$$\simeq 2 \bar{\Gamma} \gamma \bar{\gamma} \left(\frac{t}{1 - t^2} \right) (t \, \sigma_0 - \chi \mathbf{d} \cdot \boldsymbol{\sigma}) \, l. \qquad (2.25)$$

With point like disorder, Eq. (2.4), the self-energy is independent of external momentum, meaning there is no direct renormalization of the Fermi velocity; it is just given by the inverse fermion field rescaling [61, 62]. The flow of the dimensionless disorder couplings is due to vertex corrections only. Including the bare scaling dimensions of the parameters we find leading-order β-functions

$$\beta_v = -\frac{1 + t\lambda}{1 - t^2} \left((\gamma^2 + \bar{\gamma}^2) + 2t\gamma\bar{\gamma} \right) v, \qquad (2.26)$$

$$\beta_\gamma = -\frac{\gamma}{2} + \frac{\gamma + t\bar{\gamma}}{1 - t^2} \left((\gamma^2 + \bar{\gamma}^2) + 2t\gamma\bar{\gamma} \right), \qquad (2.27)$$

$$\beta_{\bar{\gamma}} = -\frac{\bar{\gamma}}{2} + \frac{\gamma + t\bar{\gamma}}{1 - t^2} \left(t(\gamma^2 + \bar{\gamma}^2) + 2\gamma\bar{\gamma} \right), \qquad (2.28)$$

$$\beta_\lambda = \frac{1 + t\lambda}{1 - t^2} \left((t - \lambda)(\gamma^2 + \bar{\gamma}^2) + 2(1 - t\lambda)\gamma\bar{\gamma} \right), \qquad (2.29)$$

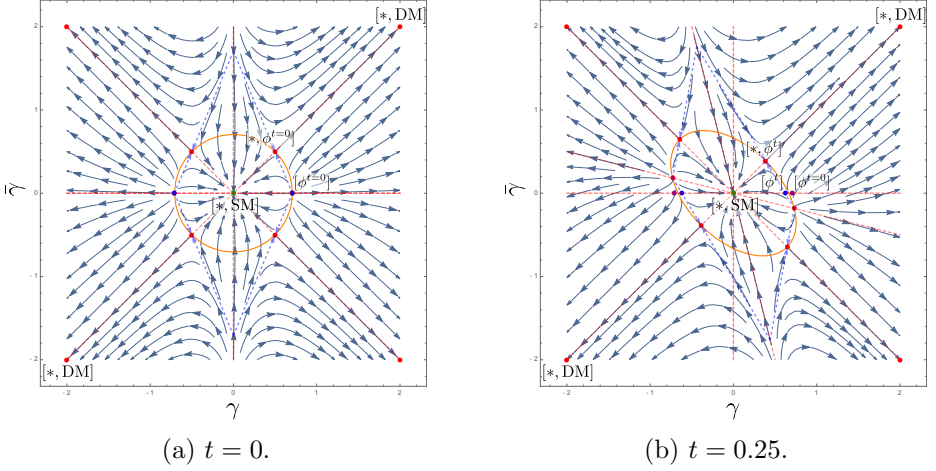where $\beta_{y_i} = \mathrm{d}y_i/\mathrm{d}l$ with $y_i = v, \gamma, \bar{\gamma}, \lambda$.

Figure 2.4: Flow for disorder couplings $\gamma, \bar{\gamma}$ and SCBA elliptic critcal disorder line, in orange (see Appendix 2.5) in (a) the untilted case, $t = 0$ and (b) the tilted case, $t = 0.25$. Red dots: disorder fixed points. Blue dots: phase transition points. Purple dot: untilted phase transition fixed point $(\gamma, \bar{\gamma})_{[\phi^{t=0}]} = (1/\sqrt{2}, 0)$.

2.3.1 Discussion of the RG equations

Under rescaling the model's parameters will flow away from their initial values, which are indicated here by subscript 0. Note that the starting values of the generated parameters are $\lambda_0 = \bar{\gamma}_0 = 0$. There are multiple parameter combinations for which β-functions (2.26)-(2.29) vanish simultaneously and the flow terminates. These fixed points are indicated by subscript asterisk $*$. A first observation is that the tilt parameter t is unaffected by the flow meaning there is no renormalization of the tilt within our renormalization scheme. As a consequence, the equations (2.27)-(2.28) for the dimensionless couplings γ and $\bar{\gamma}$ form a closed subset, producing a purely two-dimensional flow that is shown in Fig. 2.4.

Disorder flow: In general, there are three distinct fixed points that can be reached when initiating the flow at $\bar{\gamma}_0 = 0$. First of all, there is the attractive weak-coupling fixed point $(\gamma, \bar{\gamma})_{[*,\mathrm{SM}]} = (0, 0)$ which is associated with semimetallic behavior, called SM. Completely oppositely sit the attractive symmetry-related strong-disorder fixed points $(\gamma, \bar{\gamma})_{[*,\mathrm{DM}]} = \pm(\infty, \infty)$,

where the disorder strengths diverge. More interestingly, there are also the symmetry-related intermediate coupling fixed points

$$(\gamma, \bar{\gamma})_{[*,\phi^t]} = \pm \frac{1}{2} \left(\sqrt{\frac{1-t}{1+t}}, \sqrt{\frac{1-t}{1+t}} \right), \qquad (2.30)$$

that are attractive in two out of four directions and repulsive in the others. These fixed points will move towards the origin on the line $\gamma = \bar{\gamma}$ as t is increased, eventually merging with the weak-disorder fixed point $[*, \mathrm{SM}]$ for $t = 1$. The flow of the conventional untilted case $t = 0$ is presented in Fig. 2.4a. The disorder β-functions reduce to $\beta_\gamma = \gamma(\gamma^2 + \bar{\gamma}^2) - \gamma/2$ and $\beta_{\bar{\gamma}} = 2\bar{\gamma}\gamma^2 - \bar{\gamma}/2$, meaning $\bar{\gamma}$ is never generated and the flow remains effectively one-dimensional if the flow is initiated from $\bar{\gamma}_0$. This means that the intermediate fixed point $[*, \phi^{t=0}]$ is never accessed in the untilted model. It however allows for an unstable fixed point at $(\gamma, \bar{\gamma})_{[\phi^{t=0}]} = (0, 1/\sqrt{2})$ at which a transition from the weak-disorder into the strong-disorder regime occurs [25, 61, 62]. For finite tilts $t > 0$, the flow in Fig. 2.4b is fundamentally different. It holds on the horizontal axis $\bar{\gamma} = 0$ that $\beta_{\bar{\gamma}} = t\gamma^3/(1-t^2)$. Some $\bar{\gamma}$ is spontaneously generated in any disordered tilted Weyl system, which destabalizes the untilted fixed point. In return, the intermediate fixed point $[*, \phi^t]$ in Eq. (2.30) is now accesible to flow. It is reached only exactly from the phase transition point $[\phi^t]$ at $(\gamma, \bar{\gamma})_{[\phi^t]} = (\gamma_{[\phi^t]}, 0)$. We stress that $[\phi^t]$ is not an fixed point of the theory for finite tilts, but merely the point for $\bar{\gamma} = 0$ where the flow changes end point. To the left of $[\phi^t]$ on the horizontal axis the flow is towards weak disorder, whereas flow emanating form the right is directed towards strong disorder. Comparing Fig. 2.4a and Fig. 2.4b supports the observation [27] that including a finite tilt reduces the phase transition disorder strength, $\gamma_{[\phi^t]} \leq \gamma_{[\phi^{t=0}]}$. We substantiate this conclusion in Fig. 2.5, which directly graphs the dependency of the phase transition disorder strength on the tilt. Note that we have here used Eq. (2.15) to convert back to the original disorder strength Γ. Fig. 2.5 also contains a line which is obtained from a fully analytical solution of the self-consistent Born approximation (SCBA) which is presented in Appendix 2.5 and is consistent with an earlier analysis [27].

Concentrating on flow emanating from $\bar{\gamma}_0 = 0$, the asymptotic relation of the disorder couplings is surmised by $\bar{\gamma}_* = \gamma_*$ regardless of the side of the
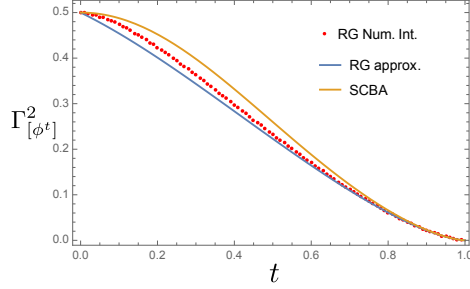
Figure 2.5: Dependence of the phase transition disorder strength $\Gamma_{[\phi]}$ on the ordinary tilt t. The SCBA (in orange, see Appendix 2.5) consistently overestimates the disorder required for the WSM-DM transition, whereas the boundary of the approximate weak-disorder parallelogram (in blue) leads to a lower estimate.

transition we study. We can then investigate the terminal behavior of the other parameters by restricting to the line $\bar{\gamma} = \gamma$.
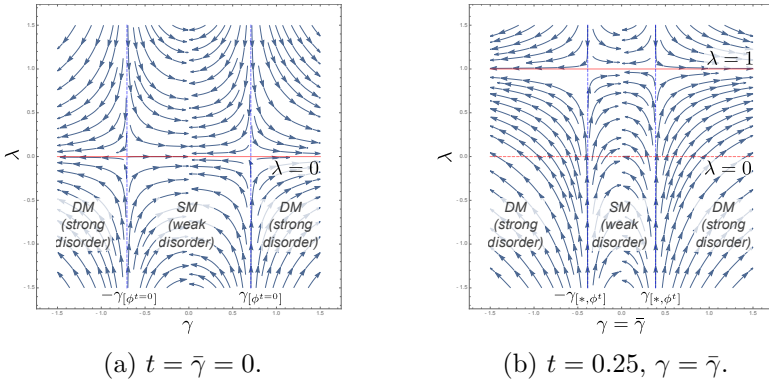
(a) $t = \bar{\gamma} = 0$.

(b) $t = 0.25$, $\gamma = \bar{\gamma}$.

Figure 2.6: Streamplot of anomalous tilting versus disorder for the appropriate terminal relations of γ and $\bar{\gamma}$. The flow predicts that λ will find a terminal value $0 \leq \lambda_* \leq 1$.

Anomalous tilt flow: Insertion of the terminal relation $\bar{\gamma} = \gamma$ into Eq. (2.29) yields the simplified λ-flow equation $\beta_\lambda = 2\gamma^2(1-\lambda)(1+t\lambda)/(1-t)$ valid on this line. Depending on the original tilt there are now two distinct scenarios that can be realized in a disordered system, also summarized in Fig. 2.6:

(1). for $t = 0$ we have that $\beta_\lambda = -2\lambda\gamma^2$, so that initial value $\lambda_0 = 0$ means that λ will never be generated.

(2). for $t > 0$ the anomalous tilt increases from $\lambda_0 = 0$ until reaching a fixed point with $0 < \lambda_{[*,\mathrm{SM}]} < 1$ inside the weak-disorder region and $\lambda_{[*,\mathrm{DM}]} = 1$ outside of it.

In general the final anomalous tilt λ_* after following the flow is a monotonically increasing function both of tilt t and disorder strength γ_0. λ will spontaneously acquire a finite value for any tilt $0 < t < 1$, even within the weak-disorder region. By Eq. (2.13) it follows that disorder *indirectly* increases the observable tilt in the system that is reached after concluding the disorder flow, although a final value $t_*^{\mathrm{eff}} = 1$ is never reached. This restricted growing behavior is depicted in Fig. 2.7. Earlier results [27] based on a more limited SCBA are qualitatively the same, but fail to pick up on the noticeable uptick in $t_{[*,\mathrm{SM}]}^{\mathrm{eff}}$ close to phase transition disorder strength. On the level of observables like the renormalized DoS, the transition from type-I to type-II Weyl cone is concealed by the disorder-induced WSM-DM transition.
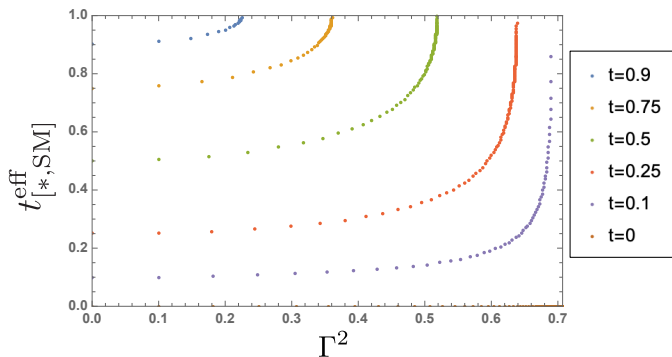
Figure 2.7: Terminal observable tilt at the weak disorder fixed point $t_{[*,\mathrm{SM}]}^{\mathrm{eff}}$ reached as a function of disorder strength Γ for selected value of original tilt t.

Velocity flow: Similarly, entering $\bar{\gamma} = \gamma$ into Eq. (2.26) yields the velocity flow equation $\beta_v = -2v\gamma^2(1+t\lambda)/(1-t)$ valid on this line. Note that, since we have verified that $0 < \lambda_* \leq 1$, it holds that β_v cannot be positive. Thus, v decreases until reaching a fixed point with a lower but finite Fermi velocity

$0 < v_{[*,\text{SM}]} < v_0$ inside the weak-disorder region and $v_{[*,\text{DM}]} = 0$ outside of it.

Note that the complete set of β-functions Eqs. (2.26)-(2.29) can be numerically integrated directly to study the behavior of the model under flow for a given set of initial parameter values. One might check that doing so confirms the analytical considerations above and substantiates the derived conclusions.

2.3.2 Interpretation and Discussion

The β-functions Eqs. (2.26)-(2.29) that result from RG treatment of disorder in the (anomalously) tilted Weyl cone produce a flow that can be divided into two qualitatively different regions separated by a quantum phase transition. In the weak-disorder region the flow of γ and $\bar{\gamma}$ is directed towards the origin. Under sufficient rescalings to smaller energy scales the system reaches the clean limit, albeit with lower but finite Fermi velocity $v_{[*,\text{SM}]}$ and at the price of acquiring a finite anomalous contribution $0 < \lambda_{[*,\text{SM}]} < 1$ to the tilt. It will thus preserve its semimetallic properties, such as a density of states that continues to vanish at the Weyl point and grow quadratically away from it along the lines of Eq. (2.14).

This behavior changes as the strength of the disorder in the model nears the phase transition point $[\phi^t]$. There, disorder flow is directed towards the intermediate fixed point $[*, \phi^t]$ of Eq. (2.30), at which the velocity and anomalous tilt have β-functions

$$\beta_v\big|_{[*,\phi^t]} = -\frac{v(1+t\lambda)}{2(1+t)}, \qquad \beta_\lambda\big|_{[*,\phi^t]} = \frac{(1-\lambda)(1+t\lambda)}{2(1+t)}$$

that show that their flow terminates for $v_{[*,\phi^t]} = 0$ and $\lambda_{[*,\phi^t]} = 1$. However, as mentioned before this does not imply that the system becomes metallic. The residual scaling of v and λ at the disorder fixed point $[*, \phi^t]$ is borne out also in the DoS. By virtue of its flowing parameters, at this point it obtains flow equation $\beta_\rho\big|_{[*,\phi^t]} = \rho$. Integration of this equation at cutoff scales that have become comparable to the chemical potential show that the disordered DoS will develop an additional inverse power of ω at criticality. Although

the system remains semimetallic, its DoS is enhanced to scale linearly,

$$\rho\big|_{[*,\phi t]}(\omega) \sim \frac{\omega}{(1-t^2)^2 v_0^3}.$$

(2.31)

It is worth noting that this yields critical exponents that are indistinguishable from those of the disordered untilted cone [30, 35, 62], but has substantially different prefactors.

On the other side of the transition sits a phase with entirely different characteristics. In the strong-disorder region both γ and $\bar{\gamma}$ undergo divergent flow signaling a breakdown of perturbation theory. Such problems can be circumvented by other methods such as the self-consistent Born approximation (SCBA) that we apply in Appendix 2.5: as an ansatz one supplements the Green function with some imaginary self-energy, which introduces a new length scale into the model with which to compare the cutoff. One then studies the conditions for which this self-energy is self-consistently allowed to take on non-zero values. Because finite imaginary self-energies must necessarily give a non-vanishing contribution to the density of states, i.e. $\rho(0) > 0$, this by definition can only take place in the strong-disorder region. The finite density of states observed even at the energy of the Weyl point shows that the strong-disorder phase is metallic in nature.

For generic three-dimensional models under disorder effects it is commonly accepted that there is a mobility edge separating localized states from extended states. The associated phase transition connects the diffusive metal with states above the mobility edge to the Anderson insulator on the other side [28, 46]. However, the model currently studied here contains only a single isolated Weyl cone and thus precludes the coherent backscattering thought to be a necessary precondition for Anderson localization. Such processes can be included by connecting two copies of the single Weyl fermion model with opposite chirality via off-diagonal intercone-scattering. The resulting Dirac-type model, with a four-dimensional matrix structure that allows for the spontaneous generation of yet more unexpected terms, will be the subject of a forthcoming paper. Another outstanding question relates to the stability of the disorder-induced WSM-DM transition to interactions. Coulomb-type interactions tend to renormalize the tilt towards zero and cause the model to flow towards the untilted limit at low energies [63], thus competing with the disorder-mediated effects studied here.

2.4 Conclusion

Within this paper we studied disorder in a model of a single tilted Weyl cone of type-I starting from a weak coupling perspective. We find a complicated multiparameter phase diagram which however still harbors a quantum critical point between a semimetallic and a diffusive metallic phase. We find that, like in the untilted case, as the system approaches critical disorder strength, the scaling of the density of states is enhanced to grow linearly with energy. We furthermore show within a renormalizaiton group approach that finite tilt quickens the disorder-induced semimetal-metal transition, see Fig. 2.5, and that disorder renormalizes the observable tilt to increase, see. Fig. 2.7, consistent with earlier work on this subject [27]. Future directions of research are to verify our findings numerically using the kernel polynomial method and also investigate the robustness under the addition of another cone. It is also interesting to contrast the increased tilt found in the disordered system from a recent finding in interacting Weyl systems where Coulomb interaction was shown to decrease tilt [63]. Therefore, one should expect an interesting interplay between the two.

2.5 Appendix: Self-Consistent Born Approximation (SCBA)

Besides the RG analysis of the main body we also studied the disorder-induced semimetal-diffusive metal (SM-DM) transition in tilted Weyl cones by means of a self-consistent Born approximation (SCBA). Implementing the ansatz $\Sigma^{\text{SCBA}} = i\alpha\,\sigma_0 - i\,\chi\,\beta\,\mathbf{d}\cdot\boldsymbol{\sigma}$ means that the self-energy acquires a finite imaginary part for $\alpha, \beta > 0$, which is directly related to the emergence of a finite DoS even at the nodal point across the transition [25, 27, 30]. We can then look for such solutions self-consistently and express the conditions for their emergence in terms of the critical disorder couplings.

Inspired by the result of the RG equations we calculate the self-energy with a more generic disorder term $\Upsilon_{\Gamma,\bar{\Gamma}} = (\Gamma\sigma_0 \mp \bar{\Gamma}\,\mathbf{d}\cdot\boldsymbol{\sigma})$ that is added to the non-interacting model corresponding to Eq. (3.1). This yields the self-consistency equation

$$
\begin{aligned}
\Sigma^{\text{SCBA}} &= \int_{\mathbf{q}}' \Upsilon_{\Gamma,\bar{\Gamma}} \left[G_{0,\chi}(0,\mathbf{q})^{-1} - \Sigma^{\text{SCBA}} \right]^{-1} \Upsilon_{\Gamma,\bar{\Gamma}} \\
&= i\left(\left((\gamma^2 + \bar{\gamma}^2) + 2t\gamma\bar{\gamma} \right)\sigma_0 - \chi\mathbf{d}\cdot\boldsymbol{\sigma}\left(t(\gamma^2 + \bar{\gamma}^2) + 2\gamma\bar{\gamma} \right) \right) \\
&\quad \times (1 - t^2)^{-1}\,(\alpha + t\beta)\,f(\alpha + t\beta),
\end{aligned}
$$

where f is a complicated function of $\alpha + t\beta$. Due to the ansatz matrix structure of the self-energy, this is solved only by a constant ratio

$$
\rho = \frac{\beta}{\alpha} = \frac{t(\gamma^2 + \bar{\gamma}^2) + 2\gamma\bar{\gamma}}{(\gamma^2 + \bar{\gamma}^2) + 2t\gamma\bar{\gamma}}. \tag{2.32}
$$

Defining $\tilde{\alpha}^2 = (1 + t\rho)^2\alpha^2$, we then find a scalar equation for this remaining unknown:

$$
\tilde{\alpha} = \tilde{\alpha}\,\Delta_{\Gamma,\bar{\Gamma}}f\left(\tilde{\alpha}\right), \tag{2.33}
$$

where $\Delta_{\Gamma,\bar{\Gamma}} = (1 + t\rho)/(1 - t^2)((\gamma^2 + \bar{\gamma}^2) + 2t\gamma\bar{\gamma})$ is a suitably defined composite coupling. We can now determine the qualitative solutions to the self-consistency equation for $\tilde{\alpha}$ by contrasting the LHS and RHS of Eq. (2.33), see Fig. 2.8. Indeed, we find that for $\Delta_{\Gamma,\bar{\Gamma}} \leq 1$ the equation is solved only by trivially setting $\tilde{\alpha} = 0$, whereas $\Delta_{\Gamma,\bar{\Gamma}} > 1$ opens up the possibility of a

finite self-energy. Thus, we find an exact critical disorder line in coupling space that is determined by the relation

$$(1 - t^2) = (1 + t^2)(\gamma^2 + \bar{\gamma}^2) + 4t\gamma\bar{\gamma} . \tag{2.34}$$

This equation describes an elliptic critical disorder line that coincides exactly with all the non-trivial disorder fixed points, see Fig. 2.4b, as long as we take into account a known factor of two difference between SCBA and renormalisation group results [27, 53]. From the same picture, we can deduce that SCBA analysis slightly overestimates the critical disorder strength γ_c^t, with the terminal direction of the flow switching only between the blue and yellow point on the positive branch of the $\bar{\gamma} = 0$ axis.

We extract the critical disorder strength as a function of tilt t at which the system transitions from semimetal to diffusive metal from the SCBA ellipse defined by Eq. (2.34). Setting $\bar{\gamma} = 0$ we find that it is given by

$$2(1 + t^2)(\gamma_\phi^t)^2 = (1 - t^2), \tag{2.35}$$

where again we have accounted for a factor of 2. This exact relation is to be compared with the results gathered from RG analysis, see Fig. 2.5. Scaling back to original coupling Γ, this graph reproduces the results from Ref.[27] up to normalization.
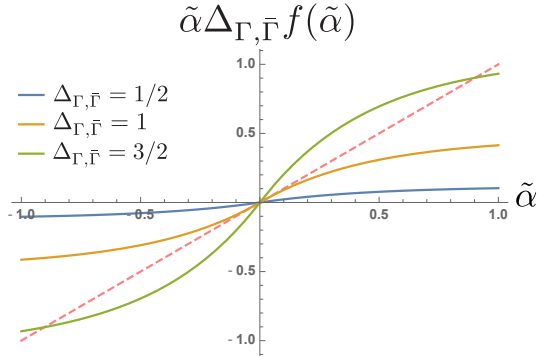

Figure 2.8: (a)-(c): Comparison of $\tilde{\alpha}$ and $\tilde{\alpha} \, \Delta_{\Gamma,\bar{\Gamma}} \, f(\tilde{\alpha})$ for the indicated composite-couplings Δ.

3 Disorder and interactions in anisotropic tilted Weyl cones

Up to minor notational and cosmetic alterations, this chapter is an integral reproduction of: Tycho S. Sikkenk and Lars Fritz, *"Interplay of disorder and interactions in a system of subcritically tilted and anisotropic three-dimensional Weyl fermions"*. Phys. Rev. B **100**, 085121 (2019) [64].

For this work TSS performed all calculations, discussed the results and prepared the manuscript for publication.

3.1 Introduction

In electronic systems with band touching points the effective low energy theory can often be expressed in terms of linearly dispersing Dirac fermions. Of these Dirac systems the two-dimensional material graphene, isolated only in 2004 [65], is the most prominent representative. In the three-dimensional Weyl subclass the massless Dirac fermions dissociate into pairs of Weyl fermions that can separate in momentum space [66]. Band structure calculations predict such excitations in several material families [23, 56], and they have been shown to exist in materials such as TaAs, NbAs, TaP and NbP [12–15, 24, 41, 42] in experiment.

Weyl fermions exhibit interesting physical properties, such as the chiral anomaly and surface Fermi arcs, that have put them into the focus of intense research interest [17, 18, 42, 67–70]. In the absence of perturbations, Weyl systems are semimetals with a Density of States (DoS) that vanishes at the Weyl point. The corresponding nodes in the spectrum are sources and sinks of Berry curvature, and their resultant opposite topological charges imply that no gap can be opened in the spectrum without merging chiral partner modes. This makes the semimetallic (SM) phase remarkably robust to weak perturbations.

Disorder constitues an irrelevant perturbation to the three-dimesional

Weyl semimetal in the renormalization group (RG) sense. Consequently, the system was subjected to perturbation theory based methods that showed that the SM phase prevails up to a critical disorder strength [25, 29, 71]. Beyond this critical strength it enters a diffusive metallic (DM) phase characterized by a finite Density of States at the Weyl point. This view is challenged by numerical results that call into question the existence of the SM phase on the basis of rare regions leading to an exponentially small but finite DoS at Fermi level [31]. More recent analytical works, however, insist on the stability of the SM phase and absence of these rare regions [72]. Irrespective of the final resolution of this matter for intermediate energy scales the critical point between SM and DM phases should still control the physics, validating perturbative approaches. Even at high degrees of disorder Anderson localization cannot occur in a model of a single Weyl cone due to the absence of available backscattering states. In realistic models comprising multiple pairs of chiral Weyl pairs backscattering processes connecting different cones are allowed, but they are supressed by the intercone distance in reciprocal space [25].

Furthermore, Coulomb interactions are a marginal perturbation in any number of dimensions. Due to the vanishing free Density of States at the Fermi level in Weyl semimetals they are left unscreened [73]. These long-ranged interactions decay quadratically in momentum space so that processes connecting well-separated Weyl nodes are surpressed. It is worth emphasizing that such interactions constitute but a particular version of quantum electrodynamics, whose central tennet is the preservation of the invariance under the $U(1)$ local gauge transformation. The coupling of the Weyl fermions with the photon mediating the Coulomb interactions should then be subject to Ward identities [1, 74].

In Weyl semimetal materials the Fermi velocity of the cone is much lower than the speed of light c. Consequently, Coulomb interactions are instantaneous on the time scale of the fermions and retardation effects are neglible [75]. Furthermore, unlike in particle physics, the effective Weyl fermions need not be Lorentz invariant. This allows for various distortions in the conical dispersion of condensed matter Weyl semimetals. Anisotropies are a common occurence in the Weyl spectrum and have several observable effects [53]. Tilts also appear frequently and have been predicted [53, 76, 77] and experimentally found [78] to produce clear signatures in various properties. In type-II Weyl cones the dispersion is tilted over, so that hole and particle

pockets emerge in the Fermi surface besides the Weyl nodes by which the DoS develops a finite value [7]. We here restrict to the subcritical tilts in type-I Weyl cones, which preserve the point-like nature of the Fermi surface. Within this model the effects of the tilt derive from increasing the number of states available at a given finite energy.

In this paper, we present a renormalization group analysis of the interplay of disorder and interactions at Fermi level in three-dimensional Weyl fermions with a tilted and anisotropic dispersion. Including both disorder and electromagnetic perturbations stabilizes the SM phase in untilted isotropic cones [61]. Whereas the degree of tilting is increased by disorder [39], Coulomb interaction tends to decrease it [63]. Coulomb interactions cause flow towards restoration of the isotropy of the Weyl dispersion, while disorder effects magnify the anisotropy between different momentum directions. The goal of this study is then to investigate the combined effect of these competing tendencies and the possible existence of new fixed points.

The two main results of this study are: (I) despite competing tendencies to lowest loop order there is no new fixed point and like in the untilted case the SM phase is stabilized by the interplay of disorder and Coulomb interaction. (II) Using a field transformation to capture all RG generated terms we find a Ward identity by which this result holds to *all* orders in perturbation theory.

The main body of the paper is organized as follows. Sec. 3.2 introduces the model and especially discusses the need for a field transformation to capture all terms generated under RG transformation. Sec. 3.3 presents the flow equations resulting from a lowest loop order expansion. Sec. 3.4 follows with a discussion of the flow equations. We first treat various limiting cases analytically in Subsecs. 3.4.1-3.4.5 before numerically considering the full RG flow of the general theory in Subsec. 3.4.6. In Sec. 3.5 we establish a Ward identity of the model and discuss its implications for calculations at any order in perturbation theory. We finish with a conclusion in Sec. 3.6.

3.2 Model Setting

In this section we present our model and set it up for RG treatment. While we have relegated the technical details of the diagrammatic calculations to

appendix 3.7, they eventually result in the set flow equations presented in Sec. 3.3.

As argued in the introduction, the separation of Weyl cones in momentum space both represses processes that merge nodes of opposite topological charge, without which a gap cannot open in the dispersion, and subdues intercone disorder scattering and Coulomb interactions. We thus reasonably start from the generalized Bloch Hamiltonian of a single isolated Weyl fermion in $d + 1$ dimensions,

$$\mathcal{H}_{0,\chi}(\mathbf{q}) = v \left[t \, q_\parallel \sigma_0 + \chi \left(q_\parallel \mathbf{d} + \eta \, \mathbf{q}_\perp \right) \cdot \boldsymbol{\sigma} \right], \tag{3.1}$$

where the dot product implies summation over d spatial dimensions. The Weyl matrices σ_μ are 2^{m-1} dimensional, where $m = \text{floor}\left[(d + 1)/2\right]$, and satisfy the anticommuting Clifford algebra $\{\sigma_\mu, \sigma_\nu\} = \delta_{\mu\nu}$ for $\mu, \nu = 0, 1, \ldots, d$. Here, σ_0 may be interpreted as the 2^{m-1} dimensional identity matrix. Note that in the case that $d = 3$ the Weyl matrices reduce to the commonly known Pauli matrices. We have furthermore introduced a momentum parametrization where component $q_\parallel = \mathbf{d} \cdot \mathbf{q}$ is oriented along the unit vector $\mathbf{d}$ while $\mathbf{q}_\perp = \mathbf{q} - q_\parallel \mathbf{d}$ is a radial projection onto the $(d - 1)$ dimensional perpendicular plane. The chirality of the Weyl node is determined by $\chi = \pm 1$. The Hamiltonian of Eq. (3.1) results in a dispersion given by

$$E_{0,s}(\mathbf{q}) = v \left(tq_\parallel + s\sqrt{q_\parallel^2 + \eta^2 q_\perp^2} \right), \tag{3.2}$$

where $s = \pm 1$ distinguishes the conduction and valence bands. The Fermi velocity is given by v, while η controls the possible development of anisotropy between the parallel and perpendicular momentum directions. The parameter t tilts the Weyl cone in the direction of $\mathbf{d}$. Increasing t causes the band structure to tilt over until the fermion becomes dispersionless as $t \to 1$. This breakdown of the SM phase is also apparent in the divergence at overtilting of the DoS

$$\rho_{0,\chi}(\omega) = -\frac{1}{\pi} \int_{\mathbf{q}} \text{Im Tr } G_{0,\chi}(\omega + i0^+, \mathbf{q}) \sim \frac{\omega^2}{v^3 \eta^2 (1 - t^2)^2}, \tag{3.3}$$

where we have used the propagator corresponding to the Weyl Hamiltonian of Eq. (3.1),

$$\begin{aligned} G_{0,\chi}^{-1} &= i\omega \, \sigma_0 - \mathcal{H}_{0,\chi} \\ &= (i\omega - vt \, q_\parallel)\sigma_0 - v\chi(q_\parallel \mathbf{d} + \eta\mathbf{q}_\perp) \cdot \boldsymbol{\sigma}. \end{aligned} \tag{3.4}$$

In the remainder of this work, we concentrate on type-I Weyl cones with subcritical tilts $0 \leq t < 1$.

We are interested in the behavior of Weyl fermions in a disordered background that is described by a quenched potential landscape $V(\mathbf{x})$ obeying a Gaussian white-noise distribution with

$$\langle V(\mathbf{x}) \rangle = 0, \qquad \langle V(\mathbf{x}) V(\mathbf{x}') \rangle \sim \delta(|\mathbf{x} - \mathbf{x}'|). \tag{3.5}$$

We average over the random potential using the replica trick, so preserving generic disorder properties [3, 79]. This entails taking many copies of the theory, promoting the various disorder distributions to a collective field V that is integrated over in the partition function with Gaussian weight

$$S_V = \frac{1}{2} \int_{\mathbf{q}} V_{\mathbf{q}} V_{-\mathbf{q}}, \tag{3.6}$$

and finally taking the number of replicas to zero in the limit. Suppressing the summed over replica indices, this results in a free fermion action

$$S_\psi = \int_{\omega,\mathbf{q}} \psi^\dagger_{\omega,\mathbf{q}} G^{-1}_{0,\chi} \psi_{\omega,\mathbf{q}}. \tag{3.7}$$

We couple the external disorder field to the density of the Weyl fermions according to

$$S_{\text{dis}} = \Gamma \int_{\mathbf{q},\mathbf{q}',\omega} V_{\mathbf{q}-\mathbf{q}'} \left(\psi^\dagger_{\mathbf{q},\omega} \, \sigma_0 \, \psi_{\mathbf{q}',\omega} \right). \tag{3.8}$$

Note that this approach is equivalent but technically differs from the more standard way of treating the disorder in which the field V is integrated out explicitly, resulting in a four-fermion interaction term.

The Weyl fermions are furthermore coupled amongst each other by means of long-range Coulomb interactions. This is represented as

$$S_{\text{Cou}} = ig \int_{\mathbf{q},\mathbf{q}',\omega,\omega'} \varphi_{\mathbf{q}-\mathbf{q}',\omega-\omega'} \left(\psi^\dagger_{\mathbf{q},\omega} \, \sigma_0 \, \psi_{\mathbf{q}',\omega'} \right), \tag{3.9}$$

where the fermions are interacting by means of a scalar gauge photon, whose free propagation is given by

$$S_\varphi = \frac{1}{2} \int_{\omega,\mathbf{q}} \varphi_{\omega,\mathbf{q}} D^{-1}_0 \varphi_{-\omega,-\mathbf{q}}. \tag{3.10}$$

In Weyl semimetals the Fermi velocity is typically much smaller than the speed of light, $v' \ll c$, so that retardation effects in the Coulomb interaction can be safely neglected [75]. As a consequence, the bare photon propagator is taken to be

$$D_0^{-1} = q^{d-1-\bar{\epsilon}} = \left(q_\parallel^2 + q_\perp^2 \right)^{(d-1-\bar{\epsilon})/2}, \tag{3.11}$$

where $\bar{\epsilon} \to 0$ is a dimensional regulator that is introduced for technical reasons.

In real materials the dispersion can feature many different pairs of Weyl cones at comparable energies [13, 23]. In the above we have implicitly neglected the disorder scattering between different cones as it is surpressed by their momentum space distance [25, 48]. The intercone Coulomb interaction, in three dimensions decaying as $\sim 1/q^2$, is similarly subdued by the cone separation and is thus also omitted [63].

As was noted previously, perturbing the bare system S_ψ by disorder action S_{dis} generates a new term $\sim t\,i\omega\,\mathbf{d}\cdot\boldsymbol{\sigma}$ in the self-energy contribution once a finite tilt $t > 0$ is included [39]. This was also observed recently in the context of two dimensional Dirac fermions perturbed by various types of disorder [80, 81]. In those works this issue was resolved by adding the term to the bare Green function by hand and treating it as a bona fide, stand-alone parameter of the theory. We here propose a different scheme to manage such terms, in which we absorb the anomalous contributions in a redefinition of the fermion field. This will have ramifications for both the bare parameters and the couplings of the theory we consider.

We transform the fermion field according to

$$\psi_{\omega,\mathbf{q}} = \hat{\lambda}^{1/2}\,\psi'_{\omega,\mathbf{q}}, \qquad\qquad \hat{\lambda} = \sigma_0 - \lambda\,\chi\,\mathbf{d}\cdot\boldsymbol{\sigma}. \tag{3.12}$$

This transformation matrix equals the identity at the beginning of our RG procedure and only perturbatively obtains a non-trivial structure. Under influence of this shift the free fermion action of Eq. (3.7) becomes

$$S'_\psi = \int_{\omega,\mathbf{q}} \psi'^\dagger_{\omega,\mathbf{q}} G'^{-1}_{0,\chi} \psi'_{\omega,\mathbf{q}} \tag{3.13}$$

with a modified (inverse) Green function

$$G_{0,\chi}'^{-1} = \hat{\lambda}^{1/2} G_{0,\chi}^{-1} \hat{\lambda}^{1/2} \tag{3.14}$$
$$= (i\omega\hat{\lambda} - v't'q_{\parallel})\sigma_0 - v'\chi \left(q_{\parallel}\mathbf{d} + \eta'\mathbf{q}_{\perp} \right) \cdot \boldsymbol{\sigma}.$$

This propagator has the same flavor as the original, with parameters that are related as

$$v' = v\,(1 - t\lambda), \quad \eta' = \eta\,\frac{\sqrt{1 - \lambda^2}}{1 - t\lambda}, \quad t' = \frac{t - \lambda}{1 - t\lambda}, \tag{3.15}$$

or alternatively,

$$v = v'\,\frac{1 + t'\lambda}{1 - \lambda^2}, \quad \eta = \eta'\,\frac{\sqrt{1 - \lambda^2}}{1 + t'\lambda}, \quad t = \frac{t' + \lambda}{1 + t'\lambda}. \tag{3.16}$$

Unlike in Eq. (3.4), however, in the transformed propagator Eq. (3.14) the frequency $i\omega$ is supplemented with the matrix structure of the transformation that can absorb the contributions deriving from the disorder-induced self-energy. Since $\det G_{0,\chi}' = \det G_{0,\chi}/\det \hat{\lambda}$, the poles of the Green function remain unchanged under transformation Eq. (3.12) and the energy spectrum remains given by Eq. (3.2). Rather, the newly generated parameter λ acts on the level of the quasiparticle weight attributed to the excitations of the system.

The field transformation also impacts the coupling terms of the action, Eqs. (3.8)-(3.9). They become

$$S'_{\text{dis}} = \int_{\omega,\mathbf{q},\mathbf{q}'} V_{\mathbf{q}-\mathbf{q}'} \psi'^{\dagger}_{\omega,\mathbf{q}} \left(\Gamma\,\hat{\lambda} \right) \psi'_{\omega,\mathbf{q}'}, \tag{3.17}$$

$$S'_{\text{Cou}} = \int_{\omega,\omega',\mathbf{q},\mathbf{q}'} \varphi_{\omega-\omega',\mathbf{q}-\mathbf{q}'} \psi'^{\dagger}_{\omega,\mathbf{q}} \left(ig\,\hat{\lambda} \right) \psi'_{\omega',\mathbf{q}'}. \tag{3.18}$$

As the above equations show, one of the merits of the transformation procedure Eq. (3.12) is that minimal coupling between frequency $i\omega$ on the one hand and gauge field φ and external field V on the other hand is respected by construction. The same parameter λ is now present not only in the Green function Eq. (3.14) but also in both interacting parts of the action. We will find that it will obtain identical renormalizations in each of these sections.

3.3 RG equations

We study the action

$$S'_0 = S'_\psi + S_V + S_\varphi, \qquad S'_{\text{int}} = S'_{\text{dis}} + S'_{\text{Cou}}, \tag{3.19}$$

in the framework of RG based on renormalized perturbation theory. Counterterms are introduced as $y_{i,0} = Z_{y_i} y_i(\mu)$, where $Z_{y_i} = 1 + \delta_{y_i}$. Under anisotropic space-time rescaling

$$\omega \to \mu^{+z}\omega, \qquad \mathbf{q} \to \mu^{+1}\mathbf{q}, \tag{3.20}$$

the parameters and fields change as $y_i(\mu) \to \mu^{+[y_i]} y_i(\mu)$, where $[y_i]$ denotes dimensionality. We determine the scaling dimensions of the fields from S'_0 to be $[\psi_{\omega,\mathbf{q}}] = -(d+2z)/2$ for the fermion field, $[V_{\mathbf{q}}] = -d/2$ for the disorder field, $[\varphi_{\omega,\mathbf{q}}] = -(2d+z-1-\bar\epsilon)/2$ for the photon field and $[v] = z-1$ for the Fermi velocity. The other parameters are scale-invariant, *i.e.*, $[t] = [\lambda] = [\eta] = 0$.

The disorder coupling has dimension $[\Gamma] = z - d/2$ meaning for a free Weyl theory ($z = 1$) it is marginal in $d = 2$ and irrelevant in $d = 3$. The Coulomb interaction mediated by the photons has scaling dimension $[g] = (z-1-\bar\epsilon)/2$, where $\bar\epsilon \to 0$ in the end. In that case Coulomb interactions are marginal irrespective of the number of spatial dimensions. In the following we perform a double ϵ-expansion around the marginal dimension, $d = 2$ and $\bar\epsilon = 0$ by working in $d = 2 + \epsilon$. We keep ϵ and $\bar\epsilon$ finite throughout the calculation and take $\epsilon \to 1$, corresponding to three dimensions, and $\bar\epsilon \to 0$ in the end. Such dimensional regularization is known to respect gauge invariance [1].

We perform a one loop expansion in Γ and Coulomb interaction strength g. Within our scheme the tilt t, anisotropy η and the generated parameter λ are treated non-perturbatively. This results in the set of diagrams presented in appendix 3.7. The required counterterms and derived flow equations are set out in appendix 3.8. In appendix 3.9 they are translated back to β functions of the original model parameters appearing in the dispersion by using Eq. (3.15).

We express the flow in terms of dimensionless couplings

$$\alpha = \frac{\Omega_d \, \mu^{\bar\epsilon}}{4(2\pi)^d \, v} \, g^2, \qquad \gamma^2 = \frac{\Omega_d \, \mu^{\epsilon}}{(2\pi)^d \, v^2} \, \Gamma^2, \tag{3.21}$$

with Ω_d the d-dimensional solid angle. The primary set of four coupled ultraviolet flow equations is then given by

$$\beta_t = t \left\{ \frac{1}{\eta\sqrt{1-t^2}}\gamma^2 - \alpha F_\parallel^\eta \right\}, \tag{3.22}$$

$$\beta_\eta = -\eta \left\{ \frac{t^2}{\eta(1-t^2)^{3/2}}\gamma^2 + \alpha \left(F_\parallel^\eta - F_\perp^\eta \right) \right\}, \tag{3.23}$$

$$\beta_\alpha = \alpha \left\{ -\bar{\epsilon} + \frac{1}{\eta\sqrt{1-t^2}}\gamma^2 - \alpha F_\parallel^\eta \right\}, \tag{3.24}$$

$$\beta_\gamma = \gamma \left\{ -\frac{\epsilon}{2} + \frac{1}{\eta\sqrt{1-t^2}}\gamma^2 - \alpha F_\parallel^\eta \right\}, \tag{3.25}$$

where $\beta_{y_i} = -\mathrm{d}y_i/\mathrm{d}\ln\mu$ for parameters y_i. We stress that the limits $\bar{\epsilon} \to 0$, $\epsilon \to 1$ should be taken in the end. We have furthermore defined two functions that depend solely on the anisotropy η,

$$F_\parallel^\eta = \frac{4\eta \left[\mathrm{EllipticE}(1-\eta^{-2}) - \mathrm{EllipticK}(1-\eta^{-2}) \right]}{\pi(1-\eta^2)}, \tag{3.26}$$

$$F_\perp^\eta = -\frac{4 \left[\mathrm{EllipticE}(1-\eta^2) - \mathrm{EllipticK}(1-\eta^2) \right]}{\pi(1-\eta^2)}. \tag{3.27}$$

When isotropy is restored, $\eta = 1$, these functions return $F_\parallel^{\eta=1} = F_\perp^{\eta=1} = 1$.

Apart from the coupled set Eqs. (3.22)-(3.25), the behavior of the remaining parameters obey

$$\beta_v = v \left\{ z - 1 - \frac{1}{\eta\sqrt{1-t^2}}\gamma^2 + \alpha F_\parallel^\eta \right\}, \tag{3.28}$$

$$\beta_\lambda = t\frac{1-\lambda^2}{\eta(1-t^2)^{3/2}}\gamma^2. \tag{3.29}$$

Note from the last equation that the spontaneous generation of a finite value transformation parameter λ is conditional on the simultaneous presence of non-zero tilt and disorder.

3.4 Discussion of the RG equations

The β functions in Eqs. (3.22)-(3.25) form a closed set that describes the scale dependence of the general theory of a tilted and anisotropic Weyl semimetal

under influence of disorder and interactions. In the following we indicate the initial parameters by a subscript zero in keeping with previously used terminology [39]. We stress that the field transformation Eq. (3.12) is necessary only to account for perturbatively generated terms, so that we strictly have $\lambda_0 = 0$ initially.

There are multiple parameter combinations for which the primary β functions vanish simultaneously. These fixed points are indicated by subscript asterisk. The corresponding values for the secondary parameters v and λ can then be obtained from their flow equations by substitution. The fixed points are characterized by a set of exponents that control the critical physics in their vicinity. The correlation length ξ scales as $\xi \sim \delta^{-\nu}$, where δ corresponds to a linearization of the most relevant operator around the fixed point and ν is the correlation length exponent (CLE). For finite $\nu > 0$ the correlation length diverges when $\delta \to 0$ on approach to the fixed point, a critical indication the system is undergoing a phase transition. Technically, ν is the inverse of the most repulsive eigenvalue of the linearized RG transformation matrix $M_{ij} = \partial\beta_{y_i}/\partial y_j|_*$ at the fixed point. Since the parameter transformations Eq. (3.16) can become singular the CLE is best derived from the flow equations of the parameters presented in appendix 3.8. Another exponent is straightforwardly found from Eq. (3.135). At a fixed point v is scale-invariant, requiring a dynamical scaling exponent (DSE)

$$z = 1 + \left[\frac{1}{\eta\sqrt{1-t^2}}\gamma^2 - \alpha F_{\parallel}^{\eta} \right]_* . \tag{3.30}$$

This is highly significant as the DoS of the three-dimensional Weyl cone model scales with the energy away form the band touching point as

$$\rho(\omega) \sim |\omega|^{(3-z)/z} \tag{3.31}$$

in the SM phase, including close to the phase transition into the DM [82]. Both disorder and Coulomb interactions modify the DSE away from unity and could then lead to perturbative corrections to the square scaling of the free DoS in Eq. (3.3).

In order to interpret the flow produced by the RG equations it is instructive to first consider some of the limiting cases.

3.4.1 Untilted, disordered case

Firstly we investigate the untilted non-interacting model as in Refs. [25, 62], corresponding to initial values $\lambda_0 = t_0 = \alpha_0 = 0$. All the primary flow equations reduce to zero, except for the disorder β function

$$\beta_\gamma = \gamma \left\{ -\frac{\epsilon}{2} + \frac{1}{\eta_0} \gamma^2 \right\}. \tag{3.32}$$

Note that the presence of fermion anisotropy η is trivial only affecting the flow as a numerical factor and therefore omitted in our discussion. The disorder flow is typified by two distinct fixed points. First of all, there is the trivial attractive fixed point at $\gamma_* = 0$. Here we find that $\nu = 0$ and $z = 1$, reflecting the irrelevance of the disorder perturbation. This fixed point is associated with the clean SM phase asymptotically described by the bare action Eq. (3.7), in which the DoS scales quadratically with the energy. Secondly there is a non-trivial fixed point at intermediate disorder $\gamma_* = \sqrt{\eta_0 \epsilon / 2}$. It is repulsive, separating the weakly disordered SM phase from the strongly disordered DM phase at critical value $\gamma_{0,c} = \gamma_*$. This SM-DM phase transition is characterized by a correlation length diverging with exponent ν. For the dynamical critical exponent we find from Eq. (3.30) that $z = 3/2$. Close to the critical point the Density of States is enhanced by strong disorder effects, scaling linearly away from the nodal point before becoming finite in the DM phase.

3.4.2 Untilted, interacting case

Alternatively we reflect on the basic model of an untitled Weyl cone with Coulomb interactions. Its purely isotropic limit was first studied in Ref. [83], and we here include the possibility of anisotropy in the Weyl fermion dispersion. We set out from the clean, untilted limit $t_0 = \gamma_0 = 0$. The primary β functions (3.22)-(3.25) reduce to

$$\beta_\eta = -\eta\alpha \left(F_\parallel^\eta - F_\perp^\eta \right), \qquad \beta_\alpha = -\alpha \left\{ \bar{\epsilon} + \alpha F_\parallel^\eta \right\}, \tag{3.33}$$

and the others vanishing. The two-dimensional flow described by these equations is presented in streamplot Fig.3.1. It is invariably directed towards the trivial non-interacting fixed point $\alpha_* = 0$ where also the isotropy is restored,
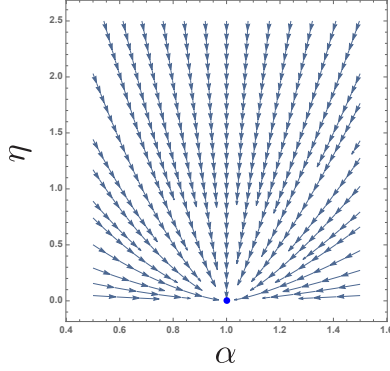
Figure 3.1: Streamplot of the flow deriving from equations (3.33) of the untilted but anisotropic and interacting model. Trivial fixed point in blue.

$\eta_* = 1$. The corresponding critical exponents are $\nu = 0$ and $z = 1$, reflecting the irrelevance of Coulomb interaction. The DoS receives logarithmic corrections that decrease it with compared to its free quadratic scaling behavior.

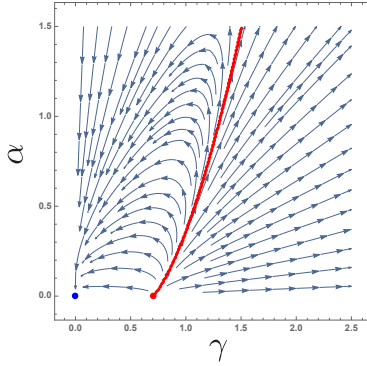### 3.4.3 Untilted, disordered, interacting case

Figure 3.2: Streamplot of the flow corresponding to the isotropic limit $\eta_0 = 1$ of equations (3.36) for the untilted model perturbed by disorder and interactions. Trivial fixed point in blue, numerical approximation of the phase boundary $\gamma_{0,c}$ between SM and DM in red.

Perturbing the free Weyl fermion model with both disorder and Coulomb

interactions, the setup studied in Refs. [61, 84] without anisotropy, means interplay effects might appear. The primary β functions are

$$\beta_\eta = -\eta\,\alpha\left(F_\parallel^\eta - F_\perp^\eta\right), \tag{3.34}$$

$$\beta_\alpha = \alpha\left\{-\bar{\epsilon} + \frac{1}{\eta}\gamma^2 - \alpha F_\parallel^\eta\right\}, \tag{3.35}$$

$$\beta_\gamma = \gamma\left\{-\frac{\epsilon}{2} + \frac{1}{\eta}\gamma^2 - \alpha F_\parallel^\eta\right\}. \tag{3.36}$$

which produce the two-dimensional flow depicted in Fig. 3.2 in the isotropic case $\eta_0 = 1$. Due to the different scaling dimensions of the perturbations these equations cannot simultaneously vanish at finite disorder and Coulomb interaction and there are no new fixed points. The anisotropy of the model influences the flow quantitatively but does not fundamentally change its topology as there is no competition in its β function. Within the SM region all flow is directed towards the previously encountered trivial point $\alpha_* = 0$, $\gamma_* = 0$ and $\eta_* = 1$ with exponents $\nu = 0$ and $z = 1$ at which the model is asymptotically free, clean and isotropic. In the disorder-only limit there is also the non-trivial fixed point for $\alpha_* = \alpha_0 = 0$ and $\gamma_* = \sqrt{\eta_* \epsilon/2}$ with $\eta_* = \eta_0$ that governs the phase transition into the DM state. It is perturbatively destabilized by the Coulomb interaction, extending into a phase boundary that expands the SM region towards higher disorder along which CLE is unchanged at $\nu = 1$ [61].

3.4.4 Tilted disordered case

We next introduce a tilt into the model of a Weyl fermion perturbed by disorder, as studied before in Ref. [39]. The β functions of interest reduce to

$$\beta_t = t\frac{1}{\eta\sqrt{1-t^2}}\gamma^2, \qquad\qquad \beta_\eta = -\eta\frac{t^2}{\eta'(1-t^2)^{3/2}}\gamma^2,$$

$$\beta_\gamma = \gamma\left\{-\frac{\epsilon}{2} + \frac{1}{\eta\sqrt{1-t^2}}\gamma^2\right\}. \tag{3.37}$$

By virtue of the identity $\beta_\eta/\eta = -t\beta_t/(1-t^2)$ the ratio $\eta^2/(1-t^2) = \eta_0^2/(1-t_0^2)$ is constant under renormalization group flow. Consequently the
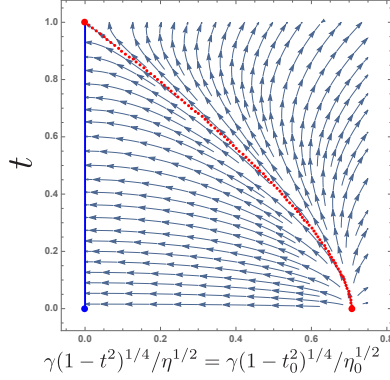
Figure 3.3: Streamplot of the flow deriving from equations (3.37) of the tilted disordered model. Line of trivial fixed points at $0 \geq t_* < 1$ in blue, numerical approximation of the phase boundary $\gamma_{0,c}$ between SM and DM in red.

flow corresponding to this set of three differential equations can summarized in the two-dimensional streamplot Fig. 3.3. The tilt shifts the boundary between semimetallic and diffusive metallic phases to lower critical disorder, see Fig. 3.4. Within the SM region, the flow is directed towards a line of clean fixed points at zero disorder $\gamma_* = 0$ and finite tilts $t_0 < t_* < 1$ and anisotropies $0 < \eta_* < \eta_0$. Note that this corresponds to values $0 < \lambda_* < 1$ for which the transformation Eq. (3.12) remains well-behaved. This fixed line inherits its exponents $\nu = 0$ and $z = 1$ from the trivial untilted and clean fixed point. The renormalized cone progessively tips over as the initial disorder approaches the critical value, see Fig. 3.5a. Similarly, the final anisotropy at the disorder-free line of fixed points decreases after flowing from more disordered points, going to zero towards the phase boundary, see Fig. 3.5b. The untilted nontrivial fixed point at $\gamma_* = \sqrt{\eta_0 \epsilon/2}$ with exponents $z = 3/2$ and $\nu = 1$ is destabilized by the inclusion of a tilt term in favor of a new fixed point along the phase boundary at $\gamma_* = (1 - t_*^2)^{1/4}\sqrt{\eta_* \epsilon/2}$ with $\eta_* \to 0$ and $t_* \to 1$. This new fixed point is however again characterized by critical exponents $z = 3/2$ and $\nu = 1$.

3.4.5 Tilted interacting case

Alternatively there is the case of the tilted Weyl fermion perturbed by Coulomb interactions, whose isotropic case was studied in Ref. [63]. The
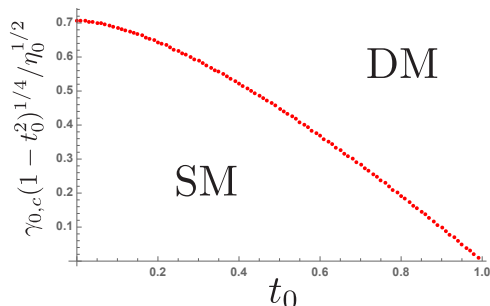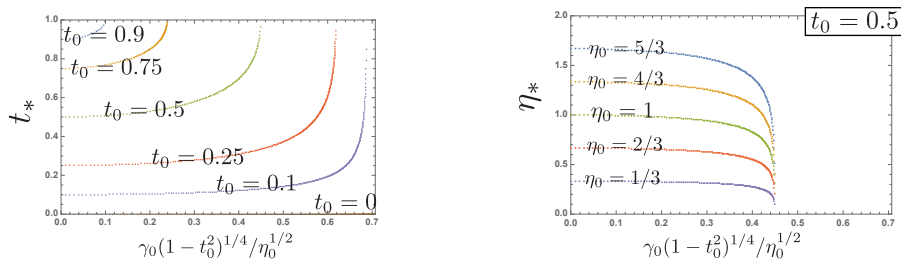
Figure 3.4: The critical initial disorder strength $\gamma_{0,c}$ of the SM-DM phase transition for $\alpha_0 = 0$ diminishes as initial tilt t_0 increases.

(a) t_* as function of a parameter combination proportional to γ_0 for arbitrary η_0.

(b) η_* as function of a parameter combination proportional to γ_0 for $t_0 = 1/2$.

Figure 3.5: Change of final tilt and anisotropy at the fixed line $\gamma_* = 0$ as a function of the initial parameters of the tilted disordered model.

set of β functions becomes

$$\beta_t = -t\alpha F_\parallel^\eta, \tag{3.38}$$

$$\beta_\eta = -\eta\alpha \left(F_\parallel^\eta - F_\perp^\eta \right), \tag{3.39}$$

$$\beta_\alpha = -\alpha \left\{ \bar{\epsilon} + \alpha F_\parallel^\eta \right\}. \tag{3.40}$$

The flow of the anisotropy and Coulomb interaction strength is independent of the tilt, and was previously depicted in the streamplot Fig. 3.1. The interactions will inevitably renormalize the tilt downwards, asymptotically restoring the isotropy of the Weyl cone. All flow is towards the untilted,

isotropic and non-interacting fixed point at $t_* = 0$, $\eta_* = 1$ and $\alpha_* = 0$ with exponents $\nu = 0$ and $z = 1$.

3.4.6 Full treatment: tilted, disordered and interacting case

(a) Front view. (b) Side view.
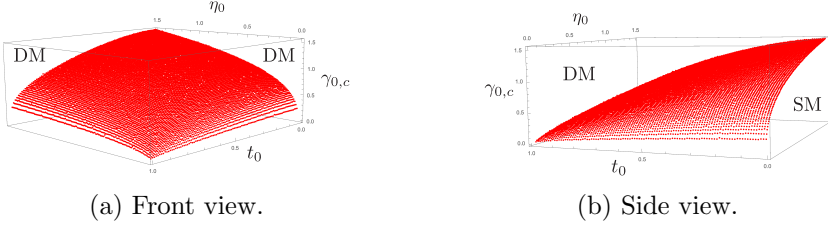
Figure 3.6: The critical initial disorder strength $\gamma_{0,c}$ of the SM-DM phase transition as a function of initial tilt t_0 and anisotropy η_0 for fixed ratio $\alpha/t = \alpha_0/t_0 = 1$.

We finally consider the full set of flow equations for the tilted anisotropic Weyl fermion under perturbation from disorder and Coulomb interactions, Eqs. (3.22)-(3.25). These perturbations have competing effects, which play out in both the bare parameters and the couplings themselves. Since Coulomb interaction is marginal on tree level it holds that $\beta_t/t = \beta_\alpha/\alpha$ meaning the ratio $\alpha/t = \alpha_0/t_0$ remains invariant under the RG transformation. A three-dimensional set of equations is then sufficient to capture the flow,

$$
\beta_t = t \left\{ \frac{1}{\eta\sqrt{1-t^2}} \gamma^2 - t\frac{\alpha_0}{t_0} F_\parallel^\eta \right\},
$$

$$
\beta_\eta = -\eta \left\{ \frac{t^2}{\eta'(1-t^2)^{3/2}} \gamma^2 + t\frac{\alpha_0}{t_0} \left(F_\parallel^\eta - F_\perp^\eta \right) \right\},
$$

$$
\beta_\gamma = \gamma \left\{ -\frac{\epsilon}{2} + \frac{1}{\eta\sqrt{1-t^2}} \gamma^2 - t\frac{\alpha_0}{t_0} F_\parallel^\eta \right\}. \tag{3.41}
$$

We numerically integrate these equations to study the SM-DM phase transition. Usefully we can use the spectator β function for λ, Eq. (3.136), to determine the value of the phase transition line as it only vanishes at $\lambda_* = 1$ for finite tilt and disorder. This procedure yields a two-dimensional phase boundary, depicted in Fig. 3.6, of the critical initial disorder $\gamma_{0,c}$ versus initial tilt t_0' and anisotropy η_0. In its vicinity the physics of the model

is controlled by the isotropic, untilted disordered but non-interacting fixed point with exponents $\nu = 1$ and $z \approx 3/2$. In the DM phase, for larger initial disorder content $\gamma_0 > \gamma_{0,c}$, the flow is directed towards strong disorder and ever larger Coulomb interactions. Within SM region $\gamma_0 < \gamma_{0,c}$ all flow is towards the trivial fixed point with $\nu = 0$ and $z = 1$, corresponding to the clean, free model. Due to the mismatch of the zeroth order scaling dimensions of the perturbations, $\bar{\epsilon} < \epsilon$, the Coulomb interactions scale out much more slowly at small couplings. As such, in the SM phase the Weyl cone is asymptotically upright and isotropic. The fixed line at $\gamma_* = 0$ with finite $t_* > 0$ and $\eta_* \neq 1$ encountered in the non-interacting case $\alpha_0 = 0$ is destabilized when Coulomb interactions are included.

3.5 Ward Identities and charge non-renormalization

From Eqs. (3.24)-(3.25) it is clear that the disorder and Coulomb interaction cannot have a fixed point at which these couplings are both finite. Although their first order corrections are identical, as the zeroth order scaling dimensions $\bar{\epsilon} \to 0, \epsilon \to 1$ differ simultaneous satisfaction of these equations is impossible.

We have found that this statement can be generalized, and that it so continues to hold to any order in perturbation theory. It is also independent of the presence of tilts and anisotropies in the dispersion. Disorder and Coulomb interaction couple in a very similar manner and have analogous perturbative expansions with diagrams of the same form. The polarization bubble, Fig. 3.7c, is regular using our $d = 2 + \epsilon$ dimensional regularization scheme. Therefore all diagrams that include it are subleading and can be neglected. In other words, neither the photon nor the disorder propagator obtains any renormalization at any order in perturbation theory. At a given order p, corrections come from all (one-particle irreducible) permutations of $2p$ vertices inserted on a single continuous fermion line. As such, all diagrams responsible for vertex renormalization can be exhaustively generated from self energy diagrams renormalizing the fermion propagator by introducing the suitable external vertex at all possible internal positions on the fermion

line [74]. Using the identity

$$\partial_{i\omega'} G'_{0,\chi}(i\omega - i\omega', \mathbf{k} - \mathbf{q})$$
$$= -G'_{0,\chi}(i\omega - i\omega', \mathbf{k} - \mathbf{q}) \, \hat{\lambda} \, G'_{0,\chi}(i\omega - i\omega', \mathbf{k} - \mathbf{q}), \qquad (3.42)$$

this might diagrammatically be depicted as

 $= -\Gamma \, \partial_{i\omega'} \, (\rightarrow\!\!\oslash\!\!\rightarrow) \, , \qquad$ $= -(ig) \, \partial_{i\omega'} \, (\rightarrow\!\!\oslash\!\!\rightarrow) \, , \quad (3.43)$

where the shaded areas represent the sum of all (one-particle irreducible) subdiagrams that can be used to connect the external legs and the derivative is understood to be taken with respect to the external frequency and applying the product rule. Note that the equality is only strictly valid for vanishing external frequency and momentum on the non-fermion third leg in the vertex diagram. However, contributions for finite inputs are irrelevant and may thus be disregarded for RG purposes. Due to the relations Eq. (3.43) vertex corrections will be exactly cancelled by the counterterms $\delta_{\psi'}$ for the fermion field and δ_λ for the field transformation parameter by the counter terms $\sim i\omega$ from the self-energy corrections. We then have identically vanishing counterterms $\delta_\Gamma = \delta_g = 0$. Such charge non-renormalization has been observed before in the 2d context of graphene by Ref. [85]. A consequence $\delta_\gamma = \delta_\alpha = -\delta_v$, at all orders in perturbation. The β functions of the dimensionless couplings can thus only differ in the tree level scaling dimensions $\bar\epsilon \to 0$, $\epsilon \to 1$, and a intermediate fixed point at finite disorder and Coulomb interaction cannot exist up to any order in perturbation theory.

In more general terms the non-renormalization of Γ and g can be identified as Ward identity deriving from the gauge invariance of the model. At its core it is but a particular manifestation of quantum electrodynamics, of which such symmetries are a defining characteristic. The Lagrangian contains a term of the form

$$\psi'^\dagger_{\omega,\mathbf{q}} \left[i\omega \, \delta(\omega - \omega')\delta(\mathbf{q} - \mathbf{q}') + ig \, \varphi_{\omega-\omega',\mathbf{q}-\mathbf{q}'} \right.$$
$$\left. + \Gamma \, \delta(\omega - \omega') \, V_{\mathbf{q}-\mathbf{q}'} \right] \hat{\lambda} \, \psi'_{\omega',\mathbf{q}'}, \qquad (3.44)$$

which can be obtained from the free Green function in Eq. (3.14) by a minimal coupling procedure. Here the disorder field V acts as an external field,

which should ordinarily couple to the fermion fields with equal charge g as the (scalar) gauge field $\varphi_{\omega,\mathbf{q}}$ mediating the electromagnetic interactions. This term would then be protected during renormalization flow by Ward identities, *i.e.*, gauge invariance, to all orders in perturbation theory, guaranteeing that $\delta_\Gamma = \delta_g = 0$. However as the zeroth order scaling of $\delta(\omega)V_{\mathbf{q}}$ does not match that of counterpart $\varphi_{\omega,\mathbf{q}}$, relative compensation between the dimensions of the couplings Γ and g is necessary. It is thus that the β functions of γ and α can only ever differ by the tree level scaling dimensions up to all orders in perturbation theory. Note furthermore that this argument applies to all type-I Weyl fermions including the untilted case [61], irrespective of possible tilts or anisotropies in their dispersion, as the $\hat{\lambda}$ field transformation preserves minimal coupling by construction.

3.6 Conclusion

Within this paper we studied type-I Weyl fermions including anisotropies and tilt and their physics if exposed to disorder and Coulomb interactions from an RG perspective. On a technical level, we find that a new term is generated under renormalization group flow, which we incorporate by means of the field transformation $\hat{\lambda}$ of Eq. (3.12). This transformation respects the minimal coupling between frequency $i\omega$ on the one hand and gauge field φ and external field V on the other hand. It also has ramifications on the other parameters of the model, as set out in Eq. (3.15).

Without tilts or anisotropies, disorder and Coulomb perturbations result in β functions that are the same except for the tree level scaling dimensions. Besides the attractive trivial fixed point, with exponents $\nu = 0$ and $z = 1$ there is only the repulsive non-interacting fixed point at finite disorder. It governs the SM-DM phase transition with critical exponents $\nu = 1$ and $z = 3/2$. There cannot be an intermediate fixed point at both finite disorder and finite Coulomb interaction [61].

Including a tilt and anisotropies does not lead to new terms in the coupling β functions, but only modifies them. It does not change the qualitative behavior and no new intermediate fixed point develops. Numerical integration shows that there is still a critical disorder value at which the system transitions from a weakly interacting and weakly disordered phase into a DM phase at strong interactions. It is a function of the initial values of the

parameters of the model, decreasing as a function of the tilt and anisotropy but increasing with the Coulomb interation.

Within the SM phase the flow is directed towards smaller couplings. Since Coulomb interaction is marginal it eventually dominates disorder perturbation which is irrelevant. Therefore, in the SM region, the flow is directed towards the attractive trivial fixed point at which the cone is upright and isotropic [63]. The attractive line of fixed points at which the tilt and anisotropy reach finite values to which the flow is directed in the tilted disordered model is particular to the complete absence of Coulomb interactions. When this is included it is immediately destabilized in favor of the trivial fixed point.

Importantly, we have found that these findings hold to all orders in perturbation theory, as the relation between frequency $i\omega$, gauge field ϕ and external disorder field V corresponds to a minimal coupling which is protected by a Ward identity. Including a tilt does not change this as the field transformation Eq. (3.12) uniformly affects the terms in Eq.(3.44). As a result, there cannot be any renormalization of the coupling parameters. The β functions of the disorder and Coulomb interactions only differ because of their different scaling dimensions. This implies that an intermediate fixed point at which both couplings are finite cannot exist. There is only the disorder driven phase transition into the DM phase from the SM phase, where Coulomb effects will dominate due to the due to the fact that they are less irrelevant.

3.7 Appendix: Perturbative analysis

Under anisotropic space-time rescaling $\omega \rightarrow \mu^{+z}\omega$, $\mathbf{q} \rightarrow \mu^{+1}\mathbf{q}$ the parameters and fields change as $y_i \rightarrow \mu^{+[y_i]}y_i$. Going beyond tree level in perturbation theory in the interactions of Eq. (3.19) will result in diagrammatic divergences that are to be cancelled by the inclusion of counterterms as $Z_{y_i} = 1 + \delta_{y_i}$. The divergences arising from the disorder perturbation are captured by regularization of the number of spatial dimensions $d = 2 + \epsilon$ [62]. Because the Coulomb interaction offers a marginal perturbation to the tree-level Weyl fermion indepedent of d, an additional expansion in $\bar{\epsilon}$ appearing the power of its propagator is required to absorb the resulting divergences.

Contributing diagrams are listed in Figs.(3.7)-(3.9). We have adhered to the convention to represent the fermion propagator $G_{0,\chi}$ as arrowed line, the photon propagator D_0 as wavy line and propagation of the disorder field by a dashed line. Vertices indicated by $\Gamma\hat{\lambda}$ derive from the disorder part Eq. (3.17) of the interacting action. Vertices indicated by $ig\hat{\lambda}$ come from the Coulomb part Eq. (3.18). Note here that all those graphs that have some dependence on the number of field replicas will vanish in the replica limit. Practically, this implies diagrams with a fermion loop connected purely by disorder legs can be safely neglected.

The derivation of these diagrammatic divergences is presented below. In calculating their divergences, we have often employed the generalized Feynman trick

$$A^{-n}B^{-r} = \frac{\Gamma[n+r]}{\Gamma[n]\Gamma[r]} \int_0^\infty \mathrm{d}u \, \frac{u^{n-1}}{(uA+B)^{n+r}} \qquad (3.45)$$

to handle the different powers of the denominators of the Weyl fermion and Coulomb boson propagators. Notationally, it has proved useful to define dimensionless couplings

$$\gamma'^2 = \frac{\Omega_d \, \mu^\epsilon}{(2\pi)^d \, v'^2} \, \Gamma^2, \qquad\qquad \alpha' = \frac{\Omega_d \, \mu^{\bar{\epsilon}}}{4(2\pi)^d \, v'} \, g^2, \qquad (3.46)$$

to shorten commonly occuring expressions.

(a) $\Sigma'_{\mathrm{dis}}(i\omega, \mathbf{k})$ (b) $\Sigma'_{\mathrm{Cou}}(i\omega, \mathbf{k})$ (c) $\Pi(i\omega, \mathbf{k})$
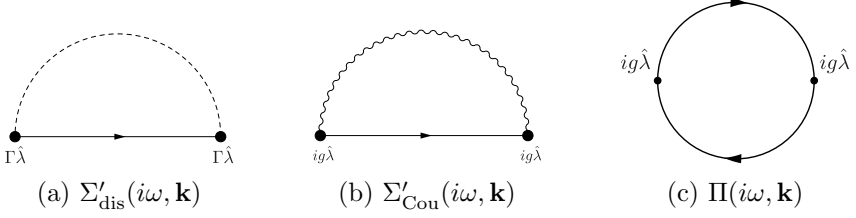
Figure 3.7: Self-energy corrections to the fermion Green function $G'_{0,\chi}$ and polarization contributing to renormalization of photon propagator D_0.

We first investigate the diagrams in Fig.(3.7), which will cause the renormalization of the parameters of the bare actions. The self-energy deriving from the disorder interaction yields

$$
\begin{aligned}
\mathrm{Fig.(3.7a)} &= \Sigma'_{\mathrm{dis}}(i\omega, \mathbf{k}) \\
&= \Gamma^2 \int_{\mathbf{q}} \hat{\lambda}\, G'_{0,\chi}(i\omega, \mathbf{q})\, \hat{\lambda} \\
&= -\frac{1}{2}\,\Gamma\left[1 - \frac{d}{2}\right] i\omega\,\gamma'^2\, \frac{1 + t'\lambda}{\eta'(1 - t'^2)^{3/2}}\, \hat{\lambda}(\sigma_0 - t'\chi\mathbf{d}\cdot\boldsymbol{\sigma})\hat{\lambda} \\
&= \left(\frac{1}{\epsilon}\right) i\omega\,\gamma'^2 \frac{1 + t'\lambda}{\eta'(1 - t'^2)^{3/2}}\left[\left((1 + \lambda^2) + 2t'\lambda\right)\sigma_0 \right. \\
&\quad \left. - \left(t'(1 + \lambda^2) + 2\lambda\right)\chi\mathbf{d}\cdot\boldsymbol{\sigma}\right] + O(\epsilon^0).
\end{aligned} \tag{3.47}
$$

On the other hand, the Coulomb self-energy reads

$$
\begin{aligned}
\mathrm{Fig.(3.7b)} &= \Sigma'_{\mathrm{Cou}}(i\omega, \mathbf{k}) \\
&= (ig)^2 \int_{\omega', \mathbf{q}} \hat{\lambda}\, G'_{0,\chi}(i\omega - i\omega', \mathbf{k} - \mathbf{q})\, \hat{\lambda}\, D_0(i\omega', \mathbf{q}) \\
&= -2\,\Gamma\left[-\frac{\bar{\epsilon}}{2}\right] v'\,\alpha'\, \hat{\lambda}\left[-F^{\eta}_{\parallel}\frac{k_{\parallel}}{1 - \lambda^2}(\lambda\sigma_0 + \chi\mathbf{d}\cdot\boldsymbol{\sigma}) \right. \\
&\quad \left. - \frac{\eta'}{1 + t'\lambda}F^{\eta}_{\perp}\chi\mathbf{k}_{\perp}\cdot\boldsymbol{\sigma}\right]\hat{\lambda} \\
&= \left(\frac{1}{\bar{\epsilon}}\right) v'\,\alpha'\left[F^{\eta}_{\parallel}k_{\parallel}(\lambda\sigma_0 - \chi\mathbf{d}\cdot\boldsymbol{\sigma}) \right. \\
&\quad \left. - \eta'\frac{1 - \lambda^2}{1 + t'\lambda}F^{\eta}_{\perp}\chi\mathbf{k}_{\perp}\cdot\boldsymbol{\sigma}\right] + O(\bar{\epsilon}^0),
\end{aligned} \tag{3.48}
$$

where $F_\parallel^\eta$ and $F_\perp^\eta$ are functions of the anisotropy parameter η,

$$F_\parallel^\eta = \frac{2}{\pi} \int_0^\infty \mathrm{d}u \; u^{(\bar\epsilon - 1)/2} (1+u)^{-3/2} (1+\eta'^2 u)^{(1-d)/2}$$

$$\left(k_\parallel^2 + \eta^2 k_\perp^2 \right)^{-\bar\epsilon/2} \left(\frac{k_\parallel^2}{1+u} + \frac{\eta^2 k_\perp^2}{1+\eta^2 u} \right)^{\bar\epsilon/2}, \tag{3.49}$$

$$F_\perp^\eta = \frac{2}{\pi} \int_0^\infty \mathrm{d}u \; u^{(\bar\epsilon - 1)/2} (1+u)^{-1/2} (1+\eta'^2 u)^{-(1+d)/2}$$

$$\left(k_\parallel^2 + \eta^2 k_\perp^2 \right)^{-\bar\epsilon/2} \left(\frac{k_\parallel^2}{1+u} + \frac{\eta^2 k_\perp^2}{1+\eta^2 u} \right)^{\bar\epsilon/2}. \tag{3.50}$$

Note that these functions are not divergent under $\bar\epsilon \to 0$. At zeroth order in $\bar\epsilon$, the integrals in Eqs. (3.49)-(3.50) can be done explicitly and functions reduce to the definitions given in Eqs. (3.97)-(3.98) of the main body. For the polarisation we find the expression

$$\mathrm{Fig.}(3.7\mathrm{c}) = \Pi(i\omega, \mathbf{k})$$

$$= -(ig)^2 \int_{\omega', \mathbf{q}} \mathrm{Tr} \left[\hat\lambda \, G'_{0,\chi}(i\omega', \mathbf{q}) \, \hat\lambda \, G'_{0,\chi}(i\omega' + i\omega, \mathbf{q} + \mathbf{k}) \right]$$

$$= -2^{m-d} \alpha' \left(\frac{d-1}{d} \right) \Gamma \left[\frac{d-1}{2} \right] \Gamma \left[\frac{3-d}{2} \right]$$

$$\frac{1-\lambda^2}{1+t'\lambda} (v'\eta')^{1-d} \mu^{d-3} k'^2$$

$$= O(\epsilon^0). \tag{3.51}$$
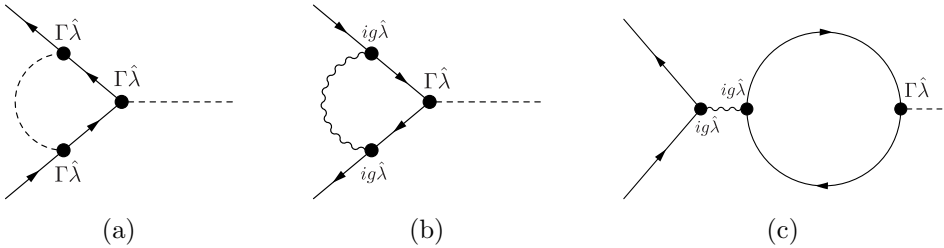
Figure 3.8: Vertex corrections to disorder coupling Γ.

Then there are the diagrams in Fig.(3.8), which will renormalize the disorder interaction strength Γ. The disorder-only leading order correction yields

$$
\begin{aligned}
\text{Fig.(3.8a)} &= \Gamma^3 \int_{\mathbf{q}} \left[\hat{\lambda}\, G'_{0,\chi}(i\omega, \mathbf{q}) \right]^2 \hat{\lambda} \\
&= \Gamma \left[1 - \frac{d}{2} \right] \frac{d-1}{2} \Gamma \gamma'^2 \frac{1 + t'\lambda}{\eta'(1 - t'^2)^{3/2}} \hat{\lambda}(\sigma_0 - t'\chi \mathbf{d} \cdot \boldsymbol{\sigma})\hat{\lambda} \\
&= -\left(\frac{1}{\epsilon} \right) \Gamma \gamma'^2 \frac{1 + t'\lambda}{\eta'(1 - t'^2)^{3/2}} \left[\left((1 + \lambda^2) + 2t'\lambda \right) \sigma_0 \right. \\
&\quad \left. - \left(t'(1 + \lambda^2) + 2\lambda \right) \chi \mathbf{d} \cdot \boldsymbol{\sigma} \right] + O(\epsilon^0),
\end{aligned}
\tag{3.52}
$$

whereas the mixed disorder-Coulomb diagram results in

$$
\text{Fig.(3.8b)} = \Gamma(ig)^2 \int_{\omega',\mathbf{q}} D_0(i\omega', \mathbf{q}) \left[\hat{\lambda}\, G'_{0,\chi}(i\omega - i\omega', \mathbf{k} - \mathbf{q}) \right]^2 \hat{\lambda} = 0.
\tag{3.53}
$$

Another perturbative contribution to the disorder vertex comes from the fermion loop diagram

$$
\begin{aligned}
\text{Fig.(3.8c)} &= -(ig)^2 \Gamma \hat{\lambda} \int_{\omega',\mathbf{q}} D_0(i\omega, \mathbf{k}) \\
&\qquad \text{Tr} \left[\hat{\lambda}\, G'_{0,\chi}(i\omega', \mathbf{q})\, \hat{\lambda}\, G'_{0,\chi}(i\omega' + i\omega, \mathbf{q} + \mathbf{k}) \right] \\
&= -2^{m-d} \alpha' \left(\frac{d-1}{d} \right) \Gamma \hat{\lambda} \left[\frac{d-1}{2} \right] \Gamma \left[\frac{3-d}{2} \right] \\
&\qquad \frac{1 - \lambda^2}{1 + t'\lambda} (v'\eta')^{1-d} \mu^{d-3} \\
&= O(\epsilon^0).
\end{aligned}
\tag{3.54}
$$

Lastly there are the diagrams in Fig.(3.9), which source the renormalization of the Coulomb interaction strength g. The purely Coulombic diagram vanishes identically,

$$
\begin{aligned}
&\text{Fig.(3.9a)} \\
&= (ig)^3 \int_{\omega',\mathbf{q}} D_0(i\omega', \mathbf{q}) \left[\hat{\lambda}\, G'_{0,\chi}(i\omega - i\omega', \mathbf{k} - \mathbf{q}) \right]^2 \hat{\lambda} \\
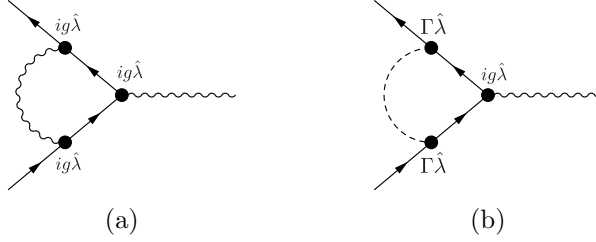&= 0,
\end{aligned}
\tag{3.55}
$$

Figure 3.9: Vertex corrections to the Coulomb coupling g.

in a restatement of gauge invariance. The mixed diagram however results in a finite contribution of the form

$$
\begin{aligned}
\text{Fig.(3.9b)} &= (ig)\Gamma^2 \int_{\omega',\mathbf{q}} \delta(\omega - \omega') \left[\hat{\lambda}\, G'_{0,\chi}(i\omega', \mathbf{q})\right]^2 \hat{\lambda} \\
&= \Gamma \left[1 - \frac{d}{2}\right] \frac{d-1}{2}(ig)\gamma'^2 \frac{1 + t'\lambda}{\eta'(1 - t'^2)^{3/2}} \hat{\lambda}(\sigma_0 - t'\chi\mathbf{d}\cdot\boldsymbol{\sigma})\hat{\lambda} \\
&= -\left(\frac{1}{\epsilon}\right)(ig)\,\gamma'^2 \frac{1 + t'\lambda}{\eta'(1 - t'^2)^{3/2}} \left[\left((1 + \lambda^2) + 2t'\lambda\right)\sigma_0 \right. \\
&\quad \left. - \left(t'(1 + \lambda^2) + 2\lambda\right)\chi\mathbf{d}\cdot\boldsymbol{\sigma}\right] + O(\epsilon^0).
\end{aligned}
\tag{3.56}
$$

Note that we might furthermore consider a pututative diagram in which an internal disorder line interpolates between an external Coulomb line and vertex point by means of an intermediate fermion loop. This however will have a momentum dependent result that is irrelevant in the RG sense and is therefore neglected.

3.8 Appendix: Counterterms and β functions

We now include counterterms to cancel the divergences in the diagrams of the perturbative expansion in the couplings. The renormalized self energy becomes

$$
\begin{aligned}
\Sigma'_R(i\omega, \mathbf{q}) &= \Sigma'_{\text{dis}}(i\omega, \mathbf{q}) + \Sigma'_{\text{Cou}}(i\omega, \mathbf{q}) \\
&\quad - \left\{\left(2\delta_{\psi'}i\omega - (2\delta_{\psi'} + \delta_{v'} + \delta_{t'})v't'q_\parallel\right)\sigma_0 \right. \\
&\quad \left. - \chi\left((2\delta_{\psi'} + \delta_{v'})v'q_\parallel\mathbf{d}\right)\right.
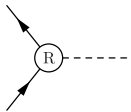\end{aligned}
$$

$$+ (2\delta_{\psi'} + \delta_{v'} + \delta_{\eta'})v'\eta'\mathbf{q}_\perp + (2\delta_{\psi'} + \delta_\lambda)i\omega\lambda\mathbf{d}) \cdot \boldsymbol{\sigma}\}$$

$$= i\omega\sigma_0 \left\{ \left(\frac{1}{\epsilon}\right) \gamma'^2 \frac{1+t'\lambda}{\eta'(1-t'^2)^{3/2}} \left((1+\lambda^2) + 2t'\lambda\right) - 2\delta_{\psi'} \right\}$$

$$- v't'q_\parallel\sigma_0 \left\{ -\left(\frac{1}{\bar{\epsilon}}\right) \alpha'\frac{\lambda}{t'}F_\parallel^\eta - \left(2\delta_{\psi'} + \delta_{v'} + \delta_{t'}\right) \right\}$$

$$- v'\chi q_\parallel\mathbf{d}\cdot\boldsymbol{\sigma} \left\{ \left(\frac{1}{\bar{\epsilon}}\right) \alpha'F_\parallel^\eta - \left(2\delta_{\psi'} + \delta_{v'}\right) \right\}$$

$$- v'\eta'\chi\mathbf{q}_\perp\cdot\boldsymbol{\sigma} \left\{ \left(\frac{1}{\bar{\epsilon}}\right) \alpha'\frac{1-\lambda^2}{1+t'\lambda}F_\perp^\eta - \left(2\delta_{\psi'} + \delta_{v'} + \delta_{\eta'}\right) \right\}$$

$$- i\omega\lambda\chi\mathbf{d}\cdot\boldsymbol{\sigma} \left\{ \left(\frac{1}{\epsilon}\right) \gamma'^2 \frac{1+t'\lambda}{\eta'(1-t'^2)^{3/2}} \left(t'(1+\lambda^2) + 2\lambda\right) \right.$$

$$\left. - \left(2\delta_{\psi'} + \delta_\lambda\right) \right\}$$

$$= 0. \tag{3.57}$$

Because the polarization diagram is regular under our renormalization scheme the photon field counterterm vanishes along the lines of

$$\Pi_R(i\omega, \mathbf{q}) = \Pi(i\omega, \mathbf{q}) - 2\delta_\varphi q^2 = 0. \tag{3.58}$$

The renormalization deriving form the vertex correction diagrams can be counteracted as

$$= \text{Figs.}(3.8)$$

$$+ \left\{ \left(2\delta_{\psi'} + \delta_\Gamma\right)\Gamma\sigma_0 - \left(2\delta_{\psi'} + \delta_\Gamma + \delta_\lambda\right)\Gamma\lambda\chi\mathbf{d}\cdot\boldsymbol{\sigma} \right\}$$

$$= \Gamma\sigma_0 \left\{ -\left(\frac{1}{\epsilon}\right) \gamma'^2 \frac{1+t'\lambda}{\eta'(1-t'^2)^{3/2}} \left((1+\lambda^2) + 2t'\lambda\right) \right.$$

$$\left. + \left(2\delta_{\psi'} + \delta_\Gamma\right) \right\}$$

$$- \Gamma\lambda\chi\mathbf{d}\cdot\boldsymbol{\sigma} \left\{ -\left(\frac{1}{\epsilon}\right) \gamma'^2 \frac{(1+t'\lambda)\left(t'(1+\lambda^2) + 2\lambda\right)}{\eta'(1-t'^2)^{3/2}} \right.$$

$$\left. + \left(2\delta_{\psi'} + \delta_\Gamma + \delta_\lambda\right) \right\}$$

$$= 0. \tag{3.59}$$

and

   $= \text{Figs.}(3.9)$

$$+ \left\{ \left(2\delta_{\psi'} + \delta_\varphi + \delta_g \right) ig\sigma_0 \right.$$
$$\left. - \left(2\delta_{\psi'} + \delta_\varphi + \delta_g + \delta_\lambda \right) ig\lambda\chi\mathbf{d}\cdot\boldsymbol{\sigma} \right\}$$
$$= ig\sigma_0 \left\{ -\left(\frac{1}{\epsilon}\right)\gamma'^2 \frac{1+t'\lambda}{\eta'(1-t'^2)^{3/2}} \left((1+\lambda^2) + 2t'\lambda)\right) \right.$$
$$\left. + \left(2\delta_{\psi'} + \delta_\varphi + \delta_g\right) \right\}$$
$$- ig\lambda\chi\mathbf{d}\cdot\boldsymbol{\sigma} \left\{ -\left(\frac{1}{\epsilon}\right)\gamma'^2 \frac{\left(1+t'\lambda\right)\left(t'(1+\lambda^2) + 2\lambda\right)}{\eta'(1-t'^2)^{3/2}} \right.$$
$$\left. + \left(2\delta_{\psi'} + \delta_\varphi + \delta_g + \delta_\lambda\right) \right\}$$
$$= 0. \tag{3.60}$$

Consequently, for the fields of the theory we find counterterms

$$2\delta_{\psi'} = \left(\frac{1}{\epsilon}\right)\gamma'^2 \frac{1+t'\lambda}{\eta'(1-t'^2)^{3/2}} \left((1+\lambda^2) + 2t'\lambda)\right), \tag{3.61}$$
$$\delta_\varphi = 0, \tag{3.62}$$

with which we also derive the terms neede to nullify the diagrammatic contributions to the tree level parameters,

$$\delta_{v'} = \left(\frac{1}{\bar\epsilon}\right)\alpha' F_\parallel^\eta - 2\delta_{\psi'}$$
$$= \left(\frac{1}{\bar\epsilon}\right)\alpha' F_\parallel^\eta - \left(\frac{1}{\epsilon}\right)\gamma'^2 \frac{1+t'\lambda}{\eta'(1-t'^2)^{3/2}} \left((1+\lambda^2) + 2t'\lambda)\right) \tag{3.63}$$
$$\delta_{t'} = -\left(\frac{1}{\bar\epsilon}\right)\alpha' \frac{\lambda}{t'} F_\parallel^\eta - 2\delta_{\psi'} - \delta_{v'},$$
$$= -\left(\frac{1}{\bar\epsilon}\right)\alpha' \left(\frac{\lambda}{t'} + 1\right) F_\parallel^\eta, \tag{3.64}$$
$$\delta_{\eta'} = \left(\frac{1}{\bar\epsilon}\right)\alpha' \frac{1-\lambda^2}{1+t'\lambda} F_\perp^\eta - 2\delta_{\psi'} - \delta_{v'}$$
$$= -\left(\frac{1}{\bar\epsilon}\right)\alpha' \left(F_\parallel^\eta - \frac{1-\lambda^2}{1+t'\lambda} F_\perp^\eta\right). \tag{3.65}$$

Because of gauge invariance the field counterterms will be exactly sufficient to cancel the divergences coming from the vertex diagrams so that the coupling strenghts are not renormalized and their counterterms vanish.

$$\delta_g = \left(\frac{1}{\epsilon}\right) \gamma'^2 \frac{1 + t'\lambda}{\eta(1 - t'^2)^{3/2}} \left((1 + \lambda^2) + 2t'\lambda)\right) - 2\delta_{\psi'} - \delta_\phi$$

$$= 0, \tag{3.66}$$

$$\delta_\Gamma = \left(\frac{1}{\epsilon}\right) \gamma'^2 \frac{1 + t'\lambda}{\eta'(1 - t'^2)^{3/2}} \left((1 + \lambda^2) + 2t'\lambda)\right) - 2\delta_{\psi'}$$

$$= 0. \tag{3.67}$$

Note that because $\delta_\phi = \delta_g = \delta_\Gamma = 0$, we also find consistently from the renormalization of the self energy and both the interaction vertices that

$$\delta_\lambda = \left(\frac{1}{\epsilon}\right) \gamma'^2 \frac{1 + t'\lambda}{\eta'(1 - t'^2)^{3/2}} \left(t'(1 + \lambda^2) + 2\lambda)\right) - 2\delta_{\psi'}$$

$$= \left(\frac{1}{\epsilon}\right) \gamma'^2 \frac{1 + t'\lambda}{\eta'(1 - t'^2)^{3/2}} (t' + \lambda)(1 - \lambda^2). \tag{3.68}$$

These counterterms lead to the flow equations

$$\beta_{v'} = v' \left\{ z - 1 + \alpha' F_\parallel^\eta - \gamma'^2 \frac{(1 + t'\lambda)\left((1 + \lambda^2) + 2t'\lambda\right)}{\eta'(1 - t'^2)^{3/2}} \right\}, \tag{3.69}$$

$$\beta_{t'} = -\alpha' \left(t' + \lambda\right) F_\parallel^\eta, \tag{3.70}$$

$$\beta_\lambda = \gamma'^2 \frac{(1 + t'\lambda)(t' + \lambda)}{\eta'(1 - t'^2)^{3/2}} (1 - \lambda^2), \tag{3.71}$$

$$\beta_{\eta'} = -\eta'\alpha' \left(F_\parallel^\eta - F_\perp^\eta\right), \tag{3.72}$$

$$\beta_{\alpha'} = \alpha' \left\{ -\bar\epsilon - \alpha' F_\parallel^\eta + \gamma'^2 \frac{(1 + t'\lambda)\left((1 + \lambda^2) + 2t'\lambda\right)}{\eta'(1 - t'^2)^{3/2}} \right\}, \tag{3.73}$$

$$\beta_{\gamma'} = \gamma' \left\{ -\frac{\epsilon}{2} - \alpha' F_\parallel^\eta + \gamma'^2 \frac{(1 + t'\lambda)\left((1 + \lambda^2) + 2t'\lambda\right)}{\eta'(1 - t'^2)^{3/2}} \right\}. \tag{3.74}$$

3.9 Appendix: Re-expressing the flow equations

We could proceed to analyze the set of equations presented in the previous section of the appendix, finding the flow's fixed points and then examining afterwards what these look like in terms of the original parameters of the theory by using Eq. (3.16),

$$v = v' \frac{1 + t'\lambda}{1 - \lambda^2}, \quad \eta = \eta' \frac{\sqrt{1 - \lambda^2}}{1 + t'\lambda}, \quad t = \frac{t' + \lambda}{1 + t'\lambda}.$$

We take an alternative strategy in which we use this equation to directly translate back the β functions into the language of the original model parameters as we have found this to significantly simplify their structure. The flow equations become

$$\beta_{v'} = v' \left\{ z - 1 - \gamma'^2 \frac{(1 + t\lambda)(1 - t\lambda)^2}{\eta(1 - t^2)^{3/2}} + \alpha' F_\parallel^\eta \right\}, \tag{3.75}$$

$$\beta_{t'} = -t \frac{1 - \lambda^2}{1 - t\lambda} \alpha' F_\parallel^\eta, \tag{3.76}$$

$$\beta_\lambda = t \frac{(1 - \lambda^2)(1 - t\lambda)^2}{\eta(1 - t^2)^{3/2}} \gamma'^2, \tag{3.77}$$

$$\beta_{\eta'} = -\eta' \alpha' \left(F_\parallel^\eta - (1 - t\lambda) F_\perp^\eta \right), \tag{3.78}$$

$$\beta_{\alpha'} = \alpha' \left\{ -\bar{\epsilon} + \gamma'^2 \frac{(1 + t\lambda)(1 - t\lambda)^2}{\eta(1 - t^2)^{3/2}} - \alpha' F_\parallel^\eta \right\}, \tag{3.79}$$

$$\beta_{\gamma'} = \gamma' \left\{ -\frac{\epsilon}{2} + \gamma'^2 \frac{(1 + t\lambda)(1 - t\lambda)^2}{\eta(1 - t^2)^{3/2}} - \alpha' F_\parallel^\eta \right\}. \tag{3.80}$$

The β functions for the original Fermi velocity v, fermion anisotropy η and tilt t are straightforward combinations of the above through redefinitions Eq. (3.16). This yields

$$
\begin{aligned}
\beta_v &= v \left\{ \frac{\beta_{v'}}{v'} + \frac{\lambda}{1 + t'\lambda} \beta_{t'} + \frac{t' + 2\lambda + t'\lambda^2}{(1 + t'\lambda)(1 - \lambda^2)} \beta_\lambda \right\} \\
&= v \left\{ \frac{\beta_{v'}}{v'} + \frac{\lambda(1 - t\lambda)}{1 - \lambda^2} \beta_{t'} + \frac{t + \lambda}{1 - \lambda^2} \beta_\lambda \right\} \\
&= v \left\{ z - 1 - \frac{(1 - t\lambda)^2}{\eta(1 - t^2)^{1/2}} \gamma'^2 + (1 - t\lambda) \alpha' F_\parallel^\eta \right\}, \tag{3.81}
\end{aligned}
$$

and

$$\begin{aligned}
\beta_t &= t \left\{ \frac{1 - \lambda^2}{(t' + \lambda)(1 + t'\lambda)} \beta_{t'} + \frac{1 - t'^2}{(t' + \lambda)(1 + t'\lambda)} \beta_\lambda \right\} \\
&= t \left\{ \frac{(1 - t\lambda)^2}{t(1 - \lambda^2)} \beta_{t'} + \frac{1 - t^2}{t(1 - \lambda^2)} \beta_\lambda \right\} \\
&= -t \left\{ (1 - t\lambda)\alpha' F_\parallel^\eta - \frac{(1 - t\lambda)^2}{\eta(1 - t^2)^{1/2}} \gamma'^2 \right\},
\end{aligned} \tag{3.82}$$

and

$$\begin{aligned}
\beta_\eta &= \eta \left\{ \frac{\beta_{\eta'}}{\eta'} - \frac{\lambda}{1 + t'\lambda} \beta_{t'} - \frac{t' + \lambda}{(1 + t'\lambda)(1 - \lambda^2)} \beta_\lambda \right\} \\
&= \eta \left\{ \frac{\beta_{\eta'}}{\eta'} - \frac{\lambda(1 - t\lambda)}{1 - \lambda^2} \beta_{t'} - \frac{t}{1 - \lambda^2} \beta_\lambda \right\} \\
&= -\eta \left\{ (1 - t\lambda) \left(F_\parallel^\eta - F_\perp^\eta \right) \alpha' + t \frac{(1 - t\lambda)^2}{\eta(1 - t^2)^{3/2}} \gamma'^2 \right\}.
\end{aligned} \tag{3.83}$$

We can simplify further with by redefining the couplings to those set out in Eq. (3.134) of the main body,

$$\gamma^2 = \frac{\Omega_d \, \mu^\epsilon}{(2\pi)^d \, v^2} \, \Gamma^2, \qquad\qquad \alpha = \frac{\Omega_d \, \mu^{\bar\epsilon}}{4(2\pi)^d \, v} \, g^2.$$

In terms of these, we find

$$\beta_v = v \left\{ z - 1 - \frac{1}{\eta\sqrt{1 - t^2}} \gamma^2 + \alpha F_\parallel^\eta \right\}, \tag{3.84}$$

$$\beta_t = -t \left\{ \alpha F_\parallel^\eta - \frac{1}{\eta\sqrt{1 - t^2}} \gamma^2 \right\}, \tag{3.85}$$

$$\beta_\eta = -\eta \left\{ \alpha \left(F_\parallel^\eta - F_\perp^\eta \right) + \frac{t^2}{\eta(1 - t^2)^{3/2}} \gamma^2 \right\}, \tag{3.86}$$

$$\beta_\lambda = t \frac{1 - \lambda^2}{\eta(1 - t^2)^{3/2}} \gamma^2. \tag{3.87}$$

The flow of the redefined couplings themselves is determined by the equations

$$\begin{aligned}
\beta_\alpha &= \alpha \left(\frac{\beta_{\alpha'}}{\alpha'} + \frac{\beta_{v'}}{v'} - \frac{\beta_v}{v} \right) \\
&= \alpha \left\{ -\bar\epsilon + \frac{1}{\eta\sqrt{1 - t^2}} \gamma^2 - \alpha F_\parallel^\eta \right\},
\end{aligned} \tag{3.88}$$

$$\beta_\gamma = \gamma \left(\frac{\beta_{\gamma'}}{\gamma'} + \frac{\beta_{v'}}{v'} - \frac{\beta_v}{v} \right)$$

$$= \gamma \left\{ -\frac{\epsilon}{2} + \frac{1}{\eta\sqrt{1-t^2}}\gamma^2 - \alpha F_\parallel^\eta \right\}. \tag{3.89}$$

Taken together these form the set of four coupled equations Eqs. (3.22)-(3.25) and two further decoupled equations Eqs. (3.135)-(3.136).

3.10 Appendix: Alternative momentum shell scheme

Applying the perturbative momentum shell scheme set out in subsubsection 1.3.4 to the disordered interacting action leads to several complications that make it hard to draw definite conclusions. Imposing the cylindrical cutoff Λ on the perpendicular momentum direction implies fixing the energy scale, implicitly breaking gauge invariance [1]. Nevertheless it is instructive to see how these difficulties arise and what kind of flow equations they give rise to.

The model we consider is given by Eq. (3.19), with some important modifications. The number of spatial dimension is fixed to $d = 3$. The bare photon propagator is taken to be

$$D_0^{-1} = q_\parallel^2 + \zeta^2 q_\perp^2, \tag{3.90}$$

where we have allowed for the possibility of anisotropy entering the photonic dispersion. The disorder scattering amplitude is dependent on the angle

$$\theta = \theta_{\mathbf{q}} = \arctan(\eta q_\perp / \sqrt{1-t^2} q_\parallel) \tag{3.91}$$

that is a function of the disorder boson's momentum $\mathbf{q}$. We can then Fourier decompose the disorder strength as

$$\Gamma_\theta = \sum_{m=-\infty}^{\infty} \Gamma^{(2m)} e^{2i\theta m}, \tag{3.92}$$

where the angular momentum modes $\Gamma^{(2m)}$ may be independently renormalized. As before, a field transformation Eq. (3.12) is performed to introduce a parameter λ to take into account quasiparticle density renormalization effects.

Contributing diagrams are those listed in Figs.(3.7)-(3.9). We first calculate the expressions corresponding to the diagrams in Fig.(3.7), which will be the primary cause of renormalization of the parameters of the bare actions. The self-energy deriving from the disorder interaction yields

$$\text{Fig.(3.7a)} = \Sigma'_{\text{dis}}(i\omega, \mathbf{k})$$

$$= \int_{\omega'} \int_{\mathbf{q}}' \Gamma^2_{\theta_{\mathbf{q}-\mathbf{k}}} \hat\lambda G'_{0,\chi}(i\omega', \mathbf{q}) \hat\lambda \delta(\omega - \omega') \approx \int_{\mathbf{q}}' \Gamma^2_{\theta_{\mathbf{q}}} \hat\lambda G'_{0,\chi}(i\omega, \mathbf{q}) \hat\lambda$$

$$\approx - \left\{ \frac{1 + t'\lambda}{\eta'(1 - t'^2)^{3/2}} \left(A'^{(0)} \sigma_0 - B'^{(0)} \chi \mathbf{d} \cdot \boldsymbol{\sigma} \right) \right.$$

$$\left. + \frac{t' + \lambda}{\eta'(1 - t'^2)^{3/2}} \left(B'^{(2)} \sigma_0 - A'^{(2)} \chi \mathbf{d} \cdot \boldsymbol{\sigma} \right) \right\} i\omega\, l, \qquad (3.93)$$

where we have used dimensionless couplings

$$\gamma'^{(2m)} = \frac{\Gamma^{(2m)}\sqrt{\Lambda}}{2\sqrt{\pi}\, v'}, \qquad\qquad \alpha' = \frac{g^2}{4\pi^2 v'}. \qquad (3.94)$$

Also, $A'^{(2m)}$ and $B'^{(2m)}$ are modes of convolutions of the disorder strength as defined by

$$A'^{(2m)} = \left((1 + \lambda^2) + 2t'\lambda \right) \left(\gamma' * \gamma' \right)^{(2m)} \qquad (3.95)$$

$$B'^{(2m)} = \left(t'(1 + \lambda^2) + 2\lambda \right) \left(\gamma' * \gamma' \right)^{(2m)}.$$

On the other hand, the Coulomb self-energy reads

$$\text{Fig.(3.7b)} = \Sigma'_{\text{Cou}}(i\omega, \mathbf{k}) \qquad\qquad\qquad\qquad\qquad\qquad (3.96)$$

$$= (ig)^2 \int_{\omega'} \int_{\mathbf{q}}' \hat\lambda G'_{0,\chi}(i\omega, \mathbf{q}) \hat\lambda D_0(i\omega - i\omega', \mathbf{k} - \mathbf{q})$$

$$\approx -v' \frac{\alpha'}{\zeta^2} \left[F^{\tilde{x}}_{\parallel} k_{\parallel} (\lambda \sigma_0 - \chi \mathbf{d} \cdot \boldsymbol{\sigma}) - \frac{\eta'}{2} \chi \frac{1 - \lambda^2}{1 + t'\lambda} F^{\tilde{x}}_{\perp} \mathbf{k}_{\perp} \cdot \boldsymbol{\sigma} \right] l,$$

where we have defined two functions

$$F^{\tilde{x}}_{\parallel} = \left(\frac{1}{1 - \tilde{x}^2} - \frac{\tilde{x}^2 \operatorname{arctanh}\sqrt{1 - \tilde{x}^2}}{(1 - \tilde{x}^2)^{3/2}} \right), \qquad (3.97)$$

$$F^{\tilde{x}}_{\perp} = - \left(\frac{1}{1 - \tilde{x}^2} - \frac{(2 - \tilde{x}^2) \operatorname{arctanh}\sqrt{1 - \tilde{x}^2}}{(1 - \tilde{x}^2)^{3/2}} \right) \qquad (3.98)$$

that depend on the ratio $\tilde{x}^2 = \eta^2/\zeta^2$. If the anisotropies in boson and fermion sectors equilibrate then $\tilde{x} = 1$ and these functions simplify to $F_\parallel^{\tilde{x}=1} = 2/3$ and $F_\perp^{\tilde{x}=1} = 4/3$. For the polarisation we find the expression

$$
\text{Fig.}(3.7\text{c}) = \Pi(0, \mathbf{k})
$$

$$
= -(ig)^2 \int_\omega \int_{\mathbf{q}}' \text{Tr}\left[\hat{\lambda}\, G'_{0,\chi}(i\omega, \mathbf{q})\, \hat{\lambda}\, G'_{0,\chi}(i\omega, \mathbf{q} + \mathbf{k})\right]
$$

$$
\approx -\frac{1}{3}\frac{\alpha'}{\eta'^2}(1 + t'\lambda)\left[k_\parallel^2 + \frac{\eta'^2(1 - \lambda^2)}{(1 + t'\lambda)^2}k_\perp^2\right] l. \tag{3.99}
$$

Then there are the diagrams in Fig.(3.8), which will renormalize the disorder interaction strength Γ_θ. Their contributions can be absorbed by in a mode by mode expansion in angle θ. The disorder-only leading order correction yields

$$
\text{Fig.}(3.8\text{a}) = \Gamma_{\theta_{\mathbf{k}}}\int_{\mathbf{q}}' \Gamma_{\theta_{\mathbf{q}}}^2\left[\hat{\lambda}\, G'_{0,\chi}(i\omega, \mathbf{q})\right]^2\hat{\lambda}
$$

$$
\approx \sum_m e^{2i\theta_{\mathbf{k}}m}\Gamma^{(2m)}\left\{\frac{1 + t'\lambda}{\eta'(1 - t'^2)^{3/2}}\left[A'^{(0)}\sigma_0 - B'^{(0)}\chi\mathbf{d}\cdot\boldsymbol{\sigma}\right]\right.
$$

$$
\left.+ \frac{t' + \lambda}{\eta'(1 - t'^2)^{3/2}}\left[B'^{(2)}\sigma_0 - A'^{(2)}\chi\mathbf{d}\cdot\boldsymbol{\sigma}\right]\right\} l, \tag{3.100}
$$

whereas the mixed disorder-Coulomb diagram results in

$$
\text{Fig.}(3.8\text{b}) = \Gamma_{\theta_{\mathbf{k}}}(ig)^2 \int_\omega \int_{\mathbf{q}}'\left(\hat{\lambda}\, G'_{0,\chi}(i\omega, \mathbf{q})\right)^2\hat{\lambda}D_0(\omega, \mathbf{q})
$$

$$
= 0. \tag{3.101}
$$

Another perturbative contribution to the disorder vertex comes from the

fermion loop diagram

$$\text{Fig.(3.8c)} = -\Gamma_{\theta_\mathbf{k}}(ig)^2\hat{\lambda} \int_{\omega'}' \int_\mathbf{q}' D_0(i\omega, \mathbf{k})$$

$$\text{Tr}\left[\hat{\lambda}\, G'_{0,\chi}(i\omega', \mathbf{q})\, \hat{\lambda}\, G'_{0,\chi}(i\omega', \mathbf{q}+\mathbf{k})\right]$$

$$\approx -\frac{1}{3}\frac{\alpha'}{\eta'^2}(1-t'^2)\sum_m e^{2i\theta_\mathbf{k} m}\left[\frac{1+t'\lambda}{1-t'^2}\,(\Gamma * f^x_\parallel)\right.$$

$$\left. + \frac{1-\lambda^2}{1+t'\lambda}\,(\Gamma * f^x_\perp)\right]^{(2m)} (\sigma_0 - \lambda\chi\mathbf{d}\cdot\boldsymbol{\sigma})\, l, \qquad (3.102)$$

where we have also defined the Fourier decomposition modes of two functions that contain the angle dependence,

$$(f^x_\parallel)^{(2m)} = \int_{-\pi}^\pi \frac{\mathrm{d}\theta}{2\pi}\, e^{2i\theta m}\frac{1}{1+\tan^2(\theta)/x^2}, \qquad (3.103)$$

$$(f^x_\perp)^{(2m)} = \int_{-\pi}^\pi \frac{\mathrm{d}\theta}{2\pi}\, e^{2i\theta m}\frac{\tan^2(\theta)}{1+\tan^2(\theta)/x^2}, \qquad (3.104)$$

They depend on a variant of the anisotropy ratio parameter, $x^2 = \tilde{x}^2/(1-t^2)$.

Lastly there are the diagrams in Fig.(3.9), which source the renormalization of the Coulomb interaction strength g. The purely Coulombic diagram vanishes identically,

$$\text{Fig.(3.9a)} = (ig)^3 \int_\omega \int_\mathbf{q}' \left[\hat{\lambda}\, G'_{0,\chi}(i\omega, \mathbf{q})\right]^2 \hat{\lambda} D_0(i\omega, \mathbf{q})$$

$$= 0, \qquad (3.105)$$

in a restatement of gauge invariance. The mixed diagram however results in a finite contribution of the form

$$\text{Fig.(3.9b)} = ig \int_\mathbf{q}' \Gamma_{\theta_\mathbf{q}}^2 \left[\hat{\lambda}\, G'_{0,\chi}(i\omega, \mathbf{q})\right]^2 \hat{\lambda}$$

$$\approx ig\left\{\frac{1+t'\lambda}{\eta'(1-t'^2)^{3/2}}\left[A'^{(0)}\sigma_0 - B'^{(0)}\chi\mathbf{d}\cdot\boldsymbol{\sigma}\right]\right.$$

$$\left. + \frac{t'+\lambda}{\eta'(1-t'^2)^{3/2}}\left[B'^{(2)}\sigma_0 - A'^{(2)}\chi\mathbf{d}\cdot\boldsymbol{\sigma}\right]\right\} l. \qquad (3.106)$$

Note that we might furthermore consider a pututative diagram in which an internal disorder line interpolates between external Coulomb line and corresponding vertex by means of an intermediate fermion loop. This however will have a momentum dependent result that is irrelevant in the RG sense and is therefore neglected.

We then collect all the diagrammatic contributions, so they may be absorbed by renormalization constants that will be introduced as $\psi' \to Z_{\psi'}^{-1}\psi'$, $\varphi \to Z_\varphi^{-1}\varphi$, $v' \to Z_{v'}^{-1}v'$, $t' \to Z_{t'}^{-1}t'$, $\lambda \to Z_\lambda^{-1}\lambda$, $\eta' \to Z_{\eta'}^{-1}\eta'$, $\zeta^2 \to Z_{\zeta^2}^{-1}\zeta^2$, $\Gamma^{(2m)} \to Z_{\Gamma^{(2m)}}^{-1}\Gamma^{(2m)}$, $g \to Z_g^{-1}g$.

First of all, we may use Dyson equation to determine how to pick the constants appearing in the free fermion and boson actions. For convience, we here reproduce the (inverse) free fermion Green function Eq. (3.14),

$$
G'_{0,\chi}(i\omega, \mathbf{k})^{-1} = i\omega\,(\sigma_0 - \lambda\chi\mathbf{d}\cdot\boldsymbol{\sigma}) - v'\left[k_\parallel(t'\sigma_0 + \chi\mathbf{d}\cdot\boldsymbol{\sigma}) + \eta'\chi\mathbf{k}_\perp\cdot\boldsymbol{\sigma}\right].
$$

By Dyson equation, we then have that

$$
\begin{aligned}
G'_\chi(i\omega, \mathbf{k})^{-1} &= G'_{0,\chi}(i\omega, \mathbf{k})^{-1} - \Sigma'_{\text{dis}}(i\omega, \mathbf{k}) - \Sigma'_{\text{Cou}}(i\omega, \mathbf{k})\\
&= i\omega\left\{1 + \left[\frac{(1 + t'\lambda)A'^{(0)}}{\eta'(1 - t'^2)^{3/2}} + \frac{(t' + \lambda)B'^{(2)}}{\eta'(1 - t'^2)^{3/2}}\right]l\right\}\sigma_0\\
&\quad - i\omega\lambda\left\{1 + \left[\frac{(1 + t'\lambda)B'^{(0)}}{\eta'(1 - t'^2)^{3/2}} + \frac{(t' + \lambda)A'^{(2)}}{\eta'(1 - t'^2)^{3/2}}\right]\frac{l}{\lambda}\right\}\mathbf{d}\cdot\boldsymbol{\sigma}\\
&\quad - v't'k_\parallel\left\{1 - \frac{\alpha'}{\zeta^2}\frac{\lambda}{t'}F_\parallel^{\tilde{x}}l\right\}\sigma_0 - v'k_\parallel\left\{1 + \frac{\alpha'}{\zeta^2}F_\parallel^{\tilde{x}}l\right\}\chi\mathbf{d}\cdot\boldsymbol{\sigma}\\
&\quad - v'\eta'\left\{1 + \frac{1}{2}\frac{\alpha'}{\zeta^2}\frac{1 - \lambda^2}{1 + t'\lambda}F_\perp^{\tilde{x}}l\right\}\chi\mathbf{k}_\perp\cdot\boldsymbol{\sigma}\\
&= i\omega Z_{\psi'}^2\,\sigma_0 - i\omega\lambda\,Z_{\psi'}^2 Z_\lambda\,\chi\mathbf{d}\cdot\boldsymbol{\sigma} - v't'\,Z_{\psi'}^2 Z_{v'} Z_{t'}\,k_\parallel\sigma_0\\
&\quad - v'\,Z_{\psi'}^2 Z_{v'}\,\chi k_\parallel\mathbf{d}\cdot\boldsymbol{\sigma} - v'\eta'\,Z_{\psi'}^2 Z_{v'} Z_{\eta'}\,\chi\mathbf{k}_\perp\cdot\boldsymbol{\sigma} \qquad (3.107)
\end{aligned}
$$

We should thus pick the renormalization constants of the free fermionic

theory parameters as

$$Z_{\psi'}^2 = 1 + \left[\frac{(1 + t'\lambda)A'^{(0)}}{\eta'(1 - t'^2)^{3/2}} + \frac{(t' + \lambda)B'^{(2)}}{\eta'(1 - t'^2)^{3/2}} \right] l, \tag{3.108}$$

$$Z_\lambda = Z_{\psi'}^{-2} \left\{ 1 + \left[\frac{(1 + t'\lambda)B'^{(0)}}{\eta'(1 - t'^2)^{3/2}} + \frac{(t' + \lambda)A'^{(2)}}{\eta'(1 - t'^2)^{3/2}} \right] \frac{l}{\lambda} \right\}, \tag{3.109}$$

$$Z_{v'} = Z_{\psi'}^{-2} \left\{ 1 + \frac{\alpha'}{\zeta^2} F_\parallel^{\tilde{x}} l \right\}, \tag{3.110}$$

$$Z_{t'} = Z_{\psi'}^{-2} Z_{v'}^{-1} \left\{ 1 - \frac{\alpha'}{\zeta^2} \frac{\lambda}{t'} F_\parallel^{\tilde{x}} l \right\}, \tag{3.111}$$

$$Z_{\eta'} = Z_{\psi'}^{-2} Z_{v'}^{-1} \left\{ 1 + \frac{1}{2} \frac{\alpha'}{\zeta^2} \frac{1 - \lambda^2}{1 + t'\lambda} F_\perp^{\tilde{x}} l \right\}. \tag{3.112}$$

Proceeding similarly for the bosonic free action, we have the (inverse) propagator of Eq. (3.90)

$$D_0(i\omega, \mathbf{k})^{-1} = k_\parallel^2 + \zeta^2 k_\perp^2,$$

and we see by Dyson equation that

$$\begin{aligned} D(i\omega, \mathbf{k})^{-1} &= D_0(i\omega, \mathbf{k})^{-1} - \Pi(0, \mathbf{k}) \\ &= \left\{ 1 + \frac{1}{3} \frac{\alpha'}{\eta'^2} (1 + t'\lambda) l \right\} k_\parallel^2 + \zeta^2 \left\{ 1 + \frac{1}{3} \frac{\alpha'}{\zeta^2} \frac{1 - \lambda^2}{1 + t'\lambda} l \right\} k_\perp^2 \\ &= Z_\varphi^2 \, k_\parallel^2 + \zeta^2 \, Z_\varphi^2 Z_{\zeta^2} \, k_\perp^2. \end{aligned} \tag{3.113}$$

In order to preserve scale-invariance, we learn that we should pick the renormalization coefficients for the free bosonic parameters as

$$Z_\varphi = 1 + \frac{1}{6} \frac{\alpha'}{\eta'^2} (1 + t'\lambda) l, \tag{3.114}$$

$$Z_{\zeta^2} = Z_\varphi^{-1} \left\{ 1 + \frac{1}{3} \frac{\alpha'}{\zeta^2} \frac{1 - \lambda^2}{1 + t'\lambda} l \right\}. \tag{3.115}$$

We next progress to the interacting part of the action. Under changes of

the cutoff scale the disorder term transforms as

$$
= \sum_m e^{2i\theta_{\mathbf{k}}m} \Gamma^{(2m)} \left[\left\{ 1 - \frac{1}{3} \frac{\alpha'}{\eta^2} \frac{1}{\gamma^{(2m)}} (1 - t'^2) \right. \right.
$$

$$
\left[\frac{1 + t'\lambda}{1 - t'^2} (\gamma' * f_\parallel^x) + \frac{1 - \lambda^2}{1 + t'\lambda} (\gamma' * f_\perp^x) \right]^{(2m)} l
$$

$$
+ \left[\frac{(1 + t'\lambda)A'^{(0)}}{\eta'(1 - t'^2)^{3/2}} + \frac{(t' + \lambda)B'^{(2)}}{\eta'(1 - t'^2)^{3/2}} \right] l \bigg\} \sigma_0
$$

$$
- \lambda \left\{ 1 - \frac{1}{3} \frac{\alpha'}{\eta'^2} \frac{1}{\gamma'^{(2m)}} (1 - t'^2) \right.
$$

$$
\left[\frac{1 + t'\lambda}{1 - t'^2} (\gamma' * f_\parallel^x) + \frac{1 - \lambda^2}{1 + t'\lambda} (\gamma' * f_\perp^x) \right]^{(2m)} l
$$

$$
+ \left. \left[\frac{(1 + t'\lambda)B'^{(0)}}{\eta'(1 - t'^2)^{3/2}} + \frac{(t' + \lambda)A'^{(2)}}{\eta'(1 - t'^2)^{3/2}} \right] \frac{l}{\lambda} \right\} \chi \mathbf{d} \cdot \boldsymbol{\sigma} \right]
$$

$$
= \sum_m e^{2i\theta_{\mathbf{k}}m} Z_{\psi'}^2 Z_{\Gamma^{(2m)}} \Gamma^{(2m)} \left(\sigma_0 - Z_\lambda \lambda \chi \mathbf{d} \cdot \boldsymbol{\sigma} \right). \qquad (3.116)
$$

In order to remain invariant, we should have

$$
Z_{\Gamma^{(2m)}} = Z_{\psi'}^{-2} \left\{ 1 - \frac{1}{3} \frac{\alpha'}{\eta'^2} \frac{1}{\gamma'^{(2m)}} (1 - t'^2) \right.
$$

$$
\left[\frac{1 + t'\lambda}{1 - t'^2} (\gamma' * f_\parallel^x) + \frac{1 - \lambda^2}{1 + t'\lambda} (\gamma' * f_\perp^x) \right]^{(2m)} l
$$

$$
+ \left. \left[\frac{(1 + t'\lambda)A'^{(0)}}{\eta'(1 - t'^2)^{3/2}} + \frac{(t' + \lambda)B'^{(2)}}{\eta'(1 - t'^2)^{3/2}} \right] l \right\}, \qquad (3.117)
$$

$$Z_\lambda = Z_{\psi'}^{-2} Z_{\Gamma^{(2m)}}^{-1} \left\{ 1 - \frac{1}{3} \frac{\alpha'}{\eta'^2} \frac{1}{\gamma'^{(2m)}} (1 - t'^2) \right.$$

$$\left[\frac{1 + t'\lambda}{1 - t'^2} (\gamma' * f_\parallel^x) + \frac{1 - \lambda^2}{1 + t'\lambda} (\gamma' * f_\perp^x) \right]^{(2m)} l$$

$$\left. + \left[\frac{(1 + t'\lambda)B'^{(0)}}{\eta'(1 - t'^2)^{3/2}} + \frac{(t' + \lambda)A'^{(2)}}{\eta(1 - t'^2)^{3/2}} \right] \frac{l}{\lambda} \right\}, \qquad (3.118)$$

The Coulomb part of the interacting action instead transforms as

$$= ig \left\{ 1 + \left[\frac{(1 + t'\lambda)A'^{(0)}}{\eta'(1 - t'^2)^{3/2}} + \frac{(t' + \lambda)B'^{(2)}}{\eta'(1 - t'^2)^{3/2}} \right] l \right\} \sigma_0$$

$$- ig\lambda \left\{ 1 + \left[\frac{(1 + t'\lambda)B'^{(0)}}{\eta'(1 - t'^2)^{3/2}} + \frac{(t' + \lambda)A'^{(2)}}{\eta'(1 - t'^2)^{3/2}} \right] \frac{l}{\lambda} \right\} \chi \mathbf{d} \cdot \boldsymbol{\sigma}$$

$$= ig Z_g Z_\varphi Z_{\psi'}^2 \left(\sigma_0 - Z_\lambda \lambda \chi \mathbf{d} \cdot \boldsymbol{\sigma} \right). \qquad (3.119)$$

Thus, to remain invariant under changes of the cutoff scale, we should have

$$Z_g = Z_{\psi'}^{-2} Z_\varphi^{-1} \left\{ 1 + \left[\frac{(1 + t'\lambda)A'^{(0)}}{\eta'(1 - t'^2)^{3/2}} + \frac{(t' + \lambda)B'^{(2)}}{\eta'(1 - t'^2)^{3/2}} \right] l \right\}, \qquad (3.120)$$

$$Z_\lambda = Z_{\psi'}^{-2} Z_\varphi^{-1} Z_g^{-1} \left\{ 1 + \left[\frac{(1 + t'\lambda)B'^{(0)}}{\eta'(1 - t'^2)^{3/2}} + \frac{(t' + \lambda)A'^{(2)}}{\eta'(1 - t'^2)^{3/2}} \right] \frac{l}{\lambda} \right\}, \qquad (3.121)$$

Note that the expressions Eq. (3.109), Eq. (3.118) and Eq. (3.121), which arrive at the renormalization of λ in three very different ways, coincide beautifully. Minding also the zeroth order scaling dimensions the flow equations

for the free theory parameters are

$$\beta_{v'} = v' \left\{ z - 1 + \frac{\alpha'}{\zeta^2} F_{\parallel}^{\tilde{x}} - \left[\frac{(1 + t'\lambda)A'^{(0)}}{\eta'(1 - t'^2)^{3/2}} + \frac{(t' + \lambda)B'^{(2)}}{\eta'(1 - t'^2)^{3/2}} \right] \right\}, \qquad (3.122)$$

$$\beta_{t'} = -\frac{\alpha'}{\zeta^2}(t' + \lambda)F_{\parallel}^{\tilde{x}}, \qquad (3.123)$$

$$\beta_{\lambda} = \left[\frac{1 + t'\lambda}{\eta'(1 - t'^2)^{3/2}}(B - \lambda A)^{(0)} + \frac{t' + \lambda}{\eta'(1 - t'^2)^{3/2}}(A - \lambda B)^{(2)} \right], \qquad (3.124)$$

$$\beta_{\eta'} = -\eta' \frac{\alpha'}{\zeta^2} \left(F_{\parallel}^{\tilde{x}} - \frac{1}{2} \frac{1 - \lambda^2}{1 + t'\lambda} F_{\perp}^{\tilde{x}} \right), \qquad (3.125)$$

$$\beta_{\zeta^2} = -\alpha' \frac{1}{3}(1 + t'\lambda) \left(\frac{\zeta^2}{\eta'^2} - \frac{1 - \lambda^2}{(1 + t'\lambda)^2} \right). \qquad (3.126)$$

To be consistent we should look at the flow of the dimensionless couplings Eq. (3.94). Their equations are straightforward combinations

$$\begin{aligned}
\beta_{\alpha'} &= \alpha' \left(2\frac{\beta_g}{g} - \frac{\beta_{v'}}{v'} \right) \\
&= -\frac{\alpha'^2}{\zeta^2} \left(\frac{1}{3} \frac{\zeta^2}{\eta'^2}(1 + t'\lambda) + F_{\parallel}^{\tilde{x}} \right) \\
&\quad + \alpha' \left[\frac{(1 + t'\lambda)A'^{(0)}}{\eta'(1 - t'^2)^{3/2}} + \frac{(t' + \lambda)B'^{(2)}}{\eta'(1 - t'^2)^{3/2}} \right], \qquad (3.127)
\end{aligned}$$

$$\begin{aligned}
\beta_{\gamma'^{(2m)}} &= \gamma'^{(2m)} \left(\frac{\beta_{\Gamma^{(2m)}}}{\Gamma^{(2m)}} - \frac{\beta_{v'}}{v'} \right), \\
&= -\frac{1}{2}\gamma'^{(2m)} - \frac{\alpha'}{\zeta^2} F_{\parallel}^{\tilde{x}} \gamma'^{(2m)} \\
&\quad + \left[\frac{(1 + t'\lambda)A'^{(0)}}{\eta'(1 - t'^2)^{3/2}} + \frac{(t' + \lambda)B'^{(2)}}{\eta'(1 - t'^2)^{3/2}} \right] \gamma'^{(2m)} \\
&\quad - \frac{\alpha'}{\eta'^2} \frac{1}{3}(1 - t'^2) \left[\frac{1 + t'\lambda}{1 - t'^2}(\gamma' * f_{\parallel}^x) + \frac{1 - \lambda^2}{1 + t'\lambda}(\gamma' * f_{\perp}^x) \right]^{(2m)}. \quad (3.128)
\end{aligned}$$

We can then use Eq. (3.16) to directly translate back the β functions into the language of the original model parameters.

This results in a primary set of five coupled flow equations

$$\beta_\eta = -\eta \frac{\alpha}{\zeta^2}\left(F_\parallel^{\tilde{x}} - \frac{1}{2}F_\perp^{\tilde{x}}\right) - \eta \frac{t^2}{\eta(1-t^2)^{3/2}}\left[(\gamma * \gamma)^{(0)} + (\gamma * \gamma)^{(2)}\right],$$

(3.129)

$$\beta_{\zeta^2} = -\alpha \frac{1}{3}\left(\frac{\zeta^2}{\eta^2} - 1\right),$$

(3.130)

$$\beta_t = -t\frac{\alpha}{\zeta^2}F_\parallel^{\tilde{x}} + \frac{t}{\eta(1-t^2)^{3/2}}\left[(\gamma * \gamma)^{(0)} + (\gamma * \gamma)^{(2)}\right],$$

(3.131)

$$\beta_{\gamma^{(2m)}} = -\frac{1}{2}\gamma^{(2m)} - \frac{\alpha}{\zeta^2}F_\parallel^{\tilde{x}}\gamma^{(2m)} + \frac{(\gamma * \gamma)^{(0)}}{\eta(1-t^2)^{1/2}}\gamma^{(2m)}$$
$$- \frac{\alpha}{\eta^2}\frac{1}{3}\left[(\gamma * f_\parallel^x) + (1-t^2)(\gamma * f_\perp^x)\right]^{(2m)},$$

(3.132)

$$\beta_\alpha = -\frac{\alpha^2}{\zeta^2}F_\parallel^{\tilde{x}} + \alpha\frac{(\gamma * \gamma)^{(0)}}{\eta(1-t^2)^{1/2}} - \frac{\alpha^2}{\eta^2}\frac{1}{3}.$$

(3.133)

where $\beta_{y_i} = dy_i/dl$ for parameters y_i and $*$ denotes the convolution operation. Note also that we have used dimensionless couplings

$$\gamma^{(2m)} = \frac{\Gamma^{(2m)}\sqrt{\Lambda}}{2\sqrt{\pi}\,v}, \qquad \alpha = \frac{g^2}{4\pi^2 v},$$

(3.134)

that are more amenable to RG analysis. All anisotropic effects enter a single predetermined ratio only. We can capture the flow of the anisotropy in both the bosonic and the fermionic sector in the parameter $\tilde{x}^2 = \eta^2/\zeta^2$.

Once the flow of the model is determined through the coupled set Eqs. (3.129)-(3.133), the behavior of the remaining parameters can be investigated by means of the decoupled secondary equations

$$\beta_v = v\left\{z - 1 + \frac{\alpha}{\zeta^2}F_\parallel^{\tilde{x}} - \frac{(\gamma * \gamma)^{(0)}}{\eta(1-t^2)^{1/2}}\right\},$$

(3.135)

$$\beta_\lambda = t\frac{1-\lambda^2}{\eta(1-t^2)^{3/2}}\left[(\gamma * \gamma)^{(0)} + (\gamma * \gamma)^{(2)}\right].$$

(3.136)

Part II

Monopole stabilization in interpenetrating pyrochlore lattices

4 Monopole stabilization in interpenetrating pyrochlore lattices

This chapter is based on unpublished work performed during a research visit to the Theory of Condensed Matter (TCM) Group at the University of Cambridge, UK, under supervision of dr. Claudio Castelnovo.

4.1 Introduction

In 1935, L. Pauling realized that the relative orientation of the molecules in water precludes full ordering even if all thermal fluctuations are frozen out at absolute zero [86]. Within a molecule of H_2O the atoms are tied together by strong covalent bonds, developing an angle between the hydrogen protons that give the unit a charge polarity. This results in a preferential orientation of the positive hydrogen legs towards the negative oxygen center, forming dipolar bonds that are relatively weaker in strength. When the water is fully frozen out, every oxygen mediates two of these intermolecular bonds and is thus surrounded by its own two hydrogen protons nearby and two hydrogen protons that are farther away. The number of configurations that obey this ground state rule grows exponentially with the size of the system, corresponding to an extensive residual entropy at zero temperature. These predictions were proven correct by measurements of the specific heat, which is defined as the change in entropy with temperature [87].

Some twenty years later P. W. Anderson detected a remarkable similarity of this model of water ice and the Ising antiferromagnet on the pyrochlore lattice [88]. This is a network of corner-sharing tetrahedra, on which the spins' binary degree of freedom emulates the two different proximities of hydrogen atoms to an oxygen atom in water ice. The interactions of the spins play out along edges of the triangular sides of the tetrahedra, by which they cannot all be satisfied simultaneously. Such frustration leads to a ground state with a large degree of degeneracy, which has a characteristic two spins pointing in and two spins pointing out of every tetrahedron. In reference

to the analogy with water ice this ground state rule has become known as the spin ice rule [89]. Several materials have since been found to realize the spin ice model on the pyrochlore lattice through the presence of strong anisotropies that reduce the spins to antiferromagnetically coupled binary degrees of freedom [90, 91].

Interest in these spin ice compounds surged when it was realized that the ice rule can be understood as a divergence free condition of an effective field of the magnetization. Under the two-in two-out rule there is as much of this field entering a tetrahedron as there is exiting, coming to a net zero flux. A flip of a spin can then be interpreted as the creation of a monopole-antimonopole pair in the two tetrahedra it resides on, which generates a non-zero flux between them [92]. Recently, it was found that a non-uniform magnetic field, on every site locally directed away from or towards the tetrahedron's center of gravity, can function as a chemical potential for the monopole degrees of freedom of spin ice. Such a field may effectively be imposed by interactions with a secondary, dual pyrochlore lattice, whose Heisenberg spins collectively point into or out of the tetrahedra due to the effects of Dzyaloshinksy-Moriya interactions [93].

In comparison to the scale of the anisotropy driven ordering occuring in the pure spin ice model the pinning of the Heisenberg spins on the dual pyrochlore lattice is considerably softer [94]. As such, there is scope for competition with the interaction that couples the two interpenetrating lattices. Depending on the configuration of the Ising-like spins in the tetrahedra of the strongly anisotropic pyrochlore this interlattice coupling come to prefer a deviation from the all-in all-out setting induced by the Dzyaloshinksy-Moriya interactions on the dual lattice. Conversely, such a small angle deviation in the Heisenberg spin all-in or all-out ordering generates a perpendicular component to the local magnetic field that could lead to transitions in Ising-like spin ground state manifold.

The remainder of this chapter is constituted as follows. In section 4.2 we introduce the pyrochlore lattice and look at the famous spin ice model that describes the spins ordering in it in various material compounds. In section 4.3 we introduce another, interpenetrating pyrochlore lattice, whose collectively co-ordering Heisenberg spins result in an effective local magnetic field on top of the spin ice model. In section 4.4 we then study the effects of a small angle deviation from the co-ordering of these secondary spins. In sec-

tion 4.5 we investigate which configurations will be maximally influenced by the deviation on some finite plaquettes, which we match to results obtained by Monte Carlo simulation in section 4.6. We finish with a conclusion in section 4.7. Lastly, in a short appendix 4.8 we present the coordinates for some important vectors in two convenient reference frames that may be used to check most calculations presented in the other sections explicitly.
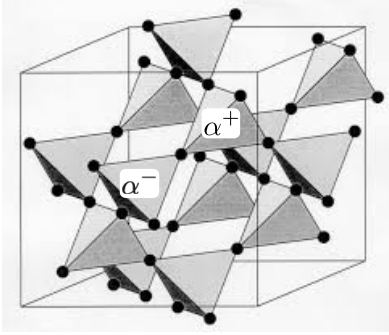
4.2 Pyrochlore lattices and the spin ice model

The pyrochlore lattice is a structure that has played an outsized role in modern condensed matter physics. It is a network of alternatingly inverted tetrahedra α^+ and α^- that are connected at the corners, see Fig. 4.1a. In certain compounds that crystallize in this lattice structure, such as $Ho_2Ti_2O_7$ (HTO) and $Dy_2Ti_2O_7$ (DTO), strong anisotropy restricts the spins to align with or against their local trigonal direction [91, 95]. We indicate the unit axis corresponding to such a direction at one of the four inequivalent sites i in some tetrahedron $\alpha^\pm$ by $\hat{u}_i^\pm = \pm\hat{u}_i$, see Fig. 4.2a. Note that unit vectors $\hat{u}_i$ are directed exactly away from the center of positive tetrahedra α^+ but towards the center of negative tetrahedra α^-. Under such conditions the magnetic moment $\boldsymbol{\sigma}_{\alpha_i^\pm}$ at $\alpha_i^\pm$ may then be expressed as $\boldsymbol{\sigma}_{\alpha_i^\pm} = \sigma_{\alpha_i^\pm}\hat{u}_i^\pm = \sigma_{\alpha_i}\hat{u}_i$. The remaining degree of freedom lies in the Ising-like variable $\sigma_{\alpha_i} \in \{+1, -1\}$, which determines whether the spin points out of/into the plus tetrahedron α^+ and into/out of the minus tetrahedron α^-. Due to the high degree of symmetry in the geometry of a tetrahedron the local axes add up to zero. Furthermore, any two of them are at the same angle so that their dot product is constant,

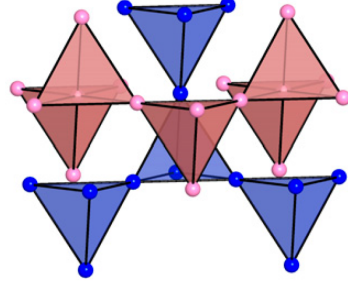$$\sum_i \hat{u}_i = \hat{u}_1 + \hat{u}_2 + \hat{u}_3 + \hat{u}_4 = 0, \qquad \hat{u}_i \cdot \hat{u}_j = \begin{cases} 1 & \text{for } i = j, \\ -\frac{1}{3} & \text{for } i \neq j. \end{cases}$$

$$(4.1)$$

Due to these anisotropies the Hamiltonian with ferromagnetic (FM) nearest neighbor coupling $J > 0$, for which degeneracies would not be expected in general, that describes the spin interactions in these substances is recast

(a) Pyrochlore lattice [96].

(b) Interpenetrating pyrochlore lattices [97].

Figure 4.1: The pyrochlore lattice is a network of corner-sharing tetrahedra that leaves room for meshing of two copies.

as

$$H^{\text{spin ice}} = -J \sum_{\langle \alpha_i, \beta_j \rangle} \boldsymbol{\sigma}_{\alpha_i} \cdot \boldsymbol{\sigma}_{\beta_j} = -J \sum_{\langle \alpha_i, \beta_j \rangle} \sigma_{\alpha_i} \sigma_{\beta_j} \hat{u}_i \cdot \hat{u}_j$$

$$= -J^{\text{eff}} \sum_{\langle \alpha_i, \beta_j \rangle} \sigma_{\alpha_i} \sigma_{\beta_j} = -\frac{1}{2} J^{\text{eff}} \sum_{\alpha} \sum_{i,j \neq i} \sigma_{\alpha_i} \sigma_{\alpha_j}, \qquad (4.2)$$

where we have found an effective coupling $J^{\text{eff}} = -J/3 < 0$ between the Ising-like degrees of freedom. The resulting antiferromagnetic (AFM) interaction is highly frustrated due to the triangular composition of the tetrahedral unit cell. Ground states are characterized by the spin ice rule

$$\sum_i \sigma_{\alpha_i} = \sigma_{\alpha_1} + \sigma_{\alpha_2} + \sigma_{\alpha_3} + \sigma_{\alpha_4} = 0 \qquad \forall \alpha, \qquad (4.3)$$

which states that every ground state tetrahedron must have two inwards-pointing spins and two outwards-pointing spins. This rule is not sufficient to eliminate all degeneracies even at zero temperature [89]. Most saliently, excitations above these ground states can be interpreted as monopole-animonopole pairs of an effective magnetic field, see Fig. 4.3. Such excitations have remained unobserved as fundamental particles, but are allowed by Maxwell's equations [92]. We define the monopole charge residing in some tetrahedron

(a) Local trigonal axes $\hat{u}_i$ of the four vertices of a tetrahedron.

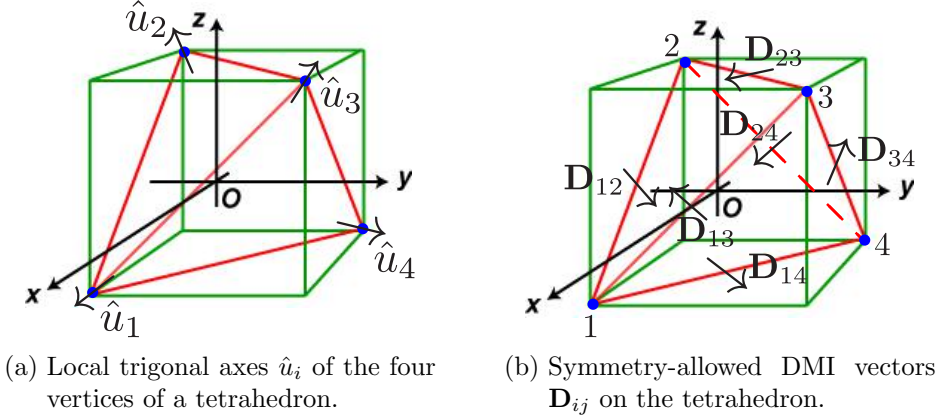(b) Symmetry-allowed DMI vectors $\mathbf{D}_{ij}$ on the tetrahedron.

Figure 4.2: Local trigonal axes $\hat{u}_i$ and DMI vectors $\mathbf{D}_{ij}$ in a plus tetrahedron in the pyrochlore lattice, portrayed in the edge-up reference frame set up in appendix subsec. 4.8.1.

$\alpha^\pm$ as

$$Q_{\alpha^\pm} = \frac{1}{2} \sum_i \sigma_{\alpha_i^\pm} = \pm \frac{1}{2} \sum_i \sigma_{\alpha_i} \tag{4.4}$$

in order to measure spin flips out of the 2-in-2-out (2i2o) ground state manifold defined by the spin ice rule. In terms of these charges the Hamiltonian becomes

$$H^{\text{spin ice}} = -\frac{1}{2} J^{\text{eff}} \sum_\alpha \sum_{i,j \neq i} \sigma_{\alpha_i} \sigma_{\alpha_j} = -\frac{1}{2} J^{\text{eff}} \sum_\alpha \left[\left(\sum_i \sigma_{\alpha_i} \right)^2 - \sum_i \sigma_{\alpha_i}^2 \right]$$

$$= -2 J^{\text{eff}} \sum_{\pm,\alpha^\pm} (Q_{\alpha^\pm}^2 - 1). \tag{4.5}$$

In confirmation of the spin ice rule, this transformation shows that the disordered two-in two-out (2i2o) manifold, with all tetrahedra holding a vanishing charge $Q_{\alpha^\pm} = 0$ and contributing $2J^{\text{eff}} < 0$ to the energy, is most advantageous. Higher in the hierarchy sit the disordered one-in three-out (1i3o) and three-in one out (3i1o) states, which have respective charge $Q_{\alpha^\pm} = \pm 1$ and $Q_{\alpha^\pm} = \mp 1$ and a vanishing energy per tetrahedron. The ordered all-out (Ao) and all-in (Ai) states, in which spins collectively co-align or contra-align

with their local direction, have the highest energy $-6J^{\mathrm{eff}} > 0$ and a charge of $Q_{\alpha\pm} = \pm 2$ and $Q_{\alpha\pm} = \mp 2$ per tetrahedron.
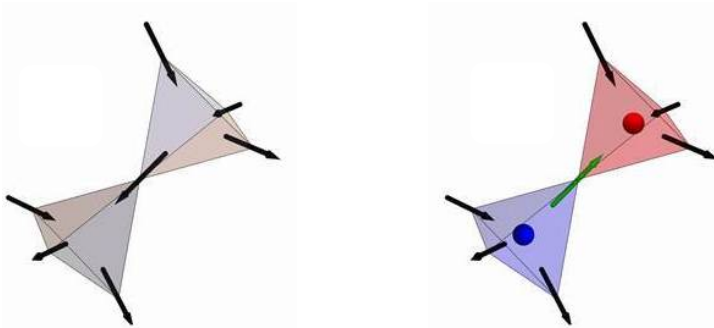

Figure 4.3: Flipping the shared spin on the two charge neutral trehedra α^+ and α^- on the left-hand side that obey the spin ice rule creates the monopole-antimonopole pair excitation with charge $Q_{\alpha\pm} = \pm 1$ per tetrahedron on the right-hand side [98].

Unlike in the pyrochlore titinates mentioned above, in the iridates $R_2\mathrm{Ir}_2\mathrm{O}_7$ both the rare-earth ions R and the iridium ions are magnetic and crystallize on interpenetrating pyrochlore lattices, see Fig. 4.1b. Whereas the physics of the rare-earth sublattice is highly specific to the atomic species investigated, the behavior of the iridium spins is more uniform [99]. Their mutual coupling is antiferromagnetic in nature, $J_{\mathrm{Ir}} < 0$, and due to their relatively isotropic crystal neighborhood their orientations are unconstrained. Writing $\mathbf{S}_{a_i}$ for a spin-1/2 vector degree of freedom on site i in a tetrahedron labelled a, the iridium sublattice exchange Hamiltonian can be rewritten as

$$H_{\mathrm{Ir}}^{\mathrm{ex.}} = -J_{\mathrm{Ir}} \sum_{\langle a_i, b_j \rangle} \mathbf{S}_{a_i} \cdot \mathbf{S}_{b_j} = -\frac{J_{\mathrm{Ir}}}{2} \sum_a \sum_{i, j \neq i} \mathbf{S}_{a_i} \cdot \mathbf{S}_{a_j}$$

$$= -\frac{J_{\mathrm{Ir}}}{2} \sum_a \left[\left(\sum_i \mathbf{S}_{a_i} \right)^2 - 4 \right]. \tag{4.6}$$

Hence, the iridium interaction energy is minimized for configurations where

the sum of spins on every tetrahedron a vanishes, or

$$\sum_i \mathbf{S}_{a_i} = \mathbf{S}_{a_1} + \mathbf{S}_{a_2} + \mathbf{S}_{a_3} + \mathbf{S}_{a_4} = 0. \tag{4.7}$$

Since the tetrahedra in the pyrochlore lattice are corner-sharing, this condition leaves a large number of degenerate ground states and an absence of long-range order in the model [100]. Single spin updates cannot be used to connect different states in the manifold, because a change at some site most be compensated for by manipulating at least one spin in both the plus as the minus tetrahedra it sits on. Updates in which two spins in a tetrahedron are redirected must take the form of a rotation in the plane perpendicular to their sum, guaranteeing continued compliance with the vanishing sum rule in Eq. (4.7). Ground states can then be connected by concatenating this procedure into closed trajectories. In this way any ground state can be continuously deformed into another without leaving the manifold [101].

Another effect derives from the fact that iridium is a relatively heavy element, and is therefore less affected by anisotropy. This opens the ground to further effects such as Dzyaloshinsky-Moriya (DM) interactions, which can no longer safely be neglected. The DM interactions that can play out in a system are confined by the symmetries of the lattice. On the iridium pyrochlore sublattice these restrictions are sufficient to uniquely establish the allowed axes of the scalar triple product of this interaction, see Fig. 4.2b, which can be decomposed into the familiar local axes as

$$\mathbf{D}_{ij} = \frac{3}{2\sqrt{2}} \, (\hat{u}_i \times \hat{u}_j). \tag{4.8}$$

The only degree of freedom remaining in the DM interaction is then captured in a sign. For $D_{\mathrm{Ir}} > 0$ we speak of direct DM interactions, whereas $D_{\mathrm{Ir}} < 0$ corresponds to indirect interactions [102]. Indirect interactions will lead to a mere reduction in the number of ground states, while direct-type DM breaks down the ground state manifold to the Ao and Ai states in which the Heisenberg spins are softly pinned to their local axes.

In some pyrochlore iridates, notably $Ho_2Ir_2O_7$ (HIO) and $Dy_2Ir_2O_7$ (DIO), the rare-earth ions interact ferromagnetically and are restricted by strong local easy axis anisotropy along the trigonal direction of their tetragonal

sites. The total model we study is then comprised of the spin ice Hamiltonian Eq. (4.2) on the rare-earth sublattice, antiferromagnetically coupled Heisenberg spins with DM interactions on the iridium sites and an exchange interaction coupling the two sublattices,

$$H = -J_R^{\text{eff}} \sum_{\langle \alpha_i, \beta_j \rangle} \sigma_{\alpha_i} \sigma_{\beta_j} - J_{\text{Ir}} \sum_{\langle a_i, b_j \rangle} \mathbf{S}_{a_i} \cdot \mathbf{S}_{b_j}$$
$$- D_{\text{ir}} \sum_{\langle a_i, b_j \rangle} \mathbf{D}_{ij} \cdot (\mathbf{S}_{a_i} \times \mathbf{S}_{b_j}) - J_{\text{Ir}-R} \sum_{\langle a_i, \alpha_j \rangle} \mathbf{S}_{a_i} \cdot \boldsymbol{\sigma}_{\alpha_j}. \qquad (4.9)$$

Clearly there is scope for competition between the energy scales set by the different coupling constants. Most of all we are interested in the behavior of the system as a function of the coupling $J_{\text{Ir-R}}$ between the iridium and rare-earth, which has the potential to change the physics of one or both of the two sublattices. In practice, the energy hierarchy is topped by the iridium couplings, where the AFM exchange is at least an order of magnitude larger than the positive DM interactions [102].

Since the lattice structure does not change much between them and the rare-earth rare-earth interactions are mediated by the oxygen atoms, it is reasonable to assume that the neareast neighbor exchange coupling as well as the nearest neighbor dipolar interaction should be approximately equal in the iridates and the titinates [93]. The latter compounds have been studied extensively in the nearest-neighbor spin ice setting, and consequentially the values of their interaction strengths are well known. We present these in Table 4.1. We have also extracted the values for the iridium couplings mentioned in the literature for the iridates, and summarized them in Table 4.2.

4.3 Iridium sublattice collective co-ordering

Motivated by the hierarchy of realistic parameter values listed in Tables 4.1-4.2, our primary interest in the iridium sublattice is as arena for the dominant energy scale set by the interaction strength J_{Ir}. In the case of $Ho_2Ir_2O_7$ the direct DM interaction is similarly larger than the interactions relevant to the dysprosium sites, which will result in breaking of the symmetries between the states in the manifold that minimize the AFM Heisenberg

J_R^{eff}	literature value	measurement technique
HTO	-1.8K [103]	MC fitting to neutron scattering measurements
DTO	-1.1K [104]	MC fitting to height and temperature of specific heat peak
HIO	-1.4K [93]	MC fitting to diffraction measurements of Ho^{3+} magnetic moment
DIO	...K ?	...

Table 4.1: Effective nearest neighbor interaction strengths in pyrochlore holmium and dysprosium titanite and iridate, as found in the literature.

	literature value	measurement technique
D_{Ir}	~ 50K [94]	MC fitting to specific heat ordering transition at $T_{\text{MIT}} = 134$K (DIO) and $T_{\text{MIT}} = 141$K (HIO)
J_{Ir}	~ -500K [102]	J_{Ir} an order of magnitude larger than D_{Ir}
$J_{\text{Ir}-R}$	$4.9 - 6.3$K (HIO) [93]	fitting of CEF calculation to diffraction measurements of Ho^{3+} magnetic moment at high T & MC fitting of scattering function to diffraction difference between $T = 1.5$ and 200K
	...K ? (DIO)	...

Table 4.2: Iridium interaction strengths in pyrochlore iridates HIO and DIO in the literature.

exchange [93]. The two possible iridium ground states that remain are ordered, with their spins collectively aligning with or against the local trigonal axes. This may be modelled as $\mathbf{S}_{a_i^\pm} \implies S^\pm \hat{u}_i^\pm = S\hat{u}_i$ for all a_i, with $S = \{+1, -1\}$ for the spins in Ao or Ai arrangement the only remaining degree of freedom. Hence, the Hamiltonian for the inter-sublattice interaction between dysprosium spins α_j and their six neighboring iridium spins $a_i \circ \alpha_j$

reduces as

$$H_{\text{Ir-Dy}} = -J_{\text{Ir-Dy}} \sum_{\langle a_i, \alpha_j \rangle} \mathbf{S}_{a_i} \cdot \boldsymbol{\sigma}_{\alpha_j} = -\frac{1}{2} J_{\text{Ir-Dy}} \sum_{\alpha, j} \boldsymbol{\sigma}_{\alpha_j} \cdot \sum_{a_i \bigcirc \alpha_j} \mathbf{S}_{a_i}$$

$$\overset{\text{Ir Ao/Ai}}{\Longrightarrow} -S J_{\text{Ir-Dy}} \sum_{\alpha, j} \boldsymbol{\sigma}_{\alpha_j} \cdot \sum_{i \neq j} \hat{u}_i = S J_{\text{Ir-Dy}} \sum_{\alpha, j} \boldsymbol{\sigma}_{\alpha_j} \cdot \hat{u}_j$$

$$= -\frac{1}{2} \sum_{\alpha, j} \mathbf{h}_j^{\text{loc}} \cdot \boldsymbol{\sigma}_{\alpha_j} = -\frac{1}{2} h^{\text{loc}} \sum_{\alpha, j} \sigma_{\alpha_j}. \tag{4.10}$$

where we have used Eq. (4.1) to rewrite the sum of trigonal axes. With the iridium spins locked in uniform direction, the intersublattice coupling can be described in terms of local fields $\mathbf{h}_j^{\text{loc}} = h^{\text{loc}} \hat{u}_j$ of uniform strength $h^{\text{loc}} = -2S J_{\text{Ir-Dy}}$ that are directed along or against the axis $\hat{u}_j$ of the dysprosium site α_j they act on, see Fig. 4.4 [93]. Note that a plus/minus dysprosium tetrahedron $\alpha^{\pm}$ is surrounded by minus/plus iridium tetrahedra $a^{\mp}$. With a ferromagnetic intersublattice coupling $J_{\text{Ir-Dy}} > 0$, Ao/Ai iridium arrangement generates local fields favoring inwards/outwards directed central dysprosium spins, while antiferromagnetic $J_{\text{Ir-Dy}} < 0$ means that Ao/Ai ordering of the iridium spins produces fields against/along the local trigonal directions on the dysprosium sublattice.

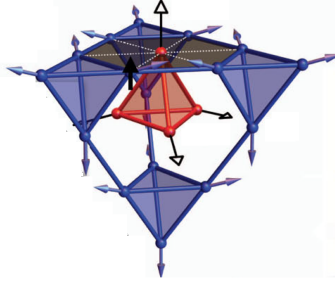Figure 4.4: Single dysprosium tetrahedron (red) and surrounding iridium sites (purple), with spins in Ao state. The intersublattice coupling then generates a local magnetic field $\mathbf{h}_j^{\text{loc}}$ (white arrowheads) acting on every dysprosium site α_j [93].

We can rewrite the total effective Hamiltonian affecting the dysprosium sublattice at energy scales well below the Ao or Ai ordering of the iridium

moments in terms of the charges defined in Eq. (4.4) as

$$H_{\text{Dy}}^{\text{eff}} = H_{\text{Dy}}^{\text{spin ice}} + H_{\text{Ir-Dy}}$$

$$\overset{\text{Ir }\underline{\text{Ao/Ai}}}{\Longrightarrow} -\frac{1}{2}J_{\text{Dy}}^{\text{eff}} \sum_{\alpha} \sum_{i,j \neq i} \sigma_{\alpha_i}\sigma_{\alpha_j} - \frac{1}{2}h^{\text{loc}} \sum_{\alpha} \sum_{j} \sigma_{\alpha_j}$$

$$= -\sum_{\pm,\alpha\pm} \left[2J_{\text{Dy}}^{\text{eff}}(Q_{\alpha\pm}^2 - 1) \pm h^{\text{loc}}Q_{\alpha\pm} \right] = \sum_{\pm,\alpha\pm} \varepsilon_{Q_{\alpha\pm}}. \qquad (4.11)$$

The corresponding energies $\varepsilon_{Q_{\alpha\pm}} = -\left[2J_{\text{Dy}}^{\text{eff}}(Q_{\alpha\pm}^2 - 1) \pm h^{\text{loc}}Q_{\alpha\pm} \right]$ per tetrahedron, also plotted in Fig. 4.5, are then given by

$$\varepsilon_{Q_{\alpha\pm}=0} = +2J_{\text{Dy}}^{\text{eff}},$$

$$\varepsilon_{Q_{\alpha\pm}=\mp 1} = -h^{\text{loc}}, \qquad\qquad \varepsilon_{Q_{\alpha\pm}=\pm 1} = +h^{\text{loc}},$$

$$\varepsilon_{Q_{\alpha\pm}=\mp 2} = -6J_{\text{Dy}}^{\text{eff}} - 2h^{\text{loc}}, \qquad \varepsilon_{Q_{\alpha\pm}=\pm 2} = -6J_{\text{Dy}}^{\text{eff}} + 2h^{\text{loc}}. \qquad (4.12)$$
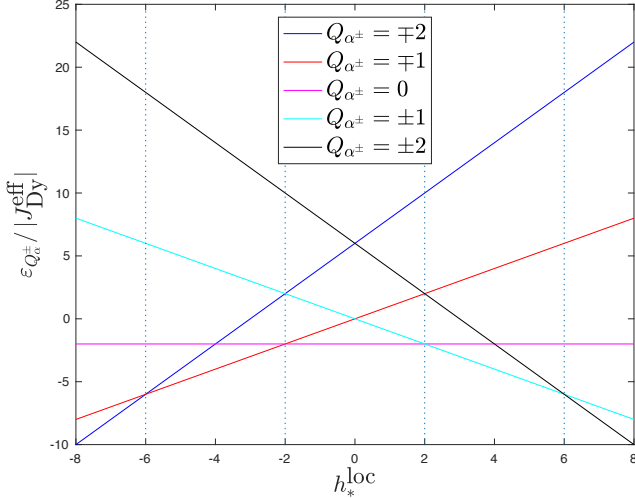
Figure 4.5: Energies per tetrahedron $\varepsilon_{Q_{\bar{\alpha}}^{\pm}}$ of Eq. (4.12), in units of $|J_{\text{Dy}}^{\text{eff}}|$ as a function of the reduced local field strength $h_*^{\text{loc}} = h^{\text{loc}}/|J_{\text{Dy}}^{\text{eff}}|$.

In this language, it is readily seen that the local fields generated by the iridium sublattice act as a chemical potential for charges [93]. Their inclusion explicitly breaks the symmetry between plus tetrahedra and minus

tetrahedra $\alpha^\pm$ that is present in ordinary pyrochlore spin ice systems. A positive h^{loc} favors the production of positive charges on positive tetrahedra and of negative charges on negative tetrahedra, while for negative-valued fields the opposite holds true. Since the system is in this way invariant under inversion h^{loc}, we focus on positive values of the reduced field strength $h^{\mathrm{loc}}_* = h^{\mathrm{loc}}/|J^{\mathrm{eff}}_{\mathrm{Dy}}|$. There are then three distinct charge phases, clearly separated by boundaries at energies $\varepsilon_0 = \varepsilon_{\pm 1}$ and $\varepsilon_{\pm 1} = \varepsilon_{\pm 2}$ [93]:

- $0 \leq h^{\mathrm{loc}}_* \leq 2$: weak local fields are insufficient to push the system away from the spin ice ground state. Here, all tetrahedra have a vanishing charge $Q_{\alpha\pm} = 0$, corresponding to canonical 2i2o ordering.

- $2 \leq h^{\mathrm{loc}}_* \leq 6$: for intermediate values the competition between the local fields and the dysprosium coupling leads the system to stabilize the monopole excitations by lowering their energy with respect ot the spin ice ground state. This results in a disordered manifold of 1i3o or 3i1o of tetrahedra that are characterized by a charge $Q_{\alpha\pm} = \pm 1$.

- $h^{\mathrm{loc}}_* > 6$: as the dominant energy scale the field strength causes the dysprosium sublattice to order into the unique ground state formed by Ao/Ai tetrahedra, with charge $Q_{\alpha\pm} = \pm 2$.

In order to quantify the degree to which the system is removed from these states we define the average charge operator

$$\bar{Q} = \frac{1}{N_{\mathrm{tet}}} \left| \sum_\alpha Q_\alpha \right| = \frac{1}{2N_{\mathrm{tet}}} \left| \sum_{\alpha,i} \sigma_{\alpha_i} \right|, \qquad (4.13)$$

where N_{tet} is the total number of tetrahedra in the pyrochlore lattice. As long as $\bar{Q}$ does not coincide with the absolute value of the allowed integer values for the charges $Q_{\alpha\pm}$, the system remains removed from full charge ordering.

We can furthermore use the polarization operator Π to gauge spin subordering within the different charge manifolds. These manifolds are defined by the condition that every tetrahedron holds a specific charge, a condition that is in general not sufficiently constraining to absolutely avoid degeneracies.

Instead there remains a large amount of freedom in the absolute spatial orientation of the spins in a tetrahedron with a given charge, which has drastic effects on the polarization. It is defined as

$$\Pi = \frac{1}{N_{\text{tet}}} \left| \sum_{\alpha,i} \boldsymbol{\sigma}_{\alpha_i} \right| = \frac{1}{N_{\text{tet}}} \left| \sum_{\alpha,i} \sigma_{\alpha_i} \hat{u}_i \right|. \tag{4.14}$$

The orientation of the spins on a tetrahedron is not uniquely specified by the charge it holds, and without secondary selection mechanisms will generally be random. Even after charge ordering, the polarization will thus generally vanish in the thermodynamic limit. On the other hand in states with ordering wavefector $q = 0$ for which all the spins on equivalent sites are directed similarly, the polarization will reach the theoretical maxima

$$\Pi_{|Q_\alpha|=2} = \frac{1}{4} \left| \sum_j \hat{u}_j \right| = 0, \tag{4.15}$$

$$\Pi^{q=0}_{|Q_\alpha|=1} = \frac{1}{4} \left| \sum_{j \neq i} \hat{u}_j - \hat{u}_i \right| = \frac{1}{2} |\hat{u}_i| = \frac{1}{2}, \tag{4.16}$$

$$\Pi^{q=0}_{|Q_\alpha|=0} = \frac{1}{4} \left| (\hat{u}_i + \hat{u}_{\text{mod}(i+1,4)}) - (\hat{u}_{\text{mod}(i+2,4)} + \hat{u}_{\text{mod}(i+3,4)}) \right| = \frac{1}{\sqrt{3}}. \tag{4.17}$$

4.4 Small angle deviation

(a) Iridium site a_i and its six iridium nearest neighbors $a_j^\pm$ with $j \neq i$.

(b) Iridium site a_i and its six surrounding dysprosium sites $\alpha_j \circ a_i$.
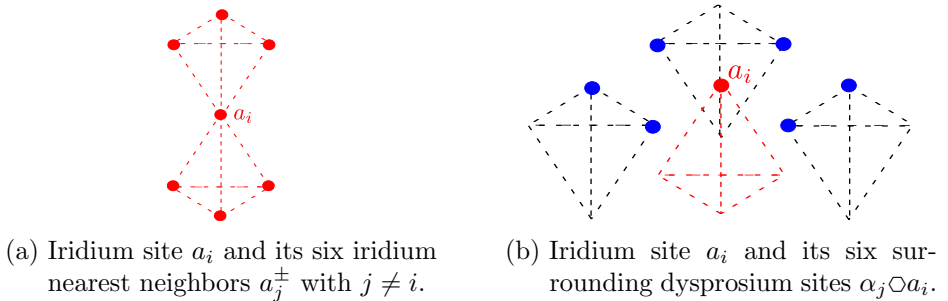
Figure 4.6: The nearest surrounding sites of an iridium site a_i.

In the previous section we have laid out the behavior of the system of interpenetrating iridium and dysprosium pyrochlore lattices on the assumption that the interactions in the former are far dominant over those in the latter, and at lower energy scales we may project into the corresponding iridium ground state manifold to probe the physics playing out on the dysprosium sites. In contrast, we will here consider possible deviations in the iridium collective ordering into the Ao or Ai state due to competition between the DM interaction and the dysprosium couplings when these are of similar order.

Focusing on interactions within the iridium sublattice, the single-site Hamiltonian is simply

$$
\begin{aligned}
H_{\mathrm{Ir},a_i} &= -J_{\mathrm{Ir}}\mathbf{S}_{a_i} \cdot \sum_{\pm} \sum_{j \neq i} \mathbf{S}_{a_j^\pm} - D_{\mathrm{Ir}} \sum_{\pm} \sum_{j \neq i} \mathbf{D}_{ij} \cdot (\mathbf{S}_{a_i} \times \mathbf{S}_{a_j^\pm}) \\
&= -\mathbf{S}_{a_i} \cdot \sum_{\pm} \sum_{j \neq i} \left(J_{\mathrm{Ir}}\, \mathbf{S}_{a_j^\pm} + \frac{3}{2\sqrt{2}} D_{\mathrm{Ir}} \left[\hat{u}_i (\mathbf{S}_{a_j^\pm} \cdot \hat{u}_j) - \hat{u}_j (\mathbf{S}_{a_j^\pm} \cdot \hat{u}_i) \right] \right) \\
&= -\mathbf{S}_{a_i} \cdot \boldsymbol{\mathcal{H}}_{a_i},
\end{aligned}
\tag{4.18}
$$

where $\boldsymbol{\mathcal{H}}_{a_i}$ can be interpreted as an effective field generated by the six nearest neighbors $a_j^\pm$ with $j \neq i$ that is acting on the central spin a_i, see Fig. 4.6a. Assuming that the iridium sublattice is ordered in the Ao or Ai state, so $\mathbf{S}_{a_j^\pm} = S\,\hat{u}_j$ for all the sites j in the thetrahedra $a^\pm$, yields

$$
\begin{aligned}
\boldsymbol{\mathcal{H}}_{a_i} &\stackrel{\mathrm{Ir\ Ao/Ai}}{\Longrightarrow} 2S \sum_{j \neq i} \left(J_{\mathrm{Ir}} \hat{u}_j + \frac{3}{2\sqrt{2}} D_{\mathrm{Ir}} \left[\hat{u}_i (\hat{u}_j \cdot \hat{u}_j) - \hat{u}_j (\hat{u}_j \cdot \hat{u}_i) \right] \right) \\
&= -2S \left(J_{\mathrm{Ir}} - 2\sqrt{2} D_{\mathrm{Ir}} \right) \hat{u}_i = -J_{\mathrm{Ir}}^{\mathrm{eff}}\, \mathbf{S}_{a_i},
\end{aligned}
\tag{4.19}
$$

by Eq. (4.1). Of course, this result may be checked explicitly in a particular reference frame, for example by means of Eqs. (4.37)-(4.38). Keeping in mind that the exchange interactions are AFM, $J_{\mathrm{Ir}} < 0$, and the DM interactions are direct, $D_{\mathrm{Ir}} > 0$, we see that $J_{\mathrm{Ir}}^{\mathrm{eff}} = 2(J_{\mathrm{Ir}} - 2\sqrt{2} D_{\mathrm{Ir}}) < 0$ and thus that the effective field points precisely along the central spin.

We are now interested in the effect on this energy of a deviation by a small angle $\theta \ll 1$, indicated by a prime, away from the ordering along the local

direction,

$$\mathbf{S}_{a_i} \to \mathbf{S}'_{a_i} = \hat{r} \sin\theta + \mathbf{S}_{a_i} \cos\theta \approx \theta\,\hat{r} + \left(1 - \frac{\theta^2}{2}\right)\mathbf{S}_{a_i}. \qquad (4.20)$$

With this result we find the dot product $\mathbf{S}_{a_i} \cdot \mathbf{S}'_{a_i} = 1 - \theta^2/2$, indepedent of the polar coordinate $\hat{r} \perp \mathbf{S}_{a_i}$ in the plane perpendicular to the unperturbed spin. Hence, we have that

$$H_{\mathrm{Ir},a_i} \overset{\mathrm{Ir\ Ao'/Ai'}}{\Longrightarrow} E_{\mathrm{Ir},a_i}(\theta) = -\mathbf{S}'_{a_i} \cdot \boldsymbol{\mathcal{H}}_{a_i} = J^{\mathrm{eff}}_{\mathrm{Ir}} \mathbf{S}'_{a_i} \cdot \mathbf{S}_{a_i}$$

$$\approx 2\left(J_{\mathrm{Ir}} - 2\sqrt{2}D_{\mathrm{Ir}}\right)\left(1 - \frac{\theta^2}{2}\right) = E^{\theta=0}_{\mathrm{Ir},a_i} - \frac{1}{2}J^{\mathrm{eff}}_{\mathrm{Ir}}\theta^2, \qquad (4.21)$$

with $E^{\theta=0}_{\mathrm{Ir},a_i} = J^{\mathrm{eff}}_{\mathrm{Ir}} = 2(J_{\mathrm{Ir}} - 2\sqrt{2}D_{\mathrm{Ir}}) < 0$.

The inter-sublattice interaction between a single iridium spin at site i in the tetrahedron a and its six surrounding dysprosium spins $\alpha_j \bigcirc a_i$, see Fig. 4.6b, is of the form

$$H_{\mathrm{Ir\text{-}Dy},a_i} = -J_{\mathrm{Ir\text{-}Dy}}\mathbf{S}_{a_i} \cdot \sum_{\alpha_j \bigcirc a_i} \boldsymbol{\sigma}_{\alpha_j} = -J_{\mathrm{Ir\text{-}Dy}}\mathbf{S}_{a_i} \cdot \boldsymbol{\eta}_{a_i}$$

$$= -J_{\mathrm{Ir\text{-}Dy}}\mathbf{S}_{a_i} \cdot \left(\boldsymbol{\eta}_{\parallel,a_i} + \boldsymbol{\eta}_{\perp,a_i}\right), \qquad (4.22)$$

where we have split up the effective field $\boldsymbol{\eta}_{\alpha_i}$ generated by the dysprosium moments into components parallel $\boldsymbol{\eta}_{\parallel,a_i} \parallel \mathbf{S}_{a_i}$ and perpendicular $\boldsymbol{\eta}_{\perp,a_i} \perp \mathbf{S}_{a_i}$ to the iridium spin that sits in it. We have accordingly defined

$$\boldsymbol{\eta}_{a_i} = \sum_{\alpha_j \bigcirc a_i} \boldsymbol{\sigma}_{\alpha_j}, \qquad \boldsymbol{\eta}_{\parallel,a_i} = \eta_{\parallel,a_i}\mathbf{S}_{a_i}, \qquad \boldsymbol{\eta}_{\perp,a_i} = \boldsymbol{\eta}_{a_i} - \boldsymbol{\eta}_{\parallel,a_i}, \quad (4.23)$$

which implies that the parallel component is given by

$$\eta_{\parallel,a_i} = \mathbf{S}_{a_i} \cdot \boldsymbol{\eta}_{a_i} = \mathbf{S}_{a_i} \cdot \sum_{\alpha_j \bigcirc a_i} \boldsymbol{\sigma}_{\alpha_j} = S \sum_{\alpha_j \bigcirc a_i} \sigma_{\alpha_j} \hat{u}_i \cdot \hat{u}_j = -\frac{S}{3} \sum_{\alpha_j \bigcirc a_i} \sigma_{\alpha_j}. \qquad (4.24)$$

As a result, we find that the parallel field acting on an iridium site is directed along the original spin if it is surrounded by dysprosium spins that

in majority have the opposite relation to their local axis. For example, if the iridium sublattice orders in Ai fashion ($S = -1$) and all the dysprosium spins neighboring the site a_i follow their axes $\hat{u}_j$ so that $\sigma_{\alpha_j} = +1$ for all $\alpha_j \circ a_i$, we find a positive parallel component $\eta_{\parallel,a_i} = +2$ that is directed along $\mathbf{S}_{a_i}$.

The local trigonal axis of an iridium site is orthogonal to the plane containing the hexagon of nearest dysprosium spins. Again assuming iridium Ao or Ai ordering, we can then similarly investigate the effect of the small wiggle $\mathbf{S}_{a_i} \to \mathbf{S}'_{a_i}$ on the inter-sublattice interaction. We find

$$
\begin{aligned}
H_{\text{Ir-Dy},a_i} &\overset{\text{Ir Ao'/Ai}'}{\Longrightarrow} E_{\text{Ir-Dy},a_i}(\theta) = -J_{\text{Ir-Dy}} \mathbf{S}'_{a_i} \cdot \boldsymbol{\eta}_{a_i} \\
&\approx -J_{\text{Ir-Dy}} \left(\theta\,\hat{r} + \left(1 - \frac{\theta^2}{2} \right) \mathbf{S}_{a_i} \right) \cdot (\eta_{\parallel,a_i} \mathbf{S}_{a_i} + \boldsymbol{\eta}_{\perp,a_i}) \\
&= E^{\theta=0}_{\text{Ir-Dy},a_i} - J_{\text{Ir-Dy}} \left(\hat{r} \cdot \boldsymbol{\eta}_{\perp,a_i}\,\theta - \frac{1}{2} \eta_{\parallel,a_i} \theta^2 \right),
\end{aligned}
\tag{4.25}
$$

where $E^{\theta=0}_{\text{Ir-Dy},a_i} = -J_{\text{Ir-Dy}} \eta_{\parallel,a_i}$ is the energy corresponding to an unperturbed spin that was treated in Sec. 4.3 [93]. Indeed, extending this contribution over the entire lattice we can cast it into the form of a sum over the dysprosium spins only,

$$
\begin{aligned}
H_{\text{Ir-Dy}} &\overset{\text{Ir Ao/Ai}}{\Longrightarrow} \frac{1}{2} \sum_{a,i} E^{\theta=0}_{\text{Ir-Dy},a_i} = -\frac{1}{2} J_{\text{Ir-Dy}} \sum_{a,i} \eta_{\parallel,a_i} \\
&= S J_{\text{Ir-Dy}} \sum_{\alpha,j} \sigma_{\alpha_j} = -\frac{1}{2} h^{\text{loc}} \sum_{\alpha,j} \sigma_{\alpha_j}
\end{aligned}
\tag{4.26}
$$

for $h^{\text{loc}} = -2 S J_{\text{Ir-Dy}}$, so that we recuperate the result previously obtained in Eq. (4.10).

Putting together Eq. (4.21) and Eq. (4.25), the total effective Hamiltonian acting on a single iridium spin at a small angle deviation from the Ao or Ai state is

$$
\begin{aligned}
H^{\text{eff}}_{\text{Ir},a_i} &= H_{\text{Ir},a_i} + H_{\text{Ir-Dy},a_i} \\
&\overset{\text{Ir Ao'/Ai}'}{\Longrightarrow} E^{\text{eff}}_{\text{Ir},a_i}(\theta) = E_{\text{Ir},a_i}(\theta) + E_{\text{Ir-Dy},a_i}(\theta) \\
&= E^{\text{eff},\theta=0}_{\text{Ir},a_i} - J_{\text{Ir-Dy}}\,\hat{r} \cdot \boldsymbol{\eta}_{\perp,a_i}\,\theta - \frac{1}{2} \left(J^{\text{eff}}_{\text{Ir}} - J_{\text{Ir-Dy}} \eta_{\parallel,a_i} \right) \theta^2,
\end{aligned}
\tag{4.27}
$$

where $E_{\text{Ir},a_i}^{\text{eff},\theta=0} = E_{\text{Ir},a_i}^{\theta=0} + E_{\text{Ir-Dy},a_i}^{\theta=0} = J_{\text{Ir}}^{\text{eff}} - J_{\text{Ir-Dy}}\eta_{\parallel,a_i}$. We minimize the energy function $E_{\text{Ir},a_i}^{\text{eff}}(\theta)$ with respect to θ. The critical point satisfies $\partial_\theta E_{\text{Ir},a_i}^{\text{eff}}(\theta)|_{\theta=\theta_0} = 0$, with the minimizing angle given by

$$\theta_0 = -\frac{J_{\text{Ir-Dy}} \; \hat{r} \cdot \boldsymbol{\eta}_{\perp,a_i}}{J_{\text{Ir}}^{\text{eff}} - J_{\text{Ir-Dy}}\eta_{\parallel,a_i}}. \tag{4.28}$$

Since it holds that $\partial_\theta^2 E_{\text{Ir},a_i}^{\text{eff}}(\theta)|_{\theta=\theta_0} = -J_{\text{Ir}}^{\text{eff}} - J_{\text{Ir-Dy}}\eta_{\parallel,a_i} > 0$, this is indeed a minimum of the energy. By back substitution we find that at this minimal point the energy function becomes

$$\begin{aligned}
E_{\text{Ir},a_i}^{\text{eff}}(\theta_0) &= E_{\text{Ir},a_i}^{\text{eff},\theta=0} + \frac{J_{\text{Ir-Dy}}^2 \left(\hat{r} \cdot \boldsymbol{\eta}_{\perp,a_i}\right)^2}{2\left(J_{\text{Ir}}^{\text{eff}} - J_{\text{Ir-Dy}}\eta_{\parallel,a_i}\right)} \\
&= -J_{\text{Ir-Dy}}\eta_{\parallel,a_i} + J_{\text{Ir-Dy}}^\perp \eta_{\perp,a_i}^2 + \text{const.}
\end{aligned} \tag{4.29}$$

At first approximation we assume that iridium perturbations are mutually independent, ignoring the possibility of correlations between the different deviations of pairs of spins. We are then at liberty to choose $\hat{r}$ to be co-directional with the perpendicular field, $\hat{r} \parallel \boldsymbol{\eta}_{\perp,a_i}$, in order to minimize the (negative) energy contribution. Furthermore, we can ignore the constant contribution deriving from the unperturbed Ao / Ai iridium state. Assuming that $|J_{\text{Ir}}^{\text{eff}}| \gg |J_{\text{Ir-Dy}}|$, the fraction in the perpendicular coupling simplifies,

$$J_{\text{Ir-Dy}}^\perp = \frac{J_{\text{Ir-Dy}}^2}{2\left(J_{\text{Ir}}^{\text{eff}} - J_{\text{Ir-Dy}}\eta_{\parallel,a_i}\right)} \approx \frac{J_{\text{Ir-Dy}}^2}{2J_{\text{Ir}}^{\text{eff}}} < 0. \tag{4.30}$$

Note that the limit of perpendicular effective coupling to zero, $J_{\text{Ir-Dy}}^\perp \to 0$, represents the static model in which the iridium spins are entirely locked into Ao or Ai position and thus contribute only by the effect of their collective parallel effective local magnetic field component on the dysprosium sublattice [93]. The perturbative effect of a small angle deviation is entirely encapsulated in the perpendicular field, whose squared contribution can be

rewritten in terms of sums of different Ising pairings on the hexagon,

$$\eta_{\perp,a_i}^2 = \eta_{a_i}^2 - \eta_{\parallel,a_i}^2 = \left(\sum_{\alpha_j \circ a_i} \boldsymbol{\sigma}_{\alpha_j} \right)^2 - \left(\sum_{\alpha_j \circ a_i} \boldsymbol{\sigma}_{\alpha_j} \cdot \mathbf{S}_{a_i} \right)^2$$

$$= \frac{8}{9} \left(12 + 2 \sum_{(\alpha_j \leftrightarrow \beta_j) \circ a_i} \sigma_{\alpha_j} \sigma_{\beta_j} \right.$$

$$\left. - \sum_{\langle \alpha_j, \beta_k \rangle \circ a_i} \sigma_{\alpha_j} \sigma_{\beta_k} - \sum_{\langle\langle \alpha_j, \beta_k \rangle\rangle \circ a_i} \sigma_{\alpha_j} \sigma_{\beta_k} \right). \tag{4.31}$$

Here, $(\alpha_j \leftrightarrow \beta_j) \circ a_i$ implies pairings of dysprosium spins on opposite ends of the hexagon centered on iridium site a_i. Similarly, the notations $\langle \alpha_j, \beta_k \rangle \circ a_i$ and $\langle\langle \alpha_j, \beta_k \rangle\rangle \circ a_i$ mean nearest neighbor and next nearest neighbor pairings on the same hexagon. It is then apparent that the energy is lowered by maximizing the perpendicular field. To this end, spins on opposite sites of a hexagon should point in the same direction. On the other hand, in pairings of adjacent and next-nearest neighboring spins one moment should be directed into and the other out of their tetrahedra.

What we have found now is the optimal approximated contribution to the overall energy of a single iridium spin that is slightly skewed away from its unperturbed Ao or Ai direction. We then extend Eq. (4.29) to hold equally for a larger number of iridium sites in the interpenetrated pyrochlore lattice, even though the correlations between two tilted iridium spins will lead to additional terms of order θ and θ^2 neglected here that will depend on polar coordinate $\hat{r}$ of the symmetry breaking. This effect will compete with the simple-minded assumption of codirectionality with the perpendicular effective dysprosium field, $\hat{r}||\boldsymbol{\eta}_{\perp,a_i}$. However, the current assumption should hold reasonably well at least in the regime of a low density of deviating iridium spins.

The assumptions made in this section are especially fruitful for Monte Carlo simulation, since they cast the irididium contributions to the energy into the form of a potential independent of their spin state that is a small optimal angle $\theta_0 \ll 1$ away from collective local direction ordering. We have thus effectively projected them out of our model description, leaving us with

a simulation that is Ising-type. A flip of a dysprosium spin on the site α_i causes an energy difference

$$\Delta E_{\text{Dy}}(\Delta\sigma_{\alpha_i}) = -J_{\text{Dy}}^{\text{eff}} \Delta\sigma_{\alpha_i} \sum_{\pm} \sum_{j\neq i} \sigma_{\alpha_j} \tag{4.32}$$

in the spin ice-like contribution of the pure dysprosium model that is unaffected by the small angle θ_0 deviation of the iridium spins. Differently, substituting Eq. (4.24) and Eq. (4.31) into Eq. (4.29) we find that the iridium potential difference on one of the six neighboring sites a_j caused by a dysprosium spin flip on site α_i is given by

$$
\begin{aligned}
\Delta E_{\text{Ir},a_j}^{\text{eff}}(\theta_0; \Delta\sigma_{\alpha_i}) &= -J_{\text{Ir-Dy}}\Delta\eta_{\parallel,a_j} + J_{\text{Ir-Dy}}^{\perp}\Delta\eta_{\perp,a_j}^2 \\
&= \left[-\frac{1}{6}h^{\text{loc}} + \frac{8}{9}J_{\text{Ir-Dy}}^{\perp} \left(2 \sum_{(\beta_i\to\alpha_i)\circ a_j} \sigma_{\beta_i} \right.\right. \\
&\qquad \left.\left. - \sum_{(\beta_k\sim\alpha_i)\circ a_j} \sigma_{\beta_k} - \sum_{(\beta_k\sim\sim\alpha_i)\circ a_j} \sigma_{\beta_k} \right) \right] \Delta\sigma_{\alpha_i}, \tag{4.33}
\end{aligned}
$$

where $(\beta_i \to \alpha_i)\circ a_j$ implies that we target the site β_i opposite of α_i on hexagon a_j and $(\beta_k \sim \alpha_i)\circ a_j$ and $(\beta_k \sim\sim \alpha_i)\circ a_j$ respectively indicate sums over the nearest and next nearest neighbors of α_i on a_j. We have taken the liberty of rewriting the parallel term in terms of the iridium-induced local field strength on a dysprosium atom by virtue of their duality in the unperturbed case $\theta = 0$, a restatement of Eq. (4.26).

4.5 Exact maximization of $\eta_\perp^2$ on finite lattice segments

In order to put our simulations on a sounder theoretical footing we have investigated the configurations within some specific manifolds that maximize the overall value of the perpendicular magnetic field on various finite lattice segments by a brute-force computerized approach. For each of the 2^N configurations permissible on a plaquette of N dysprosium Ising-like spins we

calculate the quantities

$$\eta_\parallel = \frac{1}{2} \sum_{a,j} \eta_{\parallel,a_j}, \qquad\qquad \eta_\perp^2 = \frac{1}{2} \sum_{a,j} \left(\eta_{\perp,a_j}^2 \right), \qquad (4.34)$$

where we sum over all the hexagonal dysprosium plaquettes or, equivalently, their central iridium sites a_j.

4.5.1 hexagon plaquette

First of all, we look at the elementary hexagon formed by the six dysprosium sites $\alpha_j \circ a_i$ contributing to the field acting on a iridium site a_i, see Fig. 4.6b. Modulo a global spin flip and rotations of the hexagon there are eight inequivalent configurations to consider. These are classified according to their contribution to $\eta_\parallel$ and $\eta_\perp^2$ in Table 4.3.

	$\eta_\parallel = 0$	$\eta_\parallel = 2/3$	$\eta_\parallel = 4/3$	$\eta_\parallel = 2$
$\eta_\perp^2 = 0$	(+ + + - - -), (+ - + - + -)	-	-	(+ + + + + +)
$\eta_\perp^2 = 32/9$	-	(+ + + + - -), (+ + + - + -)	(+ + + + + -)	-
$\eta_\perp^2 = 96/9$	(+ + - + - -)	-	-	-
$\eta_\perp^2 = 128/9$	-	(+ + - + + -)	-	-

Table 4.3: Parallel magnetic field and perpendicular magnetic field squared induced by different configurations, denoted by their values of Ising variable σ_{α_j} for all the six sites α_j on the hexagon.

We provided analytical formulas for the parallel and perpendicular fields on a surrounding hexagon in Eq. (4.24) and Eq. (4.31). Since opposite sites on the hexagon have coinciding local trigonal directions, the spins inhabiting them should point in the same direction to result in a postive contribution to $\eta_\perp^2$. Furthermore, due to the tetrahedron's high symmetry the sum of any three distinct local axes is antiparallel to the fourth, see Eq. (4.1). This engenders an effective preference for a spin to surround itself by pairs of spins pointing in the opposite direction if the aim is to increase the perpendicular field.

From Table 4.3 it is clear that the symmetric 2o1i2o1i-loop around the hexagon, shown in Fig. 4.7, is the configuration that is most effective at

using the described rules to maximize the perpendicular field. It is as well suited as the runner-up 2o1i1o2i-loop to benefitting from the second and third variable terms in Eq. (4.31), which both have no spins surrounded by pairs pointing in the same direction but do have two locations where spins are positioned in between pairs pointing in the opposite direction. However, all of the spins in the 2o1i2o1i formation point in the same direction as their opposite number, maximising the first variable term of Eq. (4.31), which is different for the 2o1i1o2i-loop.
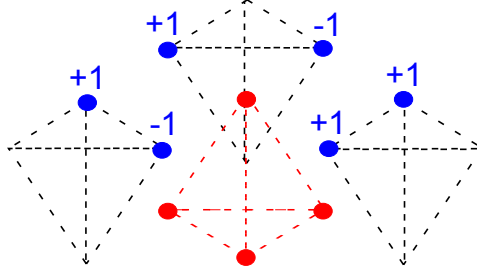

Figure 4.7: The symmetric 2o1i2o1i-loop has the highest contribution to the perpendicular field $\eta_\perp^2$ of the configurations permissible on a hexagon.

4.5.2 supertetrahedron plaquette

We then extend this analysis to the supertetrahedron formed by a single iridium tetrahedron and its dysprosium neighbors. This plaquette has an overall ground state that is a straightforward tiling of the optimal symmetric 2o1i2o1i-loop on each of its four constituent hexagons, see Fig. 4.8a. As such, its perpendicular contribution is given by $\eta_\perp^2 = 4 \cdot 128/9 = 512/9$. The entire pyrochlore lattice may be covered by a simple repitition of this fundamental supertetrahedron configuration, leading to a unique 2i2o state that preserves the original translation symmetry. This is the $q = 0$ charge 0 state.

Including only tetrahedra with charge ∓ 1 or ± 1 rules out lattice coverings composed of the optimal supertetrahedron configuration, as that setup would necessarily contain both 3i1o and 1i3o tehtrahedra. Allowing only tetrahedra of the same type, with charge ± 1 we find that the configuration in Fig. (4.8b) is preferred. Besides three optimal hexagons it also contains a single loop with a vanishing perpendicular contribution, resulting in $\eta_\perp^2 = 3 \cdot 128/9 +$

$1 \cdot 0 = 128/3$. This spin configuration is trivially extended, giving a strong hint that this might be the fundamental spin unit of the lowest energy state of the submanifold on the infinite lattice.
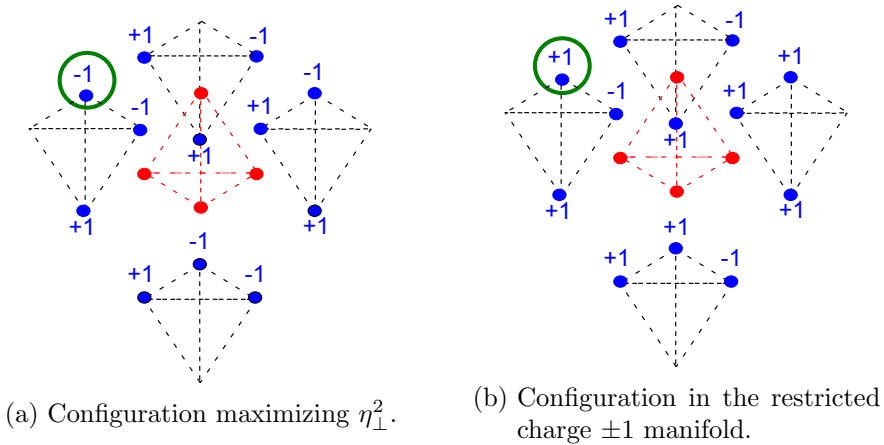

(a) Configuration maximizing $\eta_\perp^2$.

(b) Configuration in the restricted charge ± 1 manifold.

Figure 4.8: Supertetrahedron plaquette configurations maximizing $\eta_\perp^2$.

4.5.3 Triangle of supertetrahedra

Lastly we have looked at a structure consisting of three supertetrahedra in a triangular arrangement. Unconditional seeding of spins indeed finds that the simple periodic extension of the supertetrahedron optimal spin structure, containing only optimal hexagons, is preferred, with $\eta_\perp^2 = 12 \cdot 128/9 = 512/3$.

Restricting to the manifold of tetrahedra with charges ∓ 1 or ± 1, we find that on this plaquette can exist coverings with a cumulative perpendicular magnetic field squared of $\eta_\perp^2 = 1408/9$, an example of which can be found in Fig. 4.9a. Again, these structures are highly aperiodic and how they could be extended to cover the entire lattice is unclear. One feature that all the optimal spin structures on this plaquette share is that the spins on one of the central dysprosium triangular plane, e.g. those at the lower tips of the top layer of the dysprosium tetrahedra, are all directed similarly. This can be explained by realizing that every tetrahedron in the manifold has at least a single spin of both sign. By Eq. (4.31) it is then advantageous to place all such spins on equivalent sites within their tetrahedron

so that spins at opposite hexagonal ends have the same direction. The remaining three spins of each tetrahedron then order to cover their kagome plane with the optimal 2o1i2o1i-loop hexagons, while the spins of the tetrahedra of the lower kagome plane adapt to optimize the hexagons connecting the layers. This mechanism is not sufficiently constraining to be insensitive to finite-size effects. Indeed, covering the infinite lattice according to these rules results in the spin substructure Fig. 4.9b of three optimal and one zero-contribution hexagon per iridium tetrahedron, which yields a lower perpendicular field value $\eta_\perp^2 = 3 \cdot 128/3 = 128$. Respecting the original pyrochlore translation symmetry, this long-range ordered spin structure is known as the $q = 0$ charge ± 1 state. In further support of its putative status as lowest energy state of the submanifold on the extended lattice, we find that its commensurate substructure is also the lowest energy configuration on our finite plaquette if we demand that only charge ± 1 tetrahedra are included.

(a) Optimal configuration.

(b) Optimal configuration in the restricted charge ± 1 manifold.

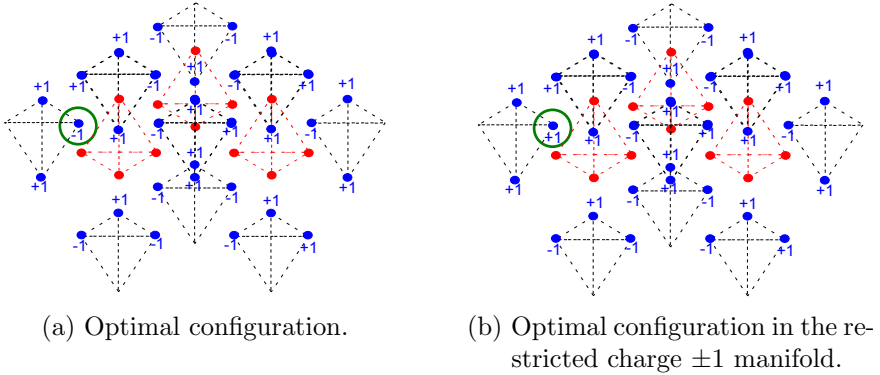Figure 4.9: Configurations on the triangle of supertetrahedra that maximize $\eta_\perp^2$.

4.6 Small angle deviation effective Monte Carlo: results

We wish to understand how a small-angle deviation from the Ao or Ai state, characterized by $\mathbf{S}_{a_i} = S\hat{u}_i$ for all a_i with $S \in \{+1, -1\}$, on the iridium sublattice affects the ordering of the dysprosium Ising-like spins. To this

end we subject the common spin ice model Eq. (4.2) on the dysprosium sublattice, supplemented with the effects of the inter-sublattice interaction, to Monte Carlo simulation. Acceptances of attempted moves are determined by the Metropolis algorithm. The relevant Boltzmann weight for a flip of the dysprosium spin at site α_i depends on the total energy difference

$$\Delta E_{\text{Dy}}^{\text{eff}}(\Delta\sigma_{\alpha_i}) = \Delta E_{\text{Dy}}(\Delta\sigma_{\alpha_i}) + \sum_{a_j \bigcirc \alpha_i} \Delta E_{\text{Ir},a_j}^{\text{eff}}(\theta_0; \Delta\sigma_{\alpha_i})$$

$$= -\left[h^{\text{loc}} + \left(J_{\text{Dy}}^{\text{eff}} + \frac{16}{9} J_{\text{Ir-Dy}}^{\perp} \right) \sum_{\pm} \sum_{j \neq i} \sigma_{\alpha_j^{\pm}} \right.$$

$$\left. + \frac{8}{9} J_{\text{Ir-Dy}}^{\perp} \left(\sum_{\beta_{j \neq i} \sim\sim \alpha_i} \sigma_{\beta_j} - 2 \sum_{\beta_i \sim\sim\sim \alpha_i} \sigma_{\beta_i} \right) \right] \Delta\sigma_{\alpha_i},$$

$$(4.35)$$

from Eq. (4.32) and Eq. (4.33). For the reader's convenience, we repeat here the definitions of the couplings that appear:

$$J_{\text{Dy}}^{\text{eff}} = -\frac{J_{\text{Dy}}}{3}, \qquad J_{\text{Ir-Dy}}^{\perp} \approx \frac{J_{\text{Ir-Dy}}^2}{2J_{\text{Ir}}^{\text{eff}}} = \frac{J_{\text{Ir-Dy}}^2}{2(J_{\text{Ir}} - 2\sqrt{2}D_{\text{Ir}})},$$

$$h^{\text{loc}} = -2S J_{\text{Ir-Dy}}, \qquad h_*^{\text{loc}} = \frac{h^{\text{loc}}}{|J_{\text{Dy}}^{\text{eff}}|} = -6S \frac{J_{\text{Ir-Dy}}}{|J_{\text{Dy}}|}.$$

Simulations were performed at fundamental parameter values

$$J_{\text{Dy}} = 4.5\text{K}, \qquad D_{\text{Ir}} = 50\text{K}, \qquad J_{\text{Ir}} = -10 D_{\text{Ir}} = -500\text{K}, \qquad (4.36)$$

along the lines indicated in [93], at different intersublattice couplings $J_{\text{Ir-Dy}} > 0$. With the choice $S = -1$, all generated local fields acting on the dysprosium sites are positive, $h^{\text{loc}} > 0$, and favor the Ao state with all spins pointing out of plus tetrahedra. For $J_{\text{Ir-Dy}}^{\perp}$ we start with the natural value resulting from the small-angle expansion definition, and then multiply it by a factor 0, 10, 100 or 1000 to magnify its effects. We present our results in a series of plots that depict the behavior of a series of instructive observables that give us insight into the physics playing out in the interpenetrated pyrochlore lattice upon lowering the temperature. Among these are the energy per spin,

heat capacity $C_V = \langle E \rangle^2 - \langle E^2 \rangle / k_{\mathrm{B}} T^2$ and average charge and polarization as defined in Eqs. (4.13)-(4.14). In the energy plots we have also shown some reference lines that correspond to the ordered $Q_{\alpha\pm} = 0$ (dotted line) and $q = 0$ ordered charge $Q_{\alpha\pm} = \pm 1$ (continuous line) states preferred by the perpendicular coupling.

It is important to remark that it has has proved difficult to completely prevent the effects of spin freezing in our simulations. Irrespective of the parameter set taken, at some (low) temperature the spins lock into position and computationally expensive non-local update mechanisms would be needed to preserve predictive power. We have attempted to circumvent such complications by tracking the number of accepted manipulations per spin. Judging from the the way it falls off at lower temperatures, for all parameter values the data is relatively trustworthy at least for significantly lower temperatures than those at which the interesting physics play out.

4.6.1 $h_*^{\mathsf{loc}} = 2$ — boundary of $J_{\mathsf{Ir\text{-}Dy}}^{\perp} = 0$ charge 0 and charge ± 1 selection regimes

First of all we aim to study the boundary of the charge 0 and charge ± 1 selection regimes that exist for $J_{\mathrm{Ir\text{-}Dy}}^{\perp} = 0$ at dimensionless local field strength $h_*^{\mathrm{loc}} = 2$, corresponding to intersublattice coupling $J_{\mathrm{Ir\text{-}Dy}} = 1.5K$ for parameter values Eq. (4.36) that give a natural perpendicular coupling $J_{\mathrm{Ir\text{-}Dy}}^{\perp} \approx -0.001$ with optimal deviation angle $\theta_0 \approx 0.002\eta_{\perp,a_i}$ of the iridium spin at a_i. For low perpendicular couplings there is excellent agreement with Lefrancois (black continuous line) [93] in the charge average plot. For higher values of $J_{\mathrm{Ir\text{-}Dy}}^{\perp}$ we start finding that the energy starts coinciding with the 2o2i dotted line, and the polarization goes towards the $1/\sqrt{3} \approx 0.57$ value predicted for the ordered $q = 0$ state in Eq. (4.15). The seemingly discontinuous behavior of the energy, polarization and charge average is accompanied by very sharp peaks in the heat capacity.

4.6.2 $h_*^{\mathsf{loc}} = 6$ — boundary of $J_{\mathsf{Ir\text{-}Dy}}^{\perp} = 0$ charge ± 1 and charge ± 2 selection regimes

We then turn our attention to the boundary of the charge ± 1 and charge ± 2 selection regimes that exist for $J_{\mathrm{Ir\text{-}Dy}}^{\perp} = 0$ at dimensionless local field
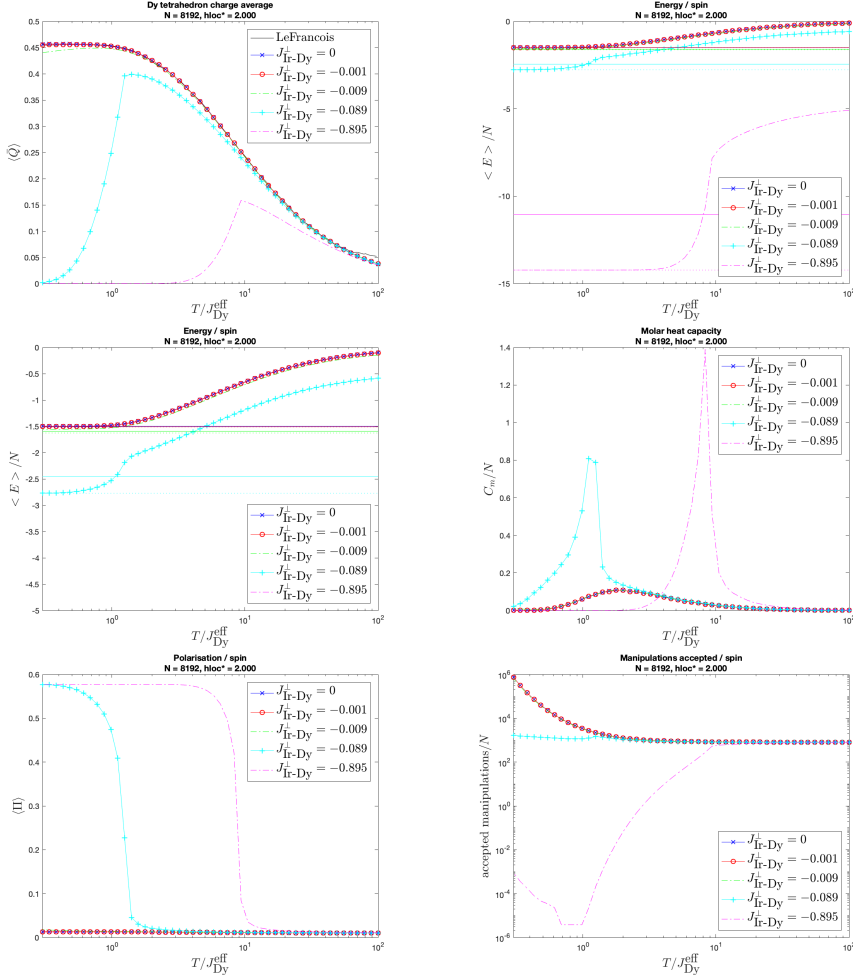
Figure 4.10: Computed observable curves for $h_*^{\text{loc}} = 2$.

strength $h_*^{\text{loc}} = 6$, corresponding to intersublattice coupling $J_{\text{Ir-Dy}} = 9K$ for parameter values Eq. (4.36). For low perpendicular couplings there is excellent agreement with Lefrancois [93] in the charge average plot (black continuous line). Notably, even at natural value (red line, $J_{\text{Ir-Dy}}^{\perp} \approx -0.008$ with a deviation angle $\theta_0 \approx 0.014\eta_{\perp,a_i}$) there is significant deviation at low T. This is due to a large preference of the perpendicular coupling for the

$Q_{\alpha\pm} = \pm 1$ state over the $Q_{\alpha\pm} = \pm 2$ state as ultimately deriving from Table 4.3, which leads to a lower charge average. Except for the largest values of $J^{\perp}_{\text{Ir-Dy}}$, the ordered 3o1i manifold is thus preferred, and energies tend to the predicted continuous reference lines. In particular the system selects the $q = 0$ charge ± 1 state, with a theoretical polarization of $1/2 = 0.5$ that is indeed tended to. For the largest value (pink lines) the perpendicular coupling becomes the dominant energy scale of in the system, leading again to the selection of the 2i2o state with vanishing average charge and a polarization of $1/\sqrt{3} \approx 0.57$. Again, all ordering transitions seem to be first order phase transitions judging by the discontinuities in the energy, polarization and charge average and the sharpness of the corresponding heat capacity peaks.

4.6.3 $h^{\text{loc}}_* = 4.5$ — deep inside $J^{\perp}_{\text{Ir-Dy}} = 0$ charge ± 1 selection regime

Finally, we have run simulations for $J_{\text{Ir-Dy}} = 6.75K$, corresponding to $h^{\text{loc}}_* = 4.5$, deep inside the the regime where the highly degenerate charge ± 1 manifold has the lowest energy for $J^{\perp}_{\text{Ir-Dy}} = 0$. It is worth noting that Lefrancois predicts such values to accurately describe the interactions in holmium iridate $\text{Ho}_2\text{Ir}_2\text{O}_7$, see Table 4.2 [93]. This gives a corresponding natural perpendicular coupling of $J^{\text{eff}}_{\text{Ir-Dy}} \approx -0.005$ for a deviation angle $\theta_0 \approx 0.011 \eta_{\perp, a_i}$ of the iridium spin at a_i. Significant deviations from purely parallel fields start developing when the perpendicular coupling is ten times increased (green line), for which the charge average $\bar{Q}$ no longer shows an overshoot but instead monotonically increases to the expected value of 1 that corresponds to the 3o1i manifold. For intermediate values the $q = 0$ ordered 3o1i state is selected, as we can see from the polarization data that tends to the corresponding $1/2 = 0.5$ continuous black line. For the largest value (pink lines) the perpendicular coupling becomes the dominant energy scale of in the system, leading again to the selection of the 2i2o state with vanishing average charge and a polarization of $1/\sqrt{3} \approx 0.57$. Again, all ordering transitions seem to be first order phase transitions judging by the discontinuities in the energy, polarization and charge average and the sharpness of the corresponding heat capacity peaks.
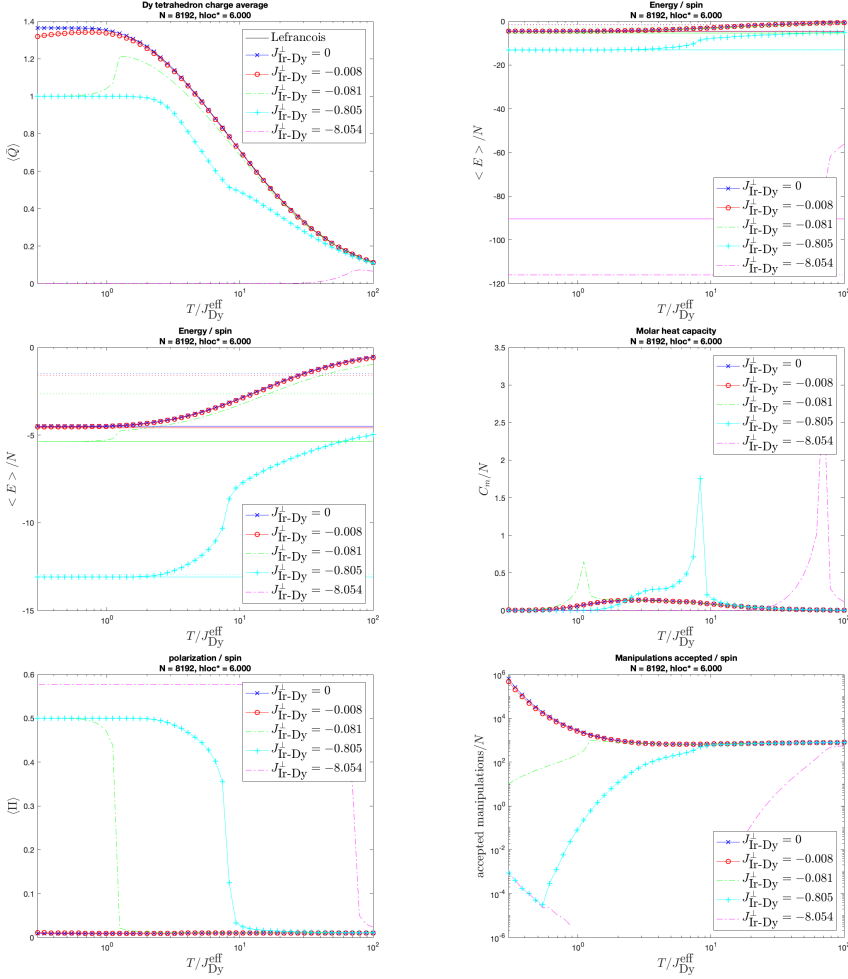
Figure 4.11: Computed observable curves for $h_*^{\text{loc}} = 6$.

4.7 Conclusion

In this chapter we have introduced an extension of the famous spin ice model that is proposed to describe the behavior of compounds of iridium and rare-earth magnetic atoms, such as $\text{Dy}_2\text{Ir}_2\text{O}_7$. In these crystals, a local magnetic field acts as a chemical potential for the monopole excitations of the canonical spin ice model on the dysprosium pyrochlore lattice and can so stabilize
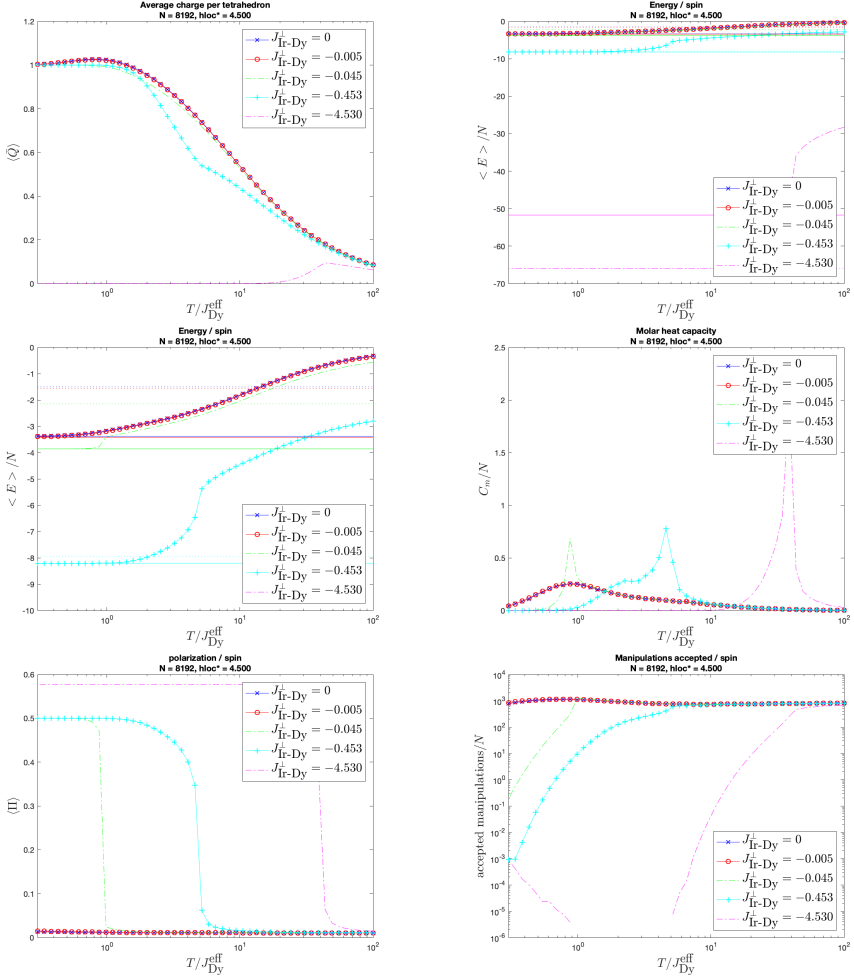
Figure 4.12: Computed observable curves for $h_*^{\mathrm{loc}} = 4.5$.

ground states with a non-zero monopole charge. This non-uniform field results from a coupling of the Ising-like spins to the Heisenberg spins of the interpenetrating pyrochlore lattice populated by the iridium atoms, which are induced to collectively co-order into the all-out all-in position by the presence of sizeable Dzyaloshinksy-Moriya interactions. The pinning on this lattice is significantly softer than the anisotropy-mediated reduction of sym-

metry to effective Ising spins in spin ice, opening the ground to competition effects.

We have found an analytical expression for the change in energy resulting from a small angle deviation from the iridium all-in all-out ordering, Eq. (4.27). Minimizing this energy we find the optimal angle of Eq. (4.28), which feeds back into the energy to express it purely as a function of of the parallel and perpendicular components of an effective field produced by the six dysprosium spins surrounding an iridium site as defined in Eq. (4.23). If this energy change turns negative it becomes advantageous to the system to adopt the proposed small angle deviation. This would require a large perpendicular component and a small parallel component of the dysprosium generated field.

We have investigated the optimal dysprosium configurations on various finite plaquettes of different sizes in section 4.5, wich suggest that a uniform, translationally invariant covering of identical tetrahedra containing a zero charge is preferrred. Furthermore, restricting to the submanifold with charge ± 1 or ∓ 1 tetrahedra the largest perpendicular fields are achieved by the translationally invariant covering of tetrahedra with the same unimodular charge. In section 4.6 we have displayed the results of Monte Carlo simulation of this small angle deviation setup, which confirm thes expectations. Unfortunately, the natural value of the interaction strength mediating the perpendicular field term is found to be small in the case of $Dy_2Ir_2O_7$ and so does not lead to significant changes to the physics of this compound. A slight exception can be made at the boundary values of different selection regimes, where the perpendicular component can be sufficient to tip the system over into the preferred translationally invariant zero charge state or runner up translationally invariant unit charge covering. There is the possibility of larger perpendicular field interaction strengths in other materials, which we have investigated by artificially inflating the value in our simulations. If an additional reinforcement mechnism can be found it might induce an interesting phase transition into the preferred uniform vanishing charge state, which seems likely to be of first order by the discontinuities it produces in observable plots.

4.8 Appendix: reference frames

4.8.1 Edge-up reference frame

In the edge-up reference frame one of the plus tetrahedra of in the pyrochlore lattice is put on its side, so that its edges coincide with the diagonals of the faces of a cube. The unit vectors of the local trigonal directions, see Fig. 4.2a, can then be parametrized as

$$\hat{u}_1 = \frac{1}{\sqrt{3}} \left(+1, -1, -1\right)^T, \qquad \hat{u}_2 = \frac{1}{\sqrt{3}} \left(-1, -1, +1\right)^T,$$

$$\hat{u}_3 = \frac{1}{\sqrt{3}} \left(+1, +1, +1\right)^T, \qquad \hat{u}_4 = \frac{1}{\sqrt{3}} \left(-1, +1, -1\right)^T. \qquad (4.37)$$

In the edge-up frame, the non-vanishing vector elements of the matrix containing the Dzyaloshinsky-Moriya axes, see Fig. 4.2b, are parametrized as

$$\mathbf{D}_{12} = -\mathbf{D}_{21} = \frac{1}{\sqrt{2}} \left(-1, 0, -1\right)^T, \qquad \mathbf{D}_{13} = -\mathbf{D}_{31} = \frac{1}{\sqrt{2}} \left(0, -1, +1\right)^T,$$

$$\mathbf{D}_{14} = -\mathbf{D}_{41} = \frac{1}{\sqrt{2}} \left(+1, +1, 0\right)^T, \qquad \mathbf{D}_{23} = -\mathbf{D}_{32} = \frac{1}{\sqrt{2}} \left(-1, +1, 0\right)^T,$$

$$\mathbf{D}_{24} = -\mathbf{D}_{42} = \frac{1}{\sqrt{2}} \left(0, -1, -1\right)^T, \qquad \mathbf{D}_{34} = -\mathbf{D}_{43} = \frac{1}{\sqrt{2}} \left(-1, 0, +1\right)^T.$$
$$(4.38)$$

4.8.2 face-up reference frame

Another useful frame of reference is the face-up reference frame, in which tetrahedra have one trigonal axis aligned with the z direction. The local trigonal unit vectors then take the parametrization

$$\hat{u}_1 = (0, 0, -1)^T, \qquad \hat{u}_2 = \left(-\sqrt{\frac{2}{9}}, \sqrt{\frac{2}{3}}, \frac{1}{3}\right)^T,$$

$$\hat{u}_3 = \left(\sqrt{\frac{8}{9}}, 0, \frac{1}{3}\right)^T, \qquad \hat{u}_4 = \left(-\sqrt{\frac{2}{9}}, -\sqrt{\frac{2}{3}}, \frac{1}{3}\right)^T. \qquad (4.39)$$

Bibliography

[1] M. E. Peskin and D. V. Schroeder, *An Introduction to Quantum Field Theory* (Westview Press, 1995).

[2] H. T. C. Stoof, D. B. M. Dickerscheid, and K. Gubbels, *Ultracold Quantum Fields*, 1st ed. (Springer, 2009).

[3] A. Altland and B. D. Simons, *Condensed Matter Field Theory*, 2nd ed. (Cambridge University Press, 2010).

[4] P. A. M. Dirac, Proc. R. Soc. Lond. A **117**, 610 (1928).

[5] N. P. Armitage, E. J. Mele, and A. Vishwanath, Rev. Mod. Phys. **90**, 015001 (2018).

[6] H. Weyl, Proc. Natl. Acad. Sci. **15**, 323 (1929).

[7] A. A. Soluyanov, D. Gresch, Z. Wang, Q. Wu, M. Troyer, X. Dai, and B. A. Bernevig, Nature **527**, 495 (2015).

[8] R. Rechciński and J. Tworzydło, Acta Physica Polonica A **130**, 1179 (2016).

[9] H. Nielsen and M. Ninomiya, Physics Letters B **130**, 389 (1983).

[10] S. M. Carroll, *Spacetime and geometry: An introduction to general relativity* (Addison-Wesley, 2004).

[11] D. Xiao, M.-C. Chang, and Q. Niu, Rev. Mod. Phys. **82**, 1959 (2010).

[12] B. Q. Lv, H. M. Weng, B. B. Fu, X. P. Wang, H. Miao, J. Ma, P. Richard, X. C. Huang, L. X. Zhao, G. F. Chen, *et al.*, Phys. Rev. X **5**, 031013 (2015).

[13] B. Lv, N. Xu, H. Weng, J. Ma, P. Richard, X. Huang, L. Zhao, G. Chen, C. Matt, F. Bisti, *et al.*, Nature Physics **11**, 724 (2015).

Bibliography

[14] S.-Y. Xu, I. Belopolski, N. Alidoust, M. Neupane, G. Bian, C. Zhang, R. Sankar, G. Chang, Z. Yuan, C.-C. Lee, *et al.*, Science **349**, 613 (2015).

[15] L. Yang, Z. Liu, Y. Sun, H. Peng, H. Yang, T. Zhang, B. Zhou, Y. Zhang, Y. Guo, M. Rahn, *et al.*, Nature Physics **11**, 728 (2015).

[16] X. Wan, A. M. Turner, A. Vishwanath, and S. Y. Savrasov, Phys. Rev. B **83**, 205101 (2011).

[17] S. A. Parameswaran, T. Grover, D. A. Abanin, D. A. Pesin, and A. Vishwanath, Phys. Rev. X **4**, 031035 (2014).

[18] Y. Baum, E. Berg, S. A. Parameswaran, and A. Stern, Phys. Rev. X **5**, 041046 (2015).

[19] K. Oura, S. Lifshits, V. G., Z. A., A.V., and M. Katayama, *Surface Science: an Introduction*, 1st ed. (Springer-Verlag, 2003).

[20] D. J. Griffiths, *Introduction to Electrodynamics*, 4th ed. (Pearson, Boston, MA, 2013).

[21] G. H. Hardy, *Divergent series*, 1st ed. (Clarendon Press, Oxford, 1949).

[22] D. J. Griffiths, *Introduction of Quantum Mechanics*, 2nd ed. (Prentice Hall, Inc., 1995).

[23] H. Weng, C. Fang, Z. Fang, B. A. Bernevig, and X. Dai, Phys. Rev. X **5**, 011029 (2015).

[24] N. Xu, H. Weng, B. Lv, C. Matt, J. Park, F. Bisti, V. Strocov, E. Pomjakushina, K. Conder, N. Plumb, *et al.*, Nature Comm. **7**, 11006 (2015).

[25] A. Altland and D. Bagrets, Phys. Rev. B **93**, 075113 (2016).

[26] J. H. Pixley, P. Goswami, and S. Das Sarma, Phys. Rev. Lett. **115**, 076601 (2015).

[27] M. Trescher, B. Sbierski, P. W. Brouwer, and E. J. Bergholtz, Phys. Rev. B **95**, 045139 (2017).

[28] E. Abrahams, P. W. Anderson, D. C. Licciardello, and T. V. Ramakrishnan, Phys. Rev. Lett. **42**, 673 (1979).

[29] E. Fradkin, Phys. Rev. B **33**, 3263 (1986).

[30] Y. Ominato and M. Koshino, Phys. Rev. B **89**, 054202 (2014).

[31] J. H. Pixley, D. A. Huse, and S. Das Sarma, Phys. Rev. X **6**, 021042 (2016).

[32] P. J. Smith, The American Statistician **49**, 217 (1995).

[33] K. G. Wilson, Phys. Rev. B **4**, 3174 (1971).

[34] K. G. Wilson, Phys. Rev. B **4**, 3184 (1971).

[35] B. Roy, R.-J. Slager, and V. Juričić, Phys. Rev. X **8**, 031076 (2018).

[36] G. 't Hooft and M. Veltman, Nuclear Physics B **44**, 189 (1972).

[37] C. G. Callan, Phys. Rev. D **2**, 1541 (1970).

[38] K. Symanzik, Communications in Mathematical Physics **18**, 227 (1970).

[39] T. S. Sikkenk and L. Fritz, Phys. Rev. B **96**, 155121 (2017).

[40] S.-M. Huang, S.-Y. Xu, I. Belopolski, C.-C. Lee, G. Chang, B. Wang, N. Alidoust, G. Bian, M. Neupane, C. Zhang, *et al.*, Nature Comm. **6**, 7373 (2015).

[41] S.-Y. Xu, N. Alidoust, I. Belopolski, Z. Yuan, G. Bian, T.-R. Chang, H. Zheng, V. N. Strocov, D. S. Sanchez, G. Chang, *et al.*, Nature Physics **11**, 748 (2015).

[42] C. Shekhar, A. K. Nayak, Y. Sun, M. Schmidt, M. Nicklas, I. Leermakers, U. Zeitler, W. Schnelle, J. Grin, C. Felser, *et al.*, Nature Physics **11**, 645 (2015).

[43] L.-k. Shi and J. C. W. Song, Phys. Rev. B **96**, 081410 (2017).

[44] S. Bera, J. D. Sau, and B. Roy, Phys. Rev. B **93**, 201302 (2016).

Bibliography

[45] S. V. Syzranov and L. Radzihovsky, Annual Review of Condensed Matter Physics **9**, 35 (2018).

[46] P. W. Anderson, Phys. Rev. **109**, 1492 (1958).

[47] J. H. Bardarson, J. Tworzydło, P. W. Brouwer, and C. W. J. Beenakker, Phys. Rev. Lett. **99**, 106801 (2007).

[48] J. Xiong, S. K. Kushwaha, T. Liang, J. W. Krizan, W. Wang, R. J. Cava, and N. P. Ong, Preprint, arXiv:1503.08179 (2015).

[49] B. Sbierski, G. Pohl, E. J. Bergholtz, and P. W. Brouwer, Phys. Rev. Lett. **113**, 026602 (2014).

[50] S. V. Syzranov, L. Radzihovsky, and V. Gurarie, Phys. Rev. Lett. **114**, 166601 (2015).

[51] J. H. Pixley, P. Goswami, and S. Das Sarma, Phys. Rev. B **93**, 085103 (2016).

[52] Y. I. Rodionov, K. I. Kugel, and F. Nori, Phys. Rev. B **92**, 195117 (2015).

[53] M. Trescher, B. Sbierski, P. W. Brouwer, and E. J. Bergholtz, Phys. Rev. B **91**, 115135 (2015).

[54] E. J. Bergholtz, Z. Liu, M. Trescher, R. Moessner, and M. Udagawa, Phys. Rev. Lett. **114**, 016806 (2015).

[55] K. Koepernik, D. Kasinathan, D. V. Efremov, S. Khim, S. Borisenko, B. Büchner, and J. van den Brink, Phys. Rev. B **93**, 201101 (2016).

[56] L. Huang, T. M. McCormick, M. Ochi, Z. Zhao, M.-T. Suzuki, R. Arita, Y. Wu, D. Mou, H. Cao, J. Yan, *et al.*, Nature Mater. **15**, 1155 (2016).

[57] I. Belopolski, D. S. Sanchez, Y. Ishida, X. Pan, P. Yu, S.-Y. Xu, G. Chang, T.-R. Chang, H. Zheng, N. Alidoust, *et al.*, Nature Comm. **7**, 13643 (2016).

[58] A. A. Zyuzin and R. P. Tiwari, JETP Letters **103**, 717 (2016).

[59] T. E. O'Brien, M. Diez, and C. W. J. Beenakker, Phys. Rev. Lett. **116**, 236401 (2016).

[60] Z.-M. Yu, Y. Yao, and S. A. Yang, Phys. Rev. Lett. **117**, 077202 (2016).

[61] P. Goswami and S. Chakravarty, Phys. Rev. Lett. **107**, 196803 (2011).

[62] B. Roy and S. Das Sarma, Phys. Rev. B **90**, 241112 (2014).

[63] F. Detassis, L. Fritz, and S. Grubinskas, Phys. Rev. B **96**, 195157 (2017).

[64] T. S. Sikkenk and L. Fritz, Phys. Rev. B **100**, 085121 (2019).

[65] K. S. Novoselov, A. K. Geim, S. V. Morozov, D. Jiang, Y. Zhang, S. V. Dubonos, I. V. Grigorieva, and A. A. Firsov, Science **306**, 666 (2004).

[66] H. Weyl, Zeitschrift fr Physik **56**, 330 (1929).

[67] A. C. Potter, I. Kimchi, and A. Vishwanath, Nature Communications **5** (2014).

[68] X. Huang, L. Zhao, Y. Long, P. Wang, D. Chen, Z. Yang, H. Liang, M. Xue, H. Weng, Z. Fang, X. Dai, and G. Chen, Phys. Rev. X **5**, 031023 (2015).

[69] F. Arnold, C. Shekhar, S.-C. Wu, Y. Sun, R. D. dos Reis, N. Kumar, M. Naumann, M. O. Ajeesh, M. Schmidt, A. G. Grushin, J. H. Bardarson, M. Baenitz, D. Sokolov, H. Borrmann, M. Nicklas, C. Felser, E. Hassinger, and B. Yan, Nature Communications **7** (2016).

[70] C.-L. Zhang, S.-Y. Xu, I. Belopolski, Z. Yuan, Z. Lin, B. Tong, G. Bian, N. Alidoust, C.-C. Lee, S.-M. Huang, T.-R. Chang, G. Chang, C.-H. Hsu, H.-T. Jeng, M. Neupane, D. S. Sanchez, H. Zheng, J. Wang, H. Lin, C. Zhang, H.-Z. Lu, S.-Q. Shen, T. Neupert, M. Zahid Hasan, and S. Jia, Nature Communications **7** (2016).

[71] B. Sbierski, K. A. Madsen, P. W. Brouwer, and C. Karrasch, Phys. Rev. B **96**, 064203 (2017).

Bibliography

[72] M. Buchhold, S. Diehl, and A. Altland, Phys. Rev. Lett. **121**, 215301 (2018).

[73] V. N. Kotov, B. Uchoa, V. M. Pereira, F. Guinea, and A. H. Castro Neto, Rev. Mod. Phys. **84**, 1067 (2012).

[74] J. C. Ward, Phys. Rev. **78**, 182 (1950).

[75] J. González, F. Guinea, and M. Vozmediano, Nuclear Physics B **424**, 595 (1994).

[76] E. C. I. van der Wurff and H. T. C. Stoof, Phys. Rev. B **96**, 121116 (2017).

[77] K. Das and A. Agarwal, Phys. Rev. B **99**, 085405 (2019).

[78] P. Li, Y. Wen, X. He, Q. Zhang, , C. Xia, Z.-M. Yu, S. A. Yang, Z. Zhu, H. N. Alshareef, and X.-X. Zhang, Nature Communications **8** (2017).

[79] S. F. Edwards and P. W. Anderson, Journal of Physics F: Metal Physics **5**, 965 (1975).

[80] P.-L. Zhao and A.-M. Wang, Preprint, arXiv:1811.11437v1 (2018).

[81] Z.-K. Yang, J.-R. Wang, and G.-Z. Liu, Phys. Rev. B **98**, 195123 (2018).

[82] K. Kobayashi, T. Ohtsuki, K.-I. Imura, and I. F. Herbut, Phys. Rev. Lett. **112**, 016402 (2014).

[83] A. A. Abrikosov and S. Beneslavskii, Soviet Physics JETP **32**, 699 (1971).

[84] J. González, Phys. Rev. B **96**, 081104 (2017).

[85] M. Vozmediano, M. Katsnelson, and F. Guinea, Physics Reports **496**, 109 (2010).

[86] L. Pauling, Journal of the American Chemical Society **57**, 2680 (1935).

[87] W. F. Giauque and J. W. Stout, Journal of the American Chemical Society **58**, 1144 (1936).

[88] P. W. Anderson, Phys. Rev. **102**, 1008 (1956).

[89] S. T. Bramwell and M. J. P. Gingras, Science **294**, 1495 (2001).

[90] M. J. Harris, S. T. Bramwell, D. F. McMorrow, T. Zeiske, and K. W. Godfrey, Phys. Rev. Lett. **79**, 2554 (1997).

[91] J. S. Gardner, M. J. P. Gingras, and J. E. Greedan, Rev. Mod. Phys. **82**, 53 (2010).

[92] C. Castelnovo, R. Moessner, and S. L. Sondhi, Nature **451**, 42 (2008).

[93] E. Lefrançois, V. Cathelin, E. Lhotel, J. Robert, P. Lejay, C. V. Colin, B. Canals, F. Damay, J. Ollivier, B. Fåk, L. C. Chapon, R. Ballou, and V. Simonet, Nat. Comm. **8** (2017).

[94] K. Matsuhira, M. Wakeshima, Y. Hinatsu, and S. Takagi, Journal of the Physical Society of Japan **80**, 094701 (2011).

[95] H. Fukazawa, R. G. Melko, R. Higashinaka, Y. Maeno, and M. J. P. Gingras, Phys. Rev. B **65**, 054410 (2002).

[96] S. T. Bramwell and M. J. Harris, Journal of Physics: Condensed Matter **10**, L215 (1998).

[97] T. M. McQueen, D. V. West, B. Muegge, Q. Huang, K. Noble, H. W. Zandbergen, and R. J. Cava, Journal of Physics: Condensed Matter **20**, 235210 (2008).

[98] S. Petit, E. Lhotel, B. Canals, M. Ciomaga Hatnean, J. Ollivier, H. Mutka, E. Ressouche, A. R. Wildes, M. R. Lees, and G. Balakrishnan, Nature Physics **12**, 746 (2016).

[99] E. Lefrançois, V. Simonet, R. Ballou, E. Lhotel, A. Hadj-Azzem, S. Kodjikian, P. Lejay, P. Manuel, D. Khalyavin, and L. C. Chapon, Phys. Rev. Lett. **114**, 247202 (2015).

[100] J. N. Reimers, Phys. Rev. B **45**, 7287 (1992).

[101] R. Moessner and J. T. Chalker, Phys. Rev. Lett. **80**, 2929 (1998).

[102] M. Elhajal, B. Canals, R. Sunyer, and C. Lacroix, Phys. Rev. B **71**, 094420 (2005).

[103] S. T. Bramwell, M. J. Harris, B. C. den Hertog, M. J. P. Gingras, J. S. Gardner, D. F. McMorrow, A. R. Wildes, A. L. Cornelius, J. D. M. Champion, R. G. Melko, and T. Fennell, Phys. Rev. Lett. **87**, 047205 (2001).

[104] B. C. den Hertog and M. J. P. Gingras, Phys. Rev. Lett. **84**, 3430 (2000).

[105] B. I. Kharisov and O. V. Kharissova, *Carbon Allotropes: Metal-Complex Chemistry, Properties and Applications* (Springer International Publishing, 2019).

Summary

The subdiscipline of physics modernly known as condensed matter theory concerns itself with describing the properties of systems composed of a large number of atoms. Such collections tend to develop behavior that is more than the sum of that of its constituents. Such synergic, or *emergent*, effects are a familiar occurrence in everyday life through thermodynamics: the temperature of an object is a statistical average of the total kinetic energy, and so is poorly defined for a single molecule. Similarly, the collective ordering of the magnetic moments of different atoms gives rise to the phenomenon of magnetism in its various guises.

Distorted Weyl cones under perturbation

(a) Diamond lattice.   (b) Graphite lattice.   (c) Graphene lattice.
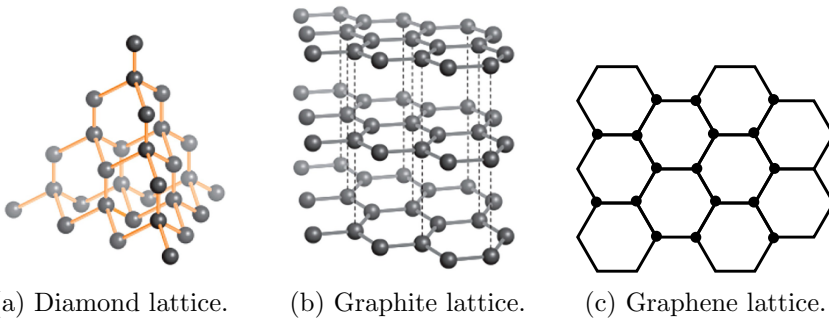
Figure 1: The lattice structure of some common carbon allotropes [105]

One of the major accomplishments of physics in the last century was the development of a theory for understanding metals. The atoms of solid materials are arranged in periodic structures known as *crystals*, which dictates to a large extent what physical properties they have. For example, a diamond in a ring and the graphite of the lead in a pencil are both pure carbon allotropes, meaning they are completely composed of C-atoms. However, due to their different lattice structures, see Fig. 1, the two substances are

still substantially different. In a crystallic structure, the orbits of the atoms' electrons come to overlap in space. This is in contradiction with the exclusion principle, a statistical law that states that matter particles, or *fermions*, cannot share the same quantum number. As a consequence, the atomic orbitals split into a set of near-continuous bands with different energies. This band structure details the allowed relation between the momenta of the electrons in the material and their energies. Some of these structures have large gaps between the bands where electron states are not permitted, see Fig. 2a. This means the energy cost of bringing the electrons in motion, causing an electric current to flow, is insurmountably large. Such materials will be insulators. Metals on the other hand have no such gaps in their band structures, see Fig. 2b, by virtue of which they tend to be good conductors of electricity. Semiconductors have band structures that are in between an insulating and conducting form, with a small gap separating two bands, see Fig. 2c. This means they can relatively easily be doped with additional electrons or electron-holes, inserting supernumerary charge carriers into the system. Joining these two types of doped semiconductors creates a heterostructure that acts as an electronic diode, in which electricity can flow in one direction but not the other. In a transistor this property forms the basis of the 0s and 1s that provide the bits for the memories of our modern computers.

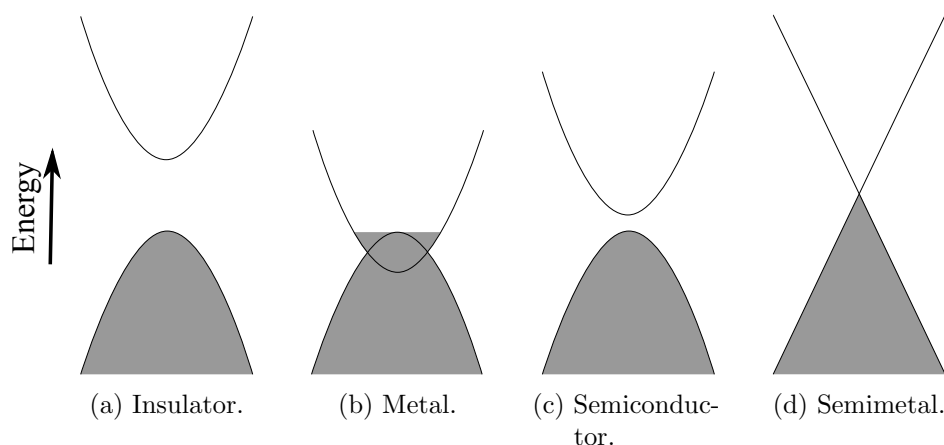(a) Insulator.   (b) Metal.   (c) Semiconductor.   (d) Semimetal.

Figure 2: Different types of band structures encountered in condensed matter systems.

In some materials, the band structure has some special regions where it resembles two inverted cones connected only at a nodal point at their tips, see Fig. 2d. It is possible then to bring the electrons in motion by paying a given slight energy cost, but mostly not as many of them as in the case of a metal. These materials, aptly called semimetals, then do conduct electricity, but mostly less well than a proper conductor. A commonly known material with such a band touching point and linear dispersion is graphene. Famously, it is only a single atomic layer thick, with its carbon atoms arranging on a purely two dimensional lattice shaped like a honeycomb, see Fig. 1c. By virtue of its exceptional mechanical strength and extraordinary electronic properties, discoverers Geim and Novoselov were awarded the Nobel prize just five years after first isolating it in 2004.

In Weyl semimetals the Fermi velocity associated with the approximately linear dispersion of the excitations near the band touching point is much smaller than the fundamental speed of light in vacuum c. Consequently their conical spectrum is not bound by Lorentz symmetry and can develop tilts and anisotropies, as has been found in real-life materials such as WTe_2. Furthermore, perturbations like disorder and Coulomb interactions can obfuscate and complicate the picture that emerges from the free, fully symmetric Weyl fermion model. We have investigated how the interplay of these disturbances impacts the scaling behavior of observables depending on the Density of States, which nominally vanishes at the free theory nodal point.

Monopole stabilization in interpenetrating pyrochlore lattices

Besides more well-known concepts as mass and charge, all fundamental particles have a property called *spin*. The spin of a particle is an intrinsic part of its total angular momentum. Unlike more conventional orbital angular momentum, however, it has no counterpart in classical mechanics and is therefore said to be a purely quantum quantity. In the classic Stern-Gerlach experiment, first performed in 1922, a magnetic field deflects the particles in a beam according to their spins, producing a set of discrete points on the detector screen. This shows that we can think of spinful particles as tiny bar magnets of various strengths. In this way spin leads to magnetic interactions between atoms. These can be ferromagnetic, favoring spins to point in the same direction, or antiferromagnetic, by which spins preferentially anti-align.

Summary

In some lattice structures of crystalline solids, the geometry is incompatible with the demands imposed by the interactions between the atoms spins. For example, on triangular setups antiferromagnetic couplings between Ising spins, which have only two possible states, cannot all be simultaneously satisfied, See Fig. 3a. This phenomenon is known as *frustration*. There are multiple ways to place the spins in a way that optimizes the interactions and come to a lowest energy state, see Fig. 3b. We say the ground state of the Ising triangular model with frustrated interactions is *degenerate*.

(a) The third spin on the triangle does not have a preferred direction.

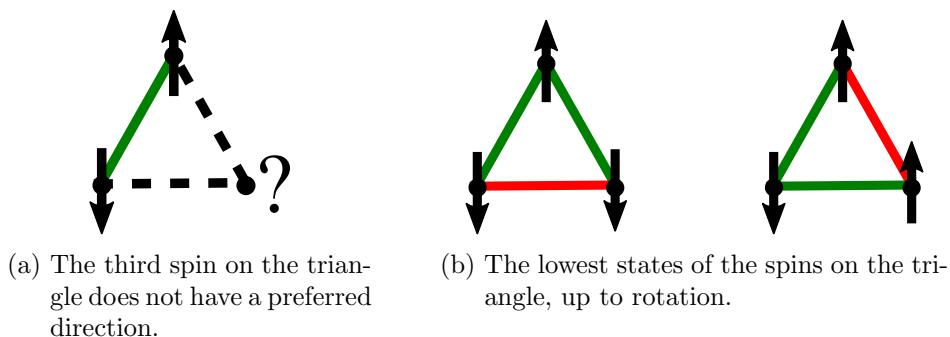(b) The lowest states of the spins on the triangle, up to rotation.

Figure 3: Frustration of antiferromagnetically interacting Ising spins on a triangle.

A more complex structure in which frustration appears is the pyrochlore lattice, see Fig. 4.1a. It is composed of corner-sharing tetrahedra that make it impossible to satisfy all the antiferromagnetic interactions between the Ising-like spins. In such spin ice models the lowest energy states obey the spin ice rule: every ground state tetrahedron must have two spins pointing inwards and two spins pointing outwards. This can be interpreted as a divergence-free condition of an effective field, with as many of the field lines leaving the tetrahedron as are entering it. Excitations above this extensively degenerate ground state manifold then obtain an interpretation as pairs of sources and sinks of this field. These monopoles are detectable in for example neutron scattering experiments and influence the low-temperature transport behavior of spin ice materials. We have investigated perturbations to a particular set-up in which two of these pyrochlore lattices interpenetrate and their spins interact, resulting in an effective chemical potential for the monopoles that can stabilize them.

Samenvatting

De subdiscipline van de fysica die tegenwoordig bekend staat als theorie van de gecondenseerde materie houdt zich bezig met het beschrijven van de eigenschappen van systemen die uit een groot aantal atomen bestaan. Dergelijke collecties hebben de neiging om gedrag te ontwikkelen dat meer is dan de som van dat van de samenstellende delen. Zulke synergie, of *emergentie*, is in het dagelijks leven bekend door de thermodynamica: de temperatuur van een object is een statistisch gemiddelde van de totale kinetische energie en is dus slecht gedefinieerd voor een enkel molecuul. Evenzo leidt de collectieve ordening van de magnetische momenten van verschillende atomen tot de verschillende verschijningsvormen van magnetisme.

Vervormde Weyl-kegels onder verstoring

Een van de belangrijkste prestaties van de natuurkunde in de vorige eeuw is de ontwikkeling van een theorie die ons in staat stelt het gedrag van metalen te begrijpen. De atomen van vaste materialen zijn gerangschikt in periodieke structuren die bekend staan als *kristallen*. Dit bepaalt in hoge mate welke fysische eigenschappen ze hebben. Een diamant in een ring en het grafiet in het lood van een potlood zijn bijvoorbeeld pure koolstofallotropen, wat betekent dat ze volledig zijn samengesteld uit C-atomen. Vanwege hun verschillende roosterstructuren, zie Fig. 1, zijn het echter nog steeds substantieel verschillende stoffen. In een kristalstructuur overlappen de banen van de elektronen rond de atomen elkaar in de ruimte. Dit is in tegenspraak met het uitsluitingsprincipe, een statistische wet die bepaalt dat materiedeeltjes, of *fermionen*, niet hetzelfde kwantumgetal kunnen hebben. Als gevolg hiervan splitsen de atomaire orbitalen zich in een reeks van bijna-continue banden met verschillende energieën. Deze bandstructuur specificeert de toegestane relatie tussen de snelheid van de elektronen in het materiaal en hun energieën. Sommige van deze structuren hebben grote openingen tussen de banden waar elektronentoestanden niet zijn toegestaan, zie Fig. 2a. Dit betekent dat de energiekosten om een elektron te versnellen, en zo een elek-

trische stroom te laten vloeien, onoverkomelijk groot is. Dergelijke materialen zijn isolatoren. Metalen daarentegen hebben niet zulke openingen in hun bandstructuren, zie Fig. 2b, waardoor ze niet zulke goede geleiders van elektriciteit zijn. Halfgeleiders hebben bandstructuren die zich tussen een isolerende en geleidende vorm bevinden, met een kleine opening tussen twee banden, zie Fig. 2c. Dit betekent dat het relatief eenvoudig is om extra elektronen of elektron-gaten toe te voegen, waardoor overtollige ladingsdragers in het systeem worden geïntroduceerd. Het samenvoegen van deze twee soorten halfgeleiders creëert een heterostructuur die werkt als een elektronische diode, waarin elektriciteit in de ene richting kan stromen maar niet in de andere. In een transistor ligt deze eigenschap aan de basis van de nullen en enen die de bits voor de geheugens van onze moderne computers vormen.

In sommige materialen heeft de bandstructuur enkele speciale gebieden waar ze lijkt op twee omgekeerde kegels die slecht op één punt aan hun uiteinden zijn verbonden, zie Fig. 2d. Het is dan mogelijk om de elektronen in beweging te brengen door een kleine energiekoste te betalen, maar meestal niet zoveel van hen als in het geval van een metaal. Deze materialen, toepasselijk semimetalen genoemd, geleiden dan elektriciteit, maar meestal minder goed dan een normaal metaal. Een bekend materiaal met een dergelijk bandaanrakingspunt en lineaire dispersie is grafeen. In dit materiaal zijn alle koolstofatomen gerangschikt op een tweedimensionaal rooster in de vorm van een honingraat, zie Fig. 1c, wat het extreem dun maakt. Op grond van zijn uitzonderlijke mechanische sterkte en buitengewone elektronische eigenschappen ontvingen ontdekkers Geim en Novoselov slechts vijf jaar na de eerste isolatie in 2004 de Nobelprijs.

In Weyl-semimetalen is de Fermi-snelheid geassocieerd met de ongeveer lineaire dispersie van de excitaties nabij het contactpunt van de banden veel kleiner dan de fundamentele lichtsnelheid in het vacuüm c. Omdat hun conische spectrum niet gebonden is aan Lorentz-symmetrie kunnen zich kantelingen en anisotropieën ontwikkelen, zoals is gevonden in bijvoorbeeld WTe_2. Bovendien kunnen verstoringen zoals atomische wanorde en Coulombinteracties het beeld dat geschetst wordt door het vrije, volledig symmetrische Weyl fermion-model beïnvloeden. Wij hebben onderzocht hoe het schaalgedrag van experimenteel observeerbare toestanddichtheid, die verdwijnt op het bandaanrakingspunt van het vrije model, wordt beïnvloed door het samenspel van deze vervormingen en verstoringen.

Monopoolstabilisatie in interpenetrerende pyrochloreroosters

Naast bekendere concepten als massa en lading hebben alle fundamentele deeltjes een eigenschap genaamd *spin*. De spin van een deeltje is een intrinsiek onderdeel van zijn totale hoekmomentum. In tegenstelling tot het conventionelere orbitaal hoekmomentum heeft het echter geen tegenhanger in de klassieke mechanica en wordt daarom gezien als een pure kwantumgrootheid. In het bekende Stern-Gerlach-experiment, dat voor het eerst werd uitgevoerd in 1922, buigt een magnetisch veld de deeltjes in een straal af naar gelang hun spins, wat resulteert in een reeks discrete punten op het detectiescherm. Dit laat zien dat we spindeeltjes kunnen beschouwen als kleine staafmagneetjes van verschillende sterktes. Op deze manier leidt spin tot magnetische interacties tussen atomen. Deze kunnen ferromagnetisch zijn, zodat spins het liefst in dezelfde richting wijzen, of antiferromagnetisch, waardoor spins bij voorkeur de andere kant op gericht zijn.

In sommige roosterstructuren van kristallijne vaste stoffen is de geometrie onverenigbaar met voorkeursrichtingen van de interacties tussen de spins van de atomen. Op driehoekige opstellingen kunnen antiferromagnetische koppelingen tussen Ising-spins, die slechts twee mogelijke toestanden hebben, niet allemaal tegelijkertijd worden voldaan, zie Fig. 3a. Dit fenomeen staat bekend als *frustratie*. Er zijn meerdere manieren om de spins zo te plaatsen dat de interacties geoptimaliseerd worden en tot een laagste energiestatus te komen, zie Fig. 3b. We zeggen dat de grondtoestand van het model met gefrustreerde interacties *degeneratief* is.

Een complexere structuur waarin frustratie een rol speelt is het pyrochloorrooster, zie Fig. 4.1a. Het is samengesteld uit tetraëders die verbonden zijn aan de hoekpunten, waardoor het onmogelijk is om alle antiferromagnetische interacties tussen de Ising-achtige spins te bevredigen. In dergelijke spin-ijsmodellen houden de laagste energietoestanden zich aan de spin-ijsregel: elke tetraëder in grondtoestand moet twee spins hebben die naar binnen wijzen en twee die naar buiten wijzen. Dit kan worden geïnterpreteerd als een divergentie-vrije conditie voor een effectief veld, waarvan net zoveel veldlijnen de tetraëder verlaten als dat er binnenkomen. Excitaties vanuit deze extensief degeneratieve grondtoestand zijn dan op te vatten als paren van bronnen en putten van dit veld. Deze monopolen zijn detecteerbaar in bijvoorbeeld neutronenverstrooiingsexperimenten en beïnvloeden het transportgedrag van spin-ijsmaterialen bij lage temperaturen. Wij hebben

onderzocht hoe een opstelling waarin twee van deze pyrochloorroosters on-
derling doordringen en hun spins interacteren, resulterend in een effectief
chemisch potentieel voor de monopolen dat ze kan stabiliseren, reageert op
verstoringen.

About the author

Tycho Sikkenk was born on the 29th of January, 1991 in Houten, the Netherlands. In 2009, he obtained a *cum laude* gymnasium degree with a double major in Science and Health at the Christelijk Gymnasium in neighboring Utrecht. He started his tertiary education with a Bachelor in Liberal Arts and Sciences at the University College Utrecht, the international honors program of Utrecht University. Pursuing his broad interests, he majored in physics and mathematics and molecular biology, while also dappling in areas as diverse as economics, further Latin and Spanish. The latter brought him to enter an exchange program with the Universidad de Guadalajara in Guadalajara, Mexico, during the spring of 2011. He graduated from the University College in 2012 with a 3.72 GPA and a *cum laude* distinction, writing a thesis in physics on the representations of the Lorentz group.

That same year he moved to London to read physics for a Master's in Quantum Fields and Fundamental Forces at Imperial College London, where he took mostly courses in high energy physics. He graduated in 2013 with an average of 72% and a distinction of *merit*, after working with prof. Fay Dowker on a thesis on the black hole firewall paradox. Switching focus from high energy to condensed matter physics he then enrolled in a second Master's in theoretical physics at Utrecht University in 2013, resulting in a thesis on frustrated quantum spins in the Swedenborgite lattice under supervision of dr. Lars Fritz and finishing with a 4.00 GPA.

In October 2015, Tycho started as a Ph.D. candidate at the Institute for Theoretical Physics in Utrecht under the continued supervision of dr. Lars Fritz, working on Weyl semimetals and spin liquids. He also spent a large part of his tenure as a visiting academic to the Condensed Matter Theory

group at Cambridge University in the United Kingdom, working with dr. Claudio Castelnovo on a project on extended spin ice models. The results of the research performed in the four years of this doctoral program are presented in this dissertation.

In his spare time, Tycho enjoys playing sports, among which cycling and field hockey stand out as particular favorites. He also likes to improve his foreign language skills in English and Spanish by reading anything from the great classics of literature to science fiction. In addition, he holds positions in the supervisory board of NWS, a non-profit uniting Dutch students abroad and promoting their interests in the domestic arena, and the board of University College Utrecht's alumni association.